LAND DEGRADATION ASSESSMENT FOR AN ABANDONED COAL MINE WITH GEOSPATIAL INFORMATION TECHNOLOGIES

A THESIS SUBMITTED TO
THE GRADUATE SCHOOL OF APPLIED AND NATURAL SCIENCES
OF
MIDDLE EAST TECHNICAL UNIVERSITY

BY

MUSTAFA KEMAL EMİL

IN PARTIAL FULFILLMENT OF THE REQUIREMENTS
FOR
THE DEGREE OF MASTER OF SCIENCE
IN
MINING ENGINEERING

SEPTEMBER 2010

Approval of the thesis:

LAND DEGRADATION ASSESSMENT FOR AN ABANDONED COAL MINE WITH GEOSPATIAL INFORMATION TECHNOLOGIES

submitted by **MUSTAFA KEMAL EMİL** in partial fulfillment of the requirements for the degree of **Master of Science in Mining Engineering Department, Middle East Technical University** by,

Prof. Dr. Canan Özgen _____________________
Dean, Graduate School of **Natural and Applied Sciences**

Prof. Dr. Ali İhsan Arol _____________________
Head of Department, **Mining Engineering**

Prof. Dr. Şebnem Düzgün
Supervisor, **Mining Engineering Dept., METU** _____________________

Examining Committee Members:

Prof. Dr. Ali İhsan Arol _____________________
Mining Engineering Dept., METU

Assoc. Prof. Dr. Şebnem Düzgün _____________________
Mining Engineering Dept., METU

Prof. Dr. Vedat Toprak _____________________
Geological Engineering Dept., METU

Assoc. Prof. Dr. Ayşegül Aksoy _____________________
Environmental Engineering Dept., METU

Assist. Prof. Dr. Nuray Demirel _____________________
Mining Engineering Dept., METU

Date: 15. 09. 2010

I hereby declare that all information in this document has been obtained and presented in accordance with academic rules and ethical conduct. I also declare that, as required by these rules and conduct, I have fully cited and referenced all material and results that are not original to this work.

Name, Last name : Mustafa Kemal Emil

Signature :

ABSTRACT

LAND DEGRADATION ASSESSMENT FOR AN ABANDONED COAL MINE WITH GEOSPATIAL INFORMATION TECHNOLOGIES

Emil, Mustafa Kemal
M.Sc., Department of Mining Engineering
Supervisor: Assoc. Prof. Dr. Şebnem Düzgün

September 2010, 113 pages

This study proposes an approach for land degradation assessment for an abandoned coal mine by using geospatial information technologies. The land degradation assessment focuses on two major changes: topographical and Land Use and Land Cover (LULC). For this purpose, historical stereo aerial photos, Worldview-1, Landsat and ASTER satellite images, Terrestrial Laser Scanning (TLS) data, Global Positioning System (GPS) survey data, and ancillary maps were used for abandoned Ovacık surface coal mine.

Volume of excavations and fillings, drainage network deviations, and slope instabilities were the investigated topographical disturbances by comparison of the Digital Elevation Models (DEM) for pre- and post-mining stages between the years 1950 and 2009, respectively. Using aerial photos and Worldview-1 satellite image, LULC maps were prepared based on the same time period. Then areal extent and spatial pattern of the LULC change was calculated and mapped by post classification comparison method. Also, extraction of LULC map by maximum likelihood and Support Vector Machine (SVM) classification approaches were explored using ASTER data. In addition to that, image differencing algorithm were also employed using first bands of Landsat and ASTER dataset and images of

Normalized Difference Vegetation Index (NDVI) to delineate spatial changes across the research area.

The results of land degradation assessment show that there was a significant topographical disturbance and LULC change in the research area. Particularly, three dump areas with a total volume of 2,334,878 m^3 were identified by DEM subtraction. It was found that stream network around the primary dump site shifted towards south with a maximum displacement of 60m. There are also depressions formed where drainage network was disturbed by excavation and waste disposal resulting pit-lake and small ponds. Slope analysis reveals that slopes higher that 60 degrees were mainly observed in excavation area with 81 percent. LULC change study showed that the forest area decreased an amount of 106,485 m^2 from 1951 to 2008. However; by means of the forestation efforts in dump sites, an amount of 106,012 m^2 forest land was recovered. Although maximum likelihood classification gave slightly better accuracy (41%) than SVM classification (39%), visual inspection of results showed that SVM classification created a more homogenous LULC map.

Keywords: Land Degradation, Geospatial Information Technologies, Remote Sensing, Geographic Information Systems (GIS), Coal Mining

ÖZ

TERKEDİLMİŞ BİR MADEN OCAĞI İÇİN JEOMEKANSAL BİLGİ TEKNOLOJİLERİ İLE ARAZİ BOZULMASININ DEĞERLENDİRİLMESİ

Emil, Mustafa Kemal
Y. Lisans, Maden Mühendisliği Bölümü
Tez Yöneticisi: Doç. Dr. Şebnem Düzgün,

Eylül 2010, 113 sayfa

Bu çalışma terk edilmiş bir kömür ocağı için jeomekansal bilgi teknolojileri kullanarak arazi bozulmalarının tayini için bir yaklaşım önermektedir. Arazi bozulması tayininin odağı iki temel değişim olan topoğrafik ve Arazi Kullanımı Arazi Örtüsü (AKAÖ) değişimleridir. Bu amaçla terkedilmiş Ovacık açık kömür madeni için stereo hava fotoğrafları, Worldview-1, Landsat ve ASTER uydu görüntüleri, Yersel Laser Tarama (YLT) verisi, Küresel Konumlandırma Sistemi (KKS) ölçme verisi ve yardımcı haritalar kullanılmıştır.

Topoğrafya ile ilgili kazı ve dolgu alanlarının hacmi, drenaj ağındaki sapmalar ve şev açısı değişimleri madencilik öncesi ve sonrasına ait 1950 ve 2009 yılları için hazırlanmış Sayısal Yükseklik Modellerinin (SYM) karşılaştırılması yöntemi ile tespit edilmiştir. Aynı tarihler için hava fotoğrafları ve Worldview-1 uydu görüntüsü temel alınarak AKAÖ haritaları hazırlanmıştır. Sonrasında, sınıflandırma sonrası karşılaştırma yöntemi kullanılarak AKAÖ değişimi alansal olarak hesaplanmış ve haritalanmıştır. Bunun yanında ASTER verisinden AKAÖ haritası elde edilmesinde maksimum olasılık ve Destekçi Vektör Makinesi (DVM) yaklaşımları incelenmiştir. Ayrıca, çalışma alanındaki mekansal değişimlerin tespit edilmesinde Landsat ve ASTER veri setlerinin birinci bantları ve Normalize Fark Bitki İndisi (NDVI) görüntüleri için görüntü çıkarma yöntemi uygulanmıştır.

Arazi bozulması değerlendirme sonuçları çalışma alanında önemli miktarda topoğrafik bozulma ve AKAÖ değişimi olduğunu göstermiştir. Özellikle SYM'lerinin çıkarılması sonucunda toplam hacmi 2,334,878 m^3 ‘ü bulan üç adet pasa sahası tespit edilmiştir. Birincil pasa sahası çevresindeki drenaj ağının maksimum 60 m yer değiştirme ile Güney yönünde kaymış olduğu fark edilmiştir. Bununla birlikte drenaj ağının kazı veya dolgu nedeni ile kesintiye uğradığı yerlerde çukurların oluştuğu ve böylelikle açık ocak göletinin ve küçük su birikintilerinin meydana geldiği gözlemlenmiştir. Eğim analizleri sonucunda 60 dereceden büyük açılı arazilerin yüzde 81'inin kazı alanı sınırları içerisinde olduğu ortaya çıkmıştır. AKAÖ değişimi analizleri 1950'den 2009'a kadar olan süreçte orman arazilerinin 106,485 m^2 azaldığını, buna rağmen pasa sahalarındaki ağaçlandırma çalışmaları sayesinde 106,012 m^2 orman arazisinin geri kazandırıldığını ortaya koymaktadır. Maksimum olasılık sınıflandırma yönteminin genel doğruluk oranının (41%) DVM sınıflandırma yöntemine göre (39%) daha iyi olmasına rağmen, sonuçların görsel incelemesi DVM sınıflandırma sonucunun daha homojen olduğunu göstermiştir.

Anahtar kelimeler: Arazi Bozulması, Jeomekansal Bilgi Teknolojileri, Uzaktan Algılama, Coğrafi Bilgi Sistemleri (CBS), Kömür Madenciliği.

To my father Hüseyin Emil

ACKNOWLEDGEMENTS

I would like to express my sincere appreciation and thanks to my supervisor Assoc. Dr. Şebnem Düzgün for providing me an opportunity to research under her supervision. I am highly indebted for her constant encouragement, continuous guidance and support.

I would like to express my thanks to Assist. Prof. Dr. Nuray Demirel for her contributions and valuable comments on this thesis study.

I also like to express my special thanks to all examining committee members for their valuable contributions and criticisms.

My sincere thanks also go to my colleague Mustafa Erkayaoğlu, Onur Gölbaşı, Mustafa Çırak, Ömer Erdem, and Selin Yoncacı for sharing their ideas and supports during my whole study period.

I would like to extend my sincere thanks to Mr. Erkan Baygül for his valuable help in point cloud preprocessing.

I would like to acknowledge METU Research Fund (BAP-07.02.2009.07) for providing financial support for this study.

I would like to express my special gratitude to all my family members for their encouragement and support in my chosen career path and for their love.

Finally, I would like to offer very special thanks to my fiancé Nazlı Uygun for her unshakeable love and support for the last thirteen years.

TABLE OF CONTENTS

LIST OF TABLES

TABLES

LIST OF FIGURES

FIGURES

CHAPTER 1

INTRODUCTION

1.1 Introduction

Coal mining operations make significant economic contributions to the society such as heating, electric production, and steel manufacturing. Coal is one of the most produced commodities in mineral industry. Total coal production in 2007 was 7036 million short tons over the world and 84 million short tons in Turkey (Energy Information Administration, 2008). According to World Coal Institute (2010), 40% of the total coal production is conducted by surface mining methods. Besides its operational advantages, surface mining results in more detrimental impacts on environment as compared to underground mining.

One of the prominent environmental impacts of the surface coal mining is land degradation which is described by Rödor and Hill (2009) as the reduction or loss of the biological or economical productivity of the land. For sustainable development, mineral industry faces with regulatory requirements forcing to assess land degradation around the mine sites and to remediate the mined-out areas. Minerals Council of Australia (2004), suggested an approach for prioritization of environmental impacts during reclamation planning. The first priority is always reduction of risks related to human health and safety. The second priority is the elimination of existing pollution sources. The third priority is to establish ecological balance and post-mining land use. The fourth priority is to meet public expectations.

The fifth and sixth priorities are satisfying esthetic concerns and reducing costs (as cited in Düzgün, 2009).

Monitoring and assessment of land degradation requires collection and comparison of data having spatial component representing environmental parameters such as pollution and land use. In this context, geospatial information technologies - Remote Sensing (RS), Geographical Information Systems (GIS), and Global Positioning Systems (GPS) - are of outstanding value. As Röder and Hill (2009) mention, remote sensing data, over three decades, provide essential base information for land degradation assessment with specific interpretation and modeling approaches. Rapid improvements in remote sensing technology allow users to obtain more accurate results with the help of higher spatial and spectral resolution images. Another geospatial technology, GIS, serves opportunity to the professionals in management of large amounts of spatial data and performing variety of spatial analysis supporting land degradation assessment. This study focus on implementation of these geospatial technologies to assess land degradation in Ovacık abandoned surface coal mine.

1.2 Objectives of the Study

The main objective of this research study was to assess mining-induced land degradation by investigating changes in topography and Land Use and Land Cover (LULC) using geospatial information technologies. The other objectives of this study were to evaluate existing re-vegetation works based on change detection algorithms and to test performances of land cover classification algorithms in a comparative manner for surface coal mines.

1.3 Outline of the Thesis

After introduction chapter of this research study, a literature survey was presented in Chapter 2 which is composed of environmental impacts of mining, overview on geospatial information technologies and literature survey on application of geospatial information technologies in mine monitoring, and land degradation assessment. After introducing the background, in Chapter 3, research methodology and case study was presented. Then, final comments were introduced in Chapter 4.

CHAPTER 2

LITERATURE SURVEY & OVERVIEW OF GEOSPATIAL INFORMATION TECHNOLOGIES

2.1 Environmental Impacts of Mining

Mining activities have the ability to cause widespread environmental damages as shown in Table 1. Most apparent environmental impacts of mining are land degradation, disturbance of forest and croplands, water table change, disturbance in surface water flow, erosion, subsidence, acid mine drainage, pollution in surroundings by discharges and waste disposal (Balkau, 1993).

Contaminations due to mining operations are classified as primary, secondary, and tertiary contaminations (Moore and Luoma, 1990). Sources of primary contaminants are the waste produced during mining, milling, and smelting and deposited near their origins. When these contaminants are transported through water or air, they generate secondary contamination in soil, ground water, rivers, and air. After deposition of these contaminants, if they remobilize and cause contamination in another place it is called tertiary contamination.

Potential water contaminants are acid mine drainage, heavy metals, cyanide, mercury, oils, fuels, and processing chemicals. These pollutants can result in serious damages to natural waterways, ground water, natural ecosystem, and clean water resources. There are different sources of wastes. Some of them are produced in great amounts having limited toxicity and some of them produced in small amount but are highly hazardous. Common wastes include overburden from the mine, gangue and waste rock from the milling, solid processing residues, and unused chemicals. These require special disposal and handling. Leaching from the dumpsites can cause water pollution and serious ecological consequences (Tören, 2001). Land cover change is another impact especially in surface mining. The extent of land cover change not only depends on time but also commodity and method of extraction. Coal mining, for example, is often a surface operation and cause larger land cover changes (Markus, 1997).

Progressive reclamation should be considered to manage environmental impact of mining. Geospatial information technologies have wide range of application in monitoring the mine environment.

Table 1 Potential environmental impacts of mining (Balkau, 1993)

Environmental impacts
• Destruction of natural habitat at the mining site and at waste disposal sites
• Destruction of adjacent habitats as a result of emissions and discharges
• Destruction of adjacent habitats arising from an influx of settlers
• Changes in river regime and ecology due to siltation and flow modifications
• Changes in land form
• Land degradation due to inadequate rehabilitation after closure
• Land instability
• Danger from failure of structures and dams
• Abandoned equipment, plants and buildings
Pollution impacts
• Drainage from mining sites, including acid mine drainage and pumped mine water
• Sediment runoff from mining sites
• Pollution from mining operations in riverbeds
• Effluent from mineral processing operations
• Sewage effluent from sites
• Oil and fuel spills
• Soil contamination from treatment residues and chemical spillage
• Air emissions from mineral processing operations
• Dust emissions from sites in close proximity to living areas and habitats
• Releases of methane (from coal mines)
Occupational/health impacts
• Handling of chemicals, residues and products
• Dust inhalation
• Fugitive emissions within the plant
• Air emission in confined spaces from transport, blasting and combustion
• Exposure to asbestos, cyanide, mercury or other toxic materials used on-site
• Exposure to heat, noise and vibration
• Physical risks at plants or on-site
• Unsanitary living conditions

2.2 Geospatial Information Technologies

Remote Sensing (RS)

"Remote sensing is the science (and to some extent, art) of acquiring information about the Earth's surface without actually being in contact with it. This is done by sensing and recording reflected or emitted energy and processing, analyzing, and applying that information." (http://ccrs.nrcan.gc.ca).

Aerial photos taken during World War I are the first remote sensing applications. Since then there is an incredible development in remote sensing technology. Now, there are many Earth Observation satellites on earth orbit having different specifications and there are also many airborne cameras being used in many applications. Remote sensing is used in various fields, such as, meteorology, oceanography, vegetation monitoring, land use land cover mapping and change detection, cartography, disaster monitoring, hydrology, city and regional planning, mineral exploration, and environmental monitoring.

Canada Centre for Remote Sensing (2008), defines seven elements of Remote sensing systems involve illustrated in Figure 1.

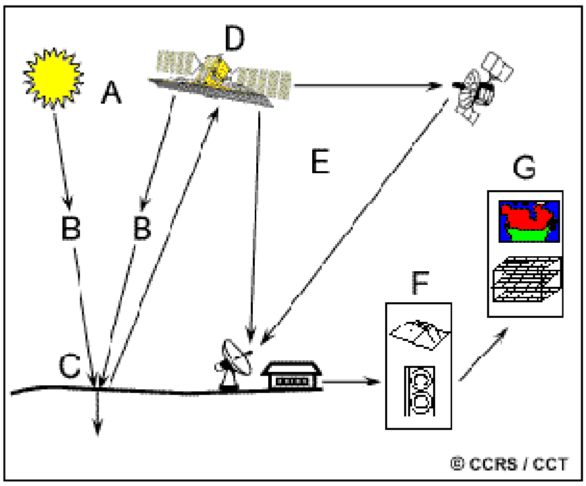

Figure 1 Elements of remote sensing (Canada Centre for Remote Sensing, 2008)

The first requirement for remote sensing is *Energy Source or Illumination (A)* and it provides illumination or electromagnetic energy to the area of interest. The second element is *Radiation and the Atmosphere (B)* as the energy travels from energy source to the area of interest. After it comes in contact with the target, it also interacts with the atmosphere during its back travel to the sensor. The third element, *Interaction with the Target (C),* is the interaction between target and the radiation regarding the properties of the radiation and the target surface. The fourth element is *Recording of Energy by the Sensor (D)*. After the radiation has been scattered by the target, it is needed to be collected the radiation scattered by a remote sensor. The fifth element is *Transmission, Reception, and Processing (E)* and covers the transmission of recorded energy in electronic form to a receiving and processing station where the data are converted to an image. The sixth remote sensing element, *Interpretation and Analysis (F)* is information extraction about the area of interest from the processed image. The last element, *Application (G),* is the final element of the remote sensing process and it entails application of imagery to better understand the area of interest, create new information or solve a specific problem. These seven elements constitute the process of remote sensing from beginning to end.

There are mainly two types of remote sensing: active and passive. Remote sensing systems which measure energy that is naturally available are called passive sensors. Source of this energy is generally sun radiation. Active sensors, on the other hand, provide their own energy source for illumination. The sensor emits radiation which is directed towards the target to be investigated. The radiation reflected from that target is detected and measured by the sensor.

The digital images acquired by satellite sensors are composed of pixels representing the brightness of each area with a numeric value or digital number shown in Figure 2. Computers display each digital value as different brightness levels. The information from a narrow wavelength range is gathered and stored in a channel, also sometimes referred to as a band. We can combine and display channels of information digitally using the three primary colors (blue, green, and red).

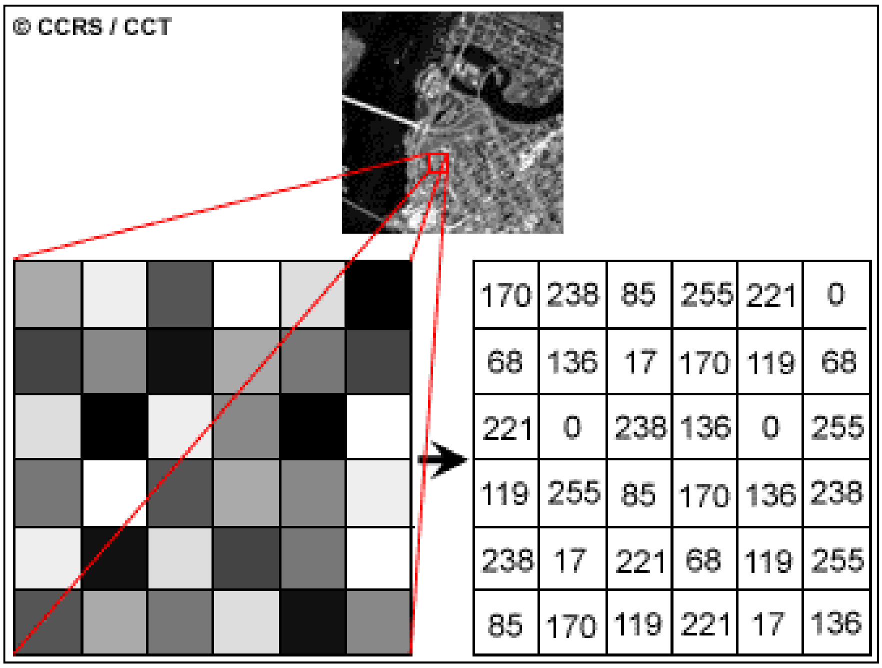

Figure 2 Pixel and Digital Number (DN) in a remotely sensed image (Canada Centre for Remote Sensing, 2008)

Geographic Information Systems (GIS)

GIS describe any information system that integrates, stores, edits, analyzes, shares, and displays geographic information (Clarke, 1986). GIS applications are tools that allow users to create interactive queries (user created searches), analyze spatial information, edit data, maps, and present the results of all these operations. Following elements are required to be able to run GIS: a computer, software, output devices; including a monitor and a printer, and finally a human operator. GIS uses relational database management system to store, retrieve and analyze data layers simulating real word shown in Figure 3.

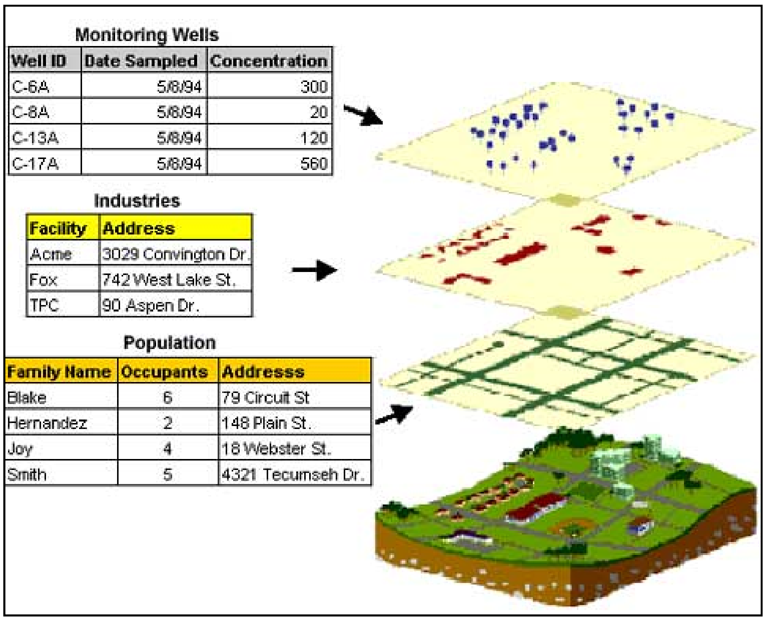

Figure 3 Layer structure of GIS (Environmental Protection Agency US, 2006)

Supervised Image Classification

Classification algorithms simply try to assign pixels to the classes by analyzing similarity between spectral signatures of individual pixel or similarity. In spectral classification approach, signatures obtained from the training samples are used to train the classifier to classify the spectral data into a classified thematic map. There are some key points in classification of remotely sensed imagery. The first is the selection of suitable classification system. This depends on purpose of classification and the data available. The second is the selection of training set. A sufficient number of training samples and their representativeness are critical for image classifications (Mather, 2004).

Maximum likelihood classification

Maximum likelihood classification is the most common supervised classification method used for remote sensing image data. The algorithm assumes that the statistics for each class in each band are normally distributed and calculates the probability that a given pixel belongs to a specific class. Unless a probability threshold is not selected, all pixels are classified. Each pixel is assigned to the class that has the highest probability (that is, the maximum likelihood). If the highest probability is smaller than given threshold, the pixel remains unclassified (ENVI 4.7 Help Menu). However, this approach does not take contextual information about the neighboring classes due to its pixel by pixel classification approach. Increased information provided by the spatial extent of the classes of the neighbors tends to mitigate the effects of noise, isolated pixels, and individual pixels (Castro-Esau, 2004).

Support Vector Machine (SVM) classification

SVM is a classification system derived from statistical learning theory. It separates the classes with a decision surface that maximizes the margin between the classes. The surface is often called the optimal hyperplane, and the data points closest to the hyperplane are called support vectors. SVM classification output is the decision value of each pixel for each class, which is used for probability estimates. SVM performs classification by selecting the highest probability. SVM includes a penalty parameter that allows a certain degree of misclassification, which is particularly important for non-separable training sets (ENVI 4.7 Help Menu). SVM does not require any assumption about the data and do not employ statistical parameters to calculate class separation. This method is especially suitable for incorporation of non-remote-sensing data into a classification procedure (Lu and Weng, 2007).

Change Detection

Change detection is simply the identification of differences in the state of a phenomenon by observing it at different points of time. Previous literature indicated that image differencing, principal component analysis, and post-classification comparison are the most common methods used for change detection (Lu et al., 2004). They report that, in practice, different algorithms are often compared to find the best change detection results for a specific application. Change detection was performed to monitor the environmental impacts induced by land degradation, deforestation, and pollution.

2.3 Overview of Geospatial Information Technologies in Mine Monitoring and Land Degradation Assessment

2.3.1 Remote Sensing Applications

Utilization of remote sensing in mining industry begins with interpretation of aerial photographs for surface mine monitoring mainly aiming to detect temporal and spatial changes in mine sites (Anderson, 1977). Earlier studies using imagery acquired by first Earth Observation (EO) satellite Landsat Multispectral Spectral Scanning (MSS) did not give successful results due to low spatial resolution of the sensor (Irons and Kennard, 1986). After the availability of higher resolution Landsat Thematic Mapper (TM) imagery conjunction with aerial photographs and MSS images it was possible to analyze land cover classes around mine sites and monitor changes caused by mining activities (Woldai, 2001).

Tören (2001), used Landsat TM imageries to detect mining induced environmental impacts around Soma open pit coal mine by change detection methods. It is found that between the years 1989 and 1999 forest area increased an amount of 17.7 km^2 due to forestation efforts and bareland area decreased 10.5 km^2. Other important result was the detection of 37.3 km^2 decrease in cultivated areas due to expanded mining activities in the site.

Woldai and Taranik (2008), using InSAR data integrated with ground water pumping data, site geology, soil data, and Landsat and ASTER images, assessed the ground surface deformation and environmental impacts for an operating open-pit mine where intensive dewatering was performed during 1996-2001. They were able to detect subsidence and uplift resulting from subsurface volumetric shrinkage induced by ground water pumping with an accuracy of a few centimeters.

SPOT imagery which is used for many researchers especially for plant monitoring, Land Use and Land Cover (LULC) mapping, pollution monitoring have been used also for mine monitoring. Mularz (1998), using SPOT imagery with Landsat and aerial photographs, monitored Land Use and Land Cover (LULC) changes over the lignite open cast mine and power plant area and evaluated reclamation activity on overburden dump area using post classification comparison technique. Combination of SPOT and Landsat images was able to discriminate conifer forest, deciduous forest, grass-urban, crop-land, and baregrounds.

Erdoğan (2002), using SPOT satellite imagery taken 1987 and 1999, monitored the changes in Göynük lignite mine in terms of areal extent of stripping. Volumetric changes due to overburden excavation and dumping was calculated by DEM overlay method. The total area that has changed due to mining activities was found as 48.3 km^2 by band differencing algorithm. Additionally, land use map of the research area was extracted by using maximum likelihood classification method with an 88% overall accuracy.

Ganas et al. (2004), used earth observation data in a decision support system to facilitate development of restoration plans for an open-cast nickel mine. SPOT stereo pairs, Landsat and high resolution KVR-1000 panchromatic images are used successively for extraction of topography with a 15.7 m RMS error, classifying land cover with around 95% overall accuracy, and ground truth information.

Post classification comparison of Landsat TM and ETM+ images were investigated to find out temporal and spatial extent of environmental degradation from 1986 to 2000 in the Tarkwa mining area (Manu et al., 2004). They concluded that over 60% of the land was degraded to the point where it could not be used for any commercial activity and 35,000 ha of land has been polluted by mining activities in Tarkwa. In this research, land degradation was considered as either loss of vegetation or complete removal of overburden.

There are also considerable efforts to monitor re-vegetation studies by remote sensing. Abuelgasim et al. (2005) using multi-temporal Landsat TM data set spanning a period of 20 years evaluated the success of the restoration program by comparing Normalized Difference Vegetation Index (NDVI) and land cover information extracted from imagery in Sudbury, Canada. Results of investigations showed that vegetation cover reasonably expanded in size for a larger number of restoration sites whereas some of re-vegetated sites showed little or no progress.

Pavelka and Halounová (2004) utilizing Landsat TM and IKONOS images were able to assess the success of reclamation on forest, agriculture and grass land based on comparison of vegetation indices. IKONOS images were used for detailed evaluation of tree species of forest reclamation to determine their individual growth quality. Lévesque and Staenz (2004) investigated airborne hyperspectral remote sensing to evaluate re-vegetation of mine tailings by using Compact Airborne Spectrographic Imager (CASI) data. The study area was classified as water, lime, fresh and oxidized tailings, and low and high photosynthetic vegetation. During classification, ground-based spectra and spectral libraries were used in K-Mean unsupervised classification algorithm and obtained a 78.1% overall accuracy.

Image rationing and differencing has also been used to extract land cover changes in the monitoring of environmental impacts of mining. Prakash and Gupta (1998) investigated land cover change detection based on these techniques and described image characteristics of mine features on black and white and color composites images of Landsat TM and differentiated land cover classes and identified land cover changes which were caused by mining and reclamation studies in their study area.

Nori et al. (2008) using post classification comparison technique on Landsat ETM+ and ASTER images for land cover change detection was able to map changes on land cover between 2003 and 2006. It was found that, grass land has decreased whereas the area of close forest and open forest has increased within this period.

2.3.2 Geographic Information Systems (GIS) Applications

In almost all above researches, GIS was used to manage, manipulate and analyze datasets utilized which would be raw and enhanced images, land cover maps created and other ancillary data like the field measurements and various maps in differing extends. However, researches below are prominent regarding application of GIS in monitoring, land degradation assessment, and reclamation planning in mineral industry.

Duong et al. (1999) used GIS to investigate the cumulative impacts of the development of different economic sectors including coal mining in Ha Long Bay in Vietnam. They constructed a database composed of dataset, satellite imagery and aerial photographs, ecology and habitats, topographical base map, population, Land Use and Land Cover (LULC), coal mining, Digital Elevation Model (DEM) and tourism facilities in the study area. The aim was to generate impact scenarios of different development and rehabilitation alternatives. They underlined the necessity of database establishment and detected around 148 km^2 deforestation for different purpose. The effect of realization of master development plan was evaluated and tabulated. GIS analyses showed that 20.5% of the mangrove area and 13.5% of the human settlements area would be affected at the end of full realization of the master development plan.

Investigation of surface topography change caused by mining activities using RS and GIS is an important part of environmental monitoring and make possible to detect undocumented and unauthorized valley fills. Shank (2004) using multi-date elevation data, Interferometric Synthetic Aperture Radar (InSAR) and Digital Line Graph (DLG) hypsography, researched on developing of a spatial inventory of mining fills. Due to low penetrating tree canopy capability of InSAR data, before comparison of topography, a forest/non-forest land cover classification was conducted using satellite imagery and forest mask prepared to exclude forested areas from analysis. GIS analysis tools were utilized to calculate fill characteristics such as area, volume, maximum depth, and length of buried stream. Results indicated the presence of over 500 fills that were not represented in an existing fill inventory digitized from permit maps. Inventory of mining cut and fill features were determined over a large area.

Ganas et al. (2004) constructed a Decision Support System (DSS) based on remote sensing and GIS, which aims to answer the questions where to restore and what will be the new land use by evaluating different strategies based on multiple criteria supplied by the user like slope, aspect, and previous land cover. The method was to overlay multi-criteria raster dataset and weighting it. The author concluded that the DSS was successful in modeling landscape restoration by selecting dump sites and applying correct measures such as terrace creation and tree planting.

Using RS, GIS and 3D modeling tools, Hill (2004) was able to model several open pit mines in 3D around Pennsylvania’s anthracite region to get accurate volume measurements for backfill and spoil volumes. The aerial photography was preferred considering cost efficiency instead of very high spatial resolution satellite imagery.

Digital photogrammetric techniques were applied to extract x, y, z coordinates of landforms from aerial photographs. Then 3D point data pre-reprocessed in GIS to removed suspicious points which are not representing earth surface prior to 3D modeling of mine features and assess suitability of applied restoration to reclamation plans. The mines were evaluated with respect to reclamation liability based on comparison of reclamation plans and volumetric calculations conducted in 3D modeling tool.

Behum (2004), used GIS as LIDAR data processing tool and detailed topographical mapping for the design of passive Acid Mine Drainage (AMD) treatment facilities in Oklahoma. Use of aerial photography found to be adequate instead of LIDAR for the areas devoid of heavy brush and woodland considering time and cost factors.

Antwi et al. (2008), beyond the LULC change, worked on habitat diversity change based on LULC patterns in post-mining area Schlabendorf Süd in Lower Lusatia. Using GIS and Landsat imagery, it is found that disturbance in land due to mining activity increased the fragmentation and habitat diversity in post-mining landscape.

Hydrological analysis is one of the widely used applications within GIS to extract drainage characteristics. Choi et al. (2008) demonstrated a research on flood and gully erosion at Pasir open pit coal mine in Indonesia using hydrological tools of GIS. It was able to determine the bench slopes that were most vulnerable to gully erosion and to decide optimal pump locations to reduce the risk of flooding during heavy rainfall in Pasir open pit coal mine.

CHAPTER 3

RESEARCH METHODOLOGY & CASE STUDY

3.1 Research Methodology

In this research an integrated methodology, illustrated in Figure 4, was applied for land degradation assessment of abandoned surface coal mines by mainly pointing out topographical disturbances, and Land Use and Land Cover (LULC) changes in the abandoned site. The research methodology was based on geospatial technologies, Remote Sensing (RS), Geographic Information Systems (GIS), Global Positioning Systems (GPS) and Terrestrial Laser Scanner (TLS) field surveys for land degradation assessment. The methodology is composed of three main parts. The first is *data collection* for both pre- and post-mining stages of the abandoned mine site. The second is *data processing* to prepare raw data to further land degradation analysis. The third part, *analysis of land degradation* aims to assess land degradation caused by mining activity using prepared data in the data processing step.

Data Collection

The aim of the data collection is to collect any available data belonging to pre- and post-mining stages of the abandoned mine to form a base for further analyses. There are several available data sources that can assist the methodology. These are multi-temporal satellite imagery and aerial photos, Global Positioning System (GPS) and Terrestrial Laser Scanner (TLS) surveys, various thematic maps (such as Geological, LULC and Topographical maps), reports and on site observations.

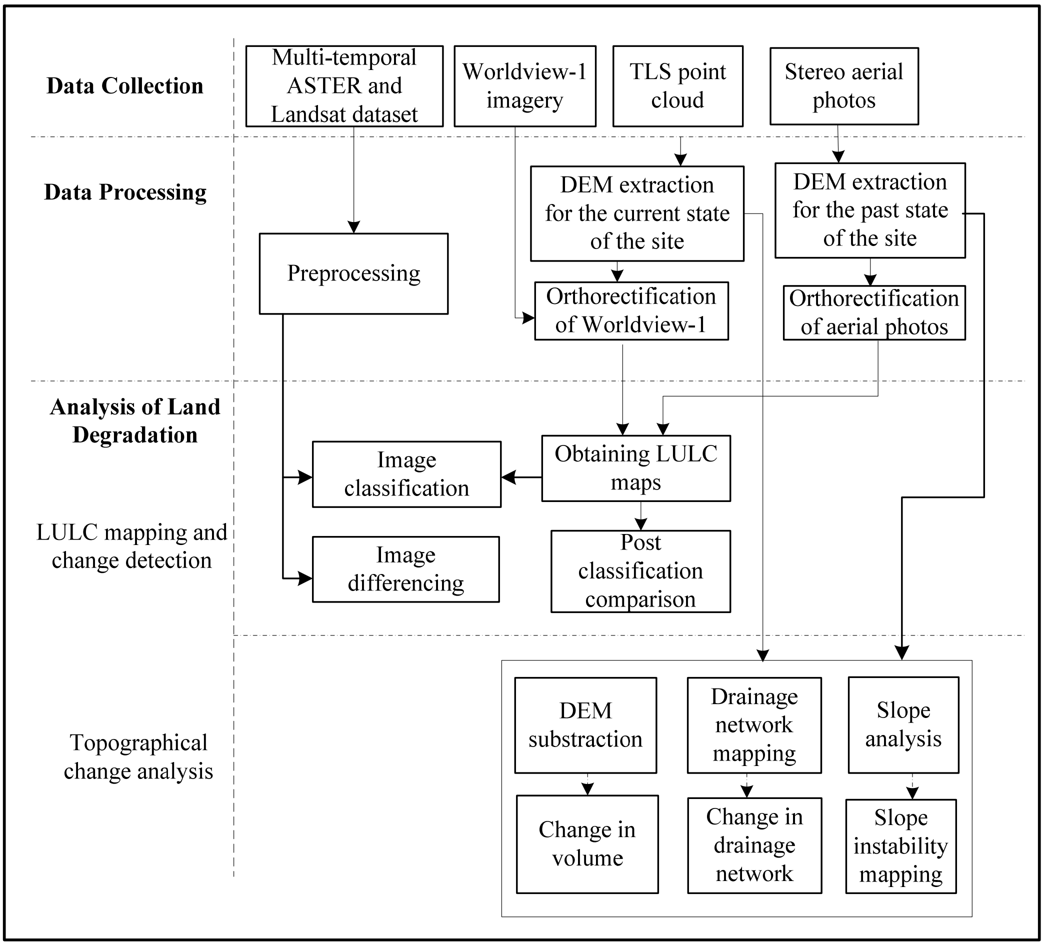

Figure 4 Illustration of research methodology

Data Processing

The dataset is required for data management and processing tools. There are software available for management and processing of each type of data: image processing software for satellite imagery, Geographic Information System (GIS) software for thematic maps and tabulated spatial data and point cloud processing software for Terrestrial Laser Scanner (TLS) data.

There are many data processing steps according to processing level of obtained data. For example, satellite imagery need to be corrected atmospherically and geometrically and orthorectified before image classification or change detection procedures. It is needed to generate some other data from raw data to use in further steps of methodology as generating a Digital Elevation Model (DEM) from stereo aerial photos to be used in topographical change analysis.

Analysis of Land Degradation

There are different land degradation processes to be analyzed for different abandoned mines depending on local settings. Deforestation, topographical deformation, LULC change, pollution, acid mine drainage are some of these degradations. In this research, changes in drainage network, slope instability, changes in LULC were investigated. In the analysis of land degradation step, image classification, change detection, slope mapping, drainage network mapping methods were applied by geospatial information tools.

3.2 Case Study Area: Abandoned Ovacık Coal Mine

General Information about the Research Area

The study area is in Ovacık, Yapraklı, Çankırı which is located in northern Turkey about 140 km northeast of Ankara, the capital of Turkey as shown in Figure 5. Rough terrain is observed in topography with an average elevation of 1300 m. The climate of the area is terrestrial with a mean annual rainfall of 394 kg/m^2 (Turkish State Meteorological Service, 2010). The main land use in the research area is forest with pine and oak trees. There are also small agricultural areas around the villages. Barelands are also observed in the research area. There are also mining induced land uses like open pit excavation, dump sites (both afforested and not afforested) and remnants of coal stock site. The current abandoned mine layout can be seen in Figure 6. The coal seam operated in the Ovacık coal mine has 0.3-0.8 m thickness with a 75-80 degree inclination. Calorific value of the coal has been determined as 4500-5000 kcal/kg.

Figure 5 Location of study area

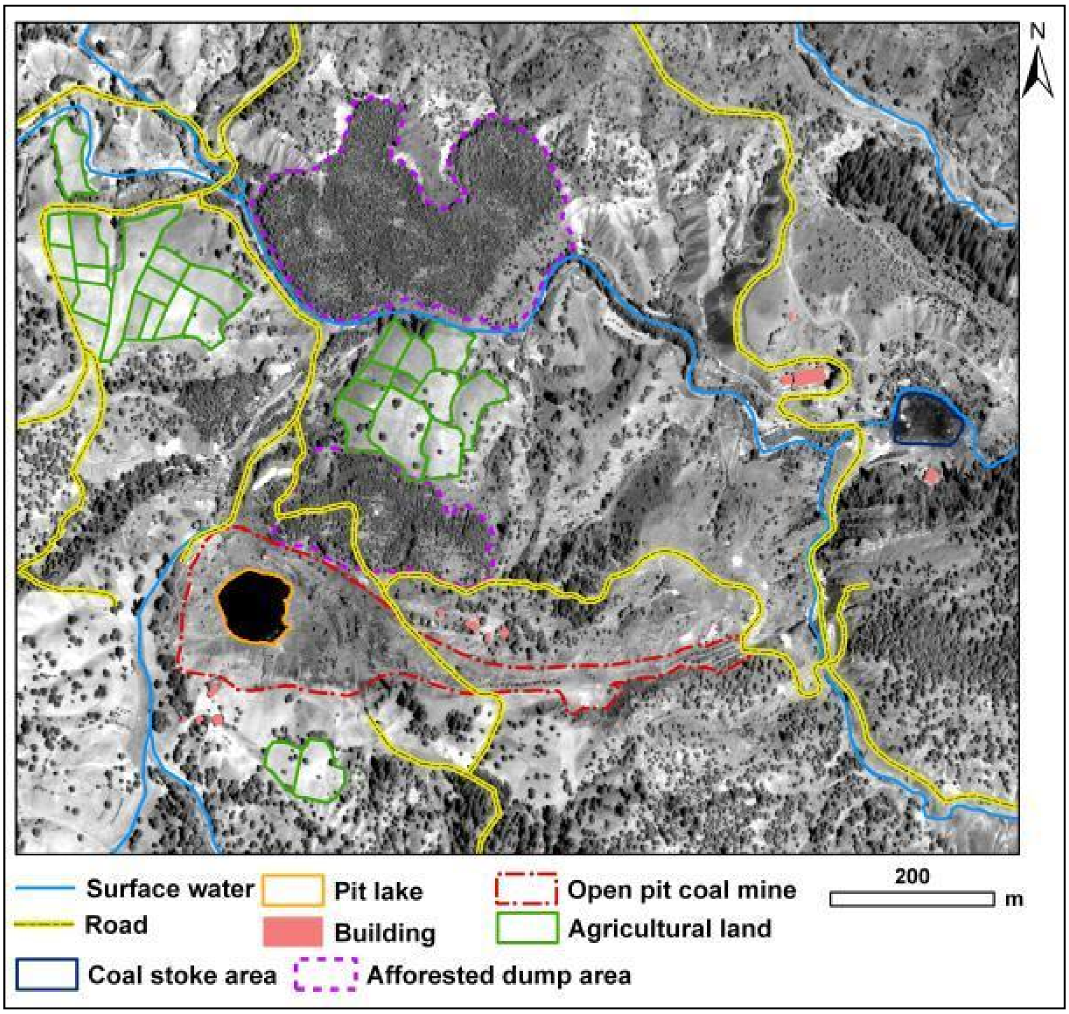

Figure 6 Current Ovacık coal mine layout overlaid with Worldview-1 satellite imagery

History of the Ovacık Coal Mine

In the Ovacık coal mine, both underground and surface mining methods has been applied. Proven coal reserve is determined by explorations conducted by General Directorate of Mineral Research and Exploration (Maden Tetkik ve Arama Genel Müdürlüğü - MTA). The first application for concession was made on March 4, 1987 by Köseoğlu Mining Company. According to the company's project report (1987) submitted to General Directorate of Mining Affairs (MİGEM), proven reserve was calculated as 144,000 tons of coal and the mine was planned to operate

72 years with an annual production rate of 20,000 tons of coal. During the operations, new coal seams were discovered and started to be excavated. Till the end of 1999, 224,440 tons of the coal were produced by surface and underground mining methods. In addition, there were 68 workers in the mine while it was operated by Köseoğlu Mining Company. The company stopped production in June 2005. After a short period of time -in 2005- the production rights were given to Uzay Yolu Mining Company. Hence, the company claimed that there is no production of coal since they have the rights. The concession was canceled on February 2008. The field has been put out to tender.

3.3 Problems Related to Ovacık Coal Mine

The following problems related to land degradation and safety were observed in the study area after several field trips.

- Open pit void was left as it is after the operation stopped without any stability and safety measures. There are high slopes around the pit. The pit is filled with water during the whole year (Figure 7).
- There were indications of acid mine drainage near old underground mine entrances (Figure 8).
- Dump sites were formed by dumping overburden to river bed which were afforested after some grading effort of General Directorate of Forestry by planting locust trees in early 1980's. However, slopes of dump sites were not been terraced or planted so erosional formations -gully and rill- exist in the slopes (Figure 9).
- Some mine facilities like entrances of underground openings, coal loading units have been demolished and sealed. However, some buildings like administration and coal storage were left without taking any measures consequently damaged and flooded partly (Figure 10 and Figure 11).

* Illegal openings were observed within the open pit, especially where the highest slopes exist. These adits are driven by nearby villagers to conduct small scale coal production (Figure 12).

Figure 7 A scene from abandoned open pit with surrounding high slopes

Figure 8 Acid mine drainage around old mine entrance

Figure 9 A view from slope of the dump site showing erosional processes (rill formation)

Figure 10 Abandoned administration building

Figure 11 Flooded coal storage building

Figure 12 One of the entrances for illegal coal production conducted by villagers

3.4 Data Collection

All data set utilized throughout this research are listed in Table 2 with related information of data format, data source and date of creation for each data type. Data set can be divided into six categories as aerial photographs, satellite imagery, 3D Terrestrial Laser Scanner (TLS) data, Ground Control Points (GCP) obtained by GPS survey, and ancillary maps.

Table 2 Collected data for the Ovacık coal mine

Data Type	Format	Source	Date
Aerial Photographs (RMK 10/18)	TIFF	HGK*	1951
Aerial Photographs (RC 5)	TIFF	HGK	1971
Aerial Photographs (RC 10)	TIFF	HGK	1990
Landsat-2 (MSS) Imagery	TIFF	GLCF**	12.09.1975
Landsat-5 (TM) Imagery	TIFF	GLCF	27.07.1987
Landsat-7 (ETM+) Imagery	TIFF	GLCF	06.07.2000
Terra (ASTER) Imagery	HDF	NASA***	17.11.2002
Terra (ASTER) Imagery	HDF	NASA	12.09.2007
WorldView-1 Imagery	TIFF	DigitalGlobe Inc	22.08.2008
Forest Map	TIFF	OGM****	–
Jeological Map	e00	MTA*****	1988
Topographic Map	TIFF	HGK	1992
Topographic Contour Map	ADF	HGK	1992
Terrestrial Laser Scanner Data	ASCII	Field Works	27.07.2009 11.10.2009 18-20.11.2009
Ground Control Points (GCPs)	ASCII	Field Works	04.07.2009 11.10.2009 22.11.2009 15.04.2010

* General Command of Mapping (HGK)
** Global Land Cover Facility (GLCF)
*** National Aeronautics and Space Administration (NASA)
**** General Directorate of Forestry (OGM)
***** General Directorate of Mineral Research and Exploration (MTA)

Aerial Photographs

Historical aerial photo sets were obtained in digital format after being scanned from General Command of Mapping (HGK) to get Land Use and Land Cover (LULC) and topographical situation before mining operation has been started in the study area. The flights took place in 1951, 1971, and 1990, capturing black and white air photos with scales of 1:35000, 1:20000, and 1:40000 respectively. Also, the coverage of air photos with air photo centers are displayed in Figure 13. Photo boundaries given in Figure 13 were drawn using photo corner coordinates supplied from HGK and they approximately represent real ground coverage. As seen in Figure 13, between photo pairs in the same flight line, there are 60% overlaps allowing to create stereo models. The stereo aerial photo pair captured in 1951 was selected for the extraction of pre-mining topography and LULC for the present study.

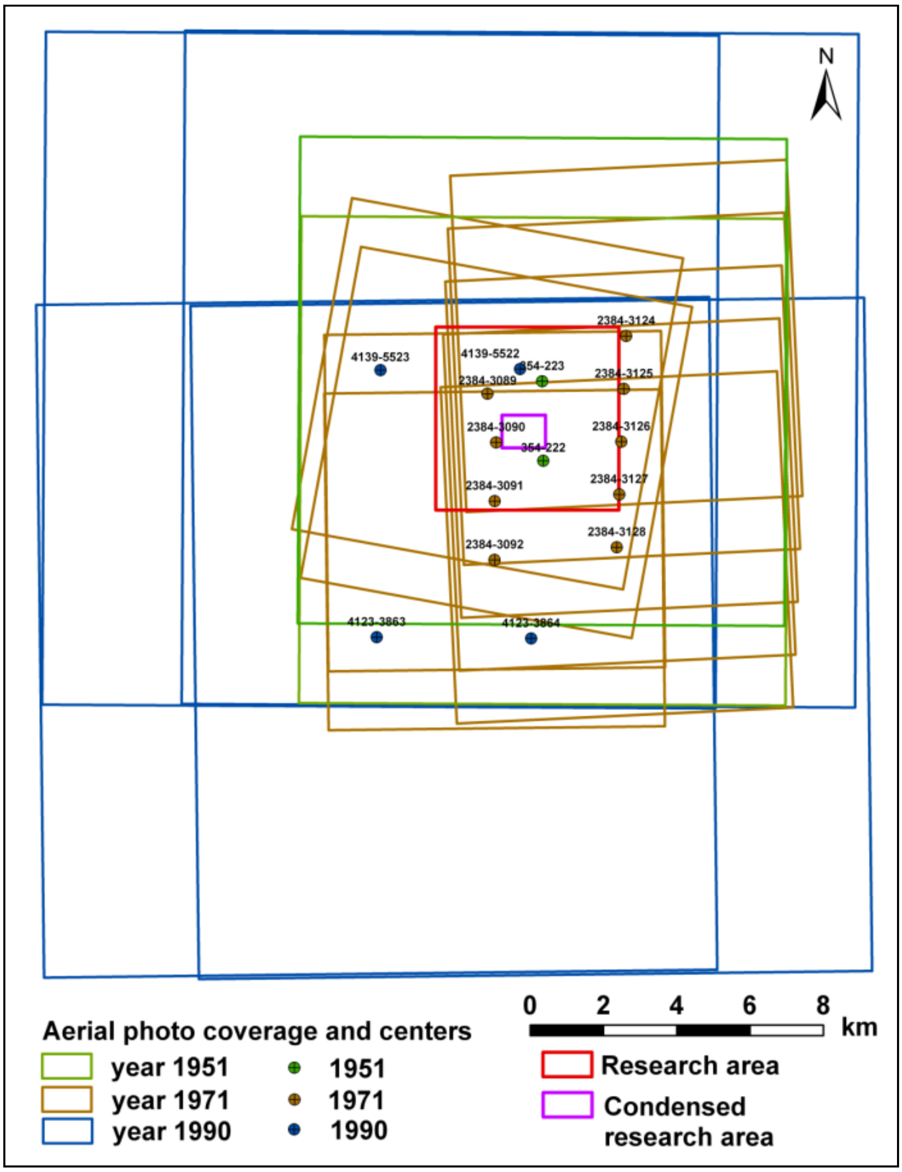

Figure 13 Aerial photo coverage and photo centers and research area

Satellite Imagery

Mainly, three types of satellite imagery having different specifications were utilized in this study. Satellite sensors and corresponding imagery specifications were listed in Table 3.

Table 3 Specifications of satellite sensors used in this research.

Landsat MSS				
Bands	1	2	3	4
Wavelength(μm)	0.50-0.60	0.60-0.70	0.70-0.80	0.80-1.10
Spatial resolution(m)	57	57	57	57

Landsat TM							
Bands	1	2	3	4	5	6	7
Wavelength(μm)	0.45-0.52	0.52-0.60	0.63-0.69	0.76-0.90	1.55-1.75	10.40-12.50	2.08-2.35
Spatial resolution(m)	28.5	28.5	28.5	28.5	28.5	28.5	28.5

Landsat ETM+								
Bands	1	2	3	4	5	6	7	8(Pan)
Wavelength(μm)	0.45 - 0.52	0.53 - 0.61	0.63 - 0.69	0.78 - 0.90	1.55 - 1.75	10.4 - 12.5	2.09 - 2.35	0.52 - 0.90
Spatial resolution(m)	28.5	28.5	28.5	28.5	28.5	57	28.5	14.25

Aster		
Bands	Wavelength(μm)	Spatial resolution(m)
1	0.52-0.60	15
2	0.63-0.69	15
3N	0.78-0.86	15
3B	0.78-0.86	15
4	1.60-1.70	30
5	2.145-2.185	30
6	2.185-2.225	30
7	2.235-2.285	30
8	2.295-2.365	30
9	2.360-2.430	30
10	8.125-8.475	90
11	8.475-8.825	90
12	8.925-9.275	90
13	10.25-10.95	90
14	10.95-11.65	90

WorldView-1	
Bands	1(Pan)
Wavelength(μm)	0.40 to 0.90
Spatial resolution(m)	0.5

Freely available Landsat data archive for the study area is searched via a web portal which is Earth Science Data Interface (ESDI) at Global Land Cover Facility (GLCF) organized by University of Maryland (2004). Among the Landsat time series overlaid with the research area, three image sets were selected and downloaded acquired in the same season –which is favorable in Land Use and Land Cover (LULC) studies- by different Landsat sensors namely MSS, TM and ETM+ respectively in the years 1975, 1987 and 2000. As seen in Figure B1, the research site covers relatively a small area and it was located northern part of the full scene Landsat MSS image. For the Landsat TM and Landsat ETM images, research area was located in northwest of the full scene imagery shown in Figure B2 and Figure B3 respectively. Landsat images were used in change detection procedure in order to assess their effectiveness in delineating mining induced changes.

Two Imagery sets acquired by Advanced Spaceborne Thermal Emission and Reflection Radiometer (ASTER) sensor in Terra satellite were obtained and included in the imagery database with the observation dates in 2002 and 2007 at level 3A which is an orthorectified product of ASTER data. Figure B4 shows relative extent and position of the research area to the full scene ASTER imagery taken in 2002. As seen in Figure B5, the ASTER imagery taken in 2007 partially covers the research area. ASTER images were used in LULC classification and change detection stages of the research.

For mapping, visualization, and validation purposes very high spatial resolution imagery was needed. Quickbird and Worldview-1 images were found to be available in data archives. However, due to high cloud coverage of Quickbird imagery, Worldview-1 panchromatic (B&W) imagery, displayed in Figure B6, was obtained. Specifically the Worldview-1 imagery was used for two main purposes; to map current LULC and to extract road network and mine layout of the site.

3D Terrestrial Laser Scan Survey

A three dimensional (3D) Terrestrial laser scan survey was conducted using the instrument Optech ILRIS-3D laser scanner on the research site shown in Figure 14 . Instrument consists of a scanner, tilt unit, tripod, control unit (pocket pc), and power supply. The results of scan are millions of points known as “point cloud”, which are 3D (X, Y, Z) representation of the scanned terrain with respect to the scanner position. Table 4 shows the specifications of the Optech ILRIS 3D Terrestrial laser scanner.

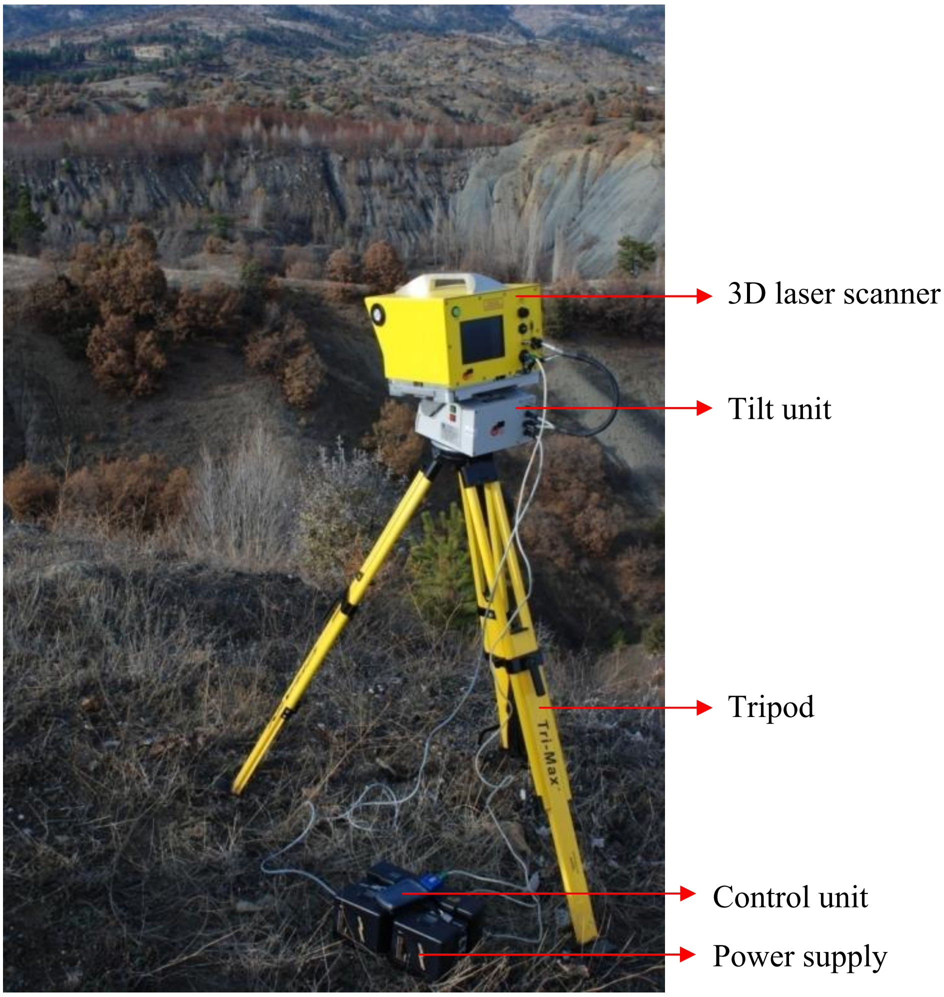

Figure 14 Optech ILRIS-3D laser scanner during scanning near dump site. Instrument parts are shown from top to bottom as scanner, tilt unit, tripod, control unit and power supply

Table 4 Specification of the Optech ILRIS 3D Terrestrial Laser Scanner

Parameters	Unit	Optech ILRIS 3D
Scanning range (80% target reflectivity)	m	1,500
Data sampling rate	points/second	2,500
Beam divergence	degree	0.00974
Minimum spot step (X and Y axis)	degree	0.00115
Raw range accuracy 100 m	mm	7
Raw positional accuracy at 100 m	mm	8
Laser wavelength	nm	1,500
Laser class		Class 1 (eye safe)
Scanner field of view	degree	40 x 40

Due to rough terrain and tree cover in the site, it was difficult to fully record the study region. After an initial scan survey plan, the plan was updated to locate next scanning location by inspection of resulted point cloud cover after each field work. Scan survey had to be finalized after 5 days of field work with 12 scan locations due to time and budget limitations. The point clouds obtained by 12 scan locations were merged and geo-referenced in UTM projection with WGS1984 datum within Polyworks 10 software environment. An oblique display of point cloud is given in Figure 15 showing open pit from west and surface features like trees and erosional rill formations are discernable in the scene. The processing of this point cloud data was highly computationally intensive.

Data was cleaned from noises which were erroneously recorded points above surface and the points recorded below water surface across shoreline of the open pit lake where water is shallow enough for the laser beam to reflect from the bottom of the lake. The point cloud has 157 millions points after noise reduction with average point spacing of 14 cm. This huge data set occupies 6972 MB storage space in the format of ASCII text.

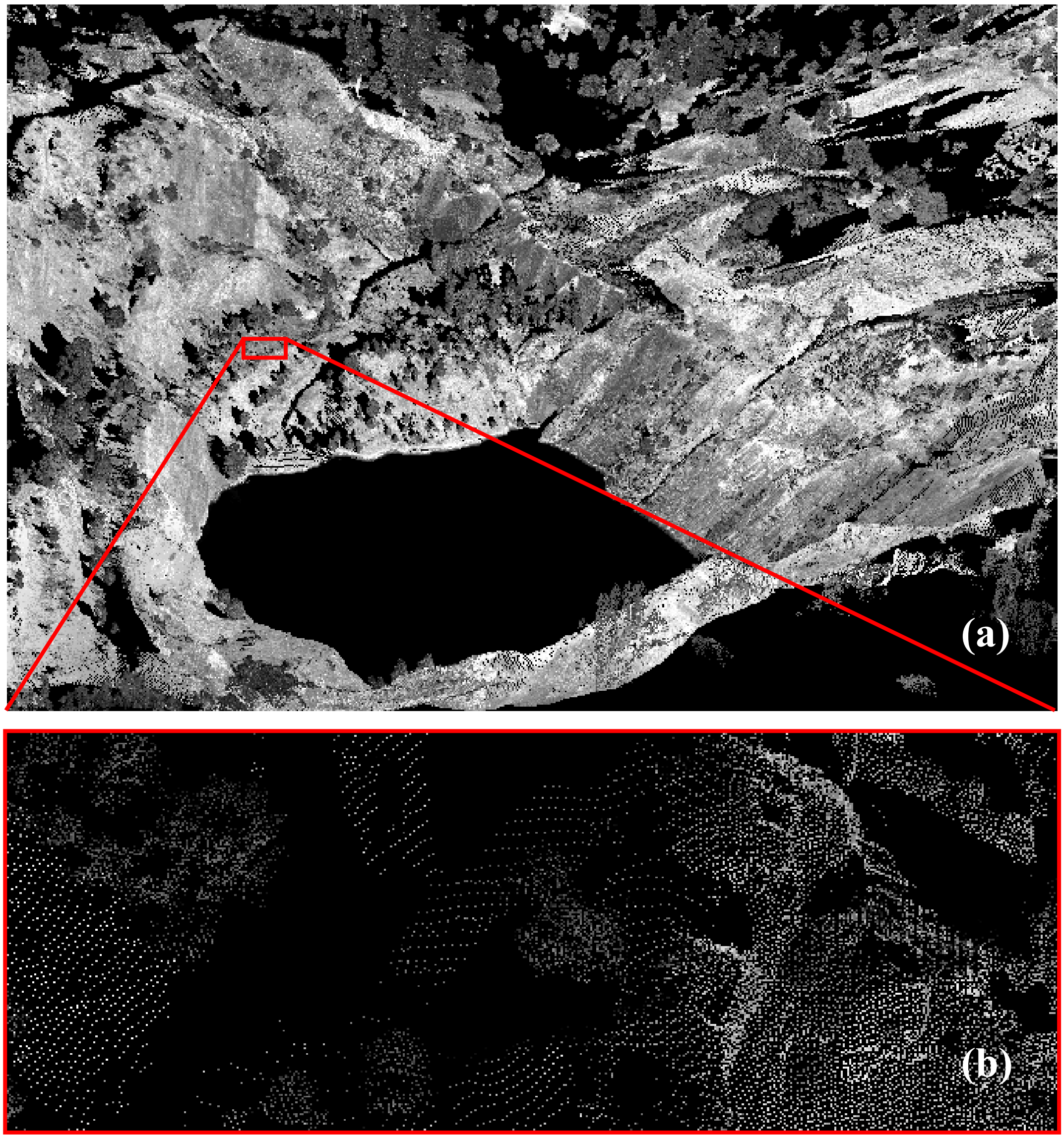

Figure 15 An oblique view of point cloud showing open pit looking from west (a) and close view of point cloud (b)

The terrestrial laser scan survey was conducted to gain current topography of the research site in detail. Point cloud recorded in scan survey was used to produce current Digital Elevation Model (DEM) to detect topographical changes such as volumetric, drainage network and slope comparing with pre-mining topography.

Global Positioning System (GPS) Survey

Throughout the research 3 Global Positioning System (GPS) receivers were utilized depending on device availability and accuracy level needed for ongoing purpose of data collection.

Table 5 shows GPS instruments used with basic specifications. In this research, Topcon GR3 receiver was used in Real time Kinematic mode which gives the highest accuracy (centimeter level) by employing both the reference station correction and carrier phase signals from GPS satellites (Blanco et al., 2009). On the other hand, Topcon GRS-1 and Septentrio AsteRx1 GPS receiver were used in DGPS mode which have relatively lower accuracy (tens of centimeters) by employing differential correction from a static reference station with known fixed position (Blanco et al., 2009).

Table 5 Specifications of GPS receivers utilized in this study

Type GPS receivers	Signal Tracking	Indicated Accuracies		
		Static	Real Time Kinematic	DGPS
TOPCON GR3	GPS, GLONASS, Galileo	Horizontal: 3mm + 0.5 ppm	Horizontal: 10 mm + 1 ppm	< 50 cm
	(72 channel)	Vertical: 5mm + 0.5 ppm	Vertical: 15 mm + 1 ppm	
TOPCON GRS-1	GPS, GLONASS	Horizontal : 3mm + 0.8 ppm	Horizontal: 10 mm + 1 ppm	50 cm
	(72 Channel)	Vertical: 4mm + 1.0 ppm	Vertical: 15 mm + 1 ppm	
Septentrio AsteRx1 PRO	GPS, Galileo		Horizontal: 20 cm + 1 ppm	Horizontal: 50 cm
	(24 channel)		Vertical: 35 cm + 1 ppm	Vertical: 90 cm

GPS survey was conducted in the field to collect Ground Control Points (GCPs) shown in Figure 16 to be used in four purposes. The first was to georeference point cloud data acquired by Terrestrial Laser Scanner. The second was to use in orthorectification of aerial photos and Worldview-1 satellite imagery. The third was to assess the accuracy of DEMs created by aerial photos and TLS data. And the last was to use for mapping purposes. Number and usage of GCPs according to GPS receiver and date of the field work are given in Table 6.

Table 6 Number of GCPs collected in the field works.

	Date of GPS survey and GPS receiver used			
	04.07.2009	11.10.2009	15.04.2010	
Usage of GCPs	(Septentrio AsteRx1)	(Topcon GRS-1)	(Topcon GR3)	Total
Georeferencing of TLS data	–	47	84	131
Orthorectification of Aerial Photos	–	–	6	6
Orthorecticication of Worldview-1	–	–	6	6
Accuracy assesment of Current DEM	–	–	70	70
Accuracy assesment of Past DEM	–	82	41	123
Mapping	51	–	–	51

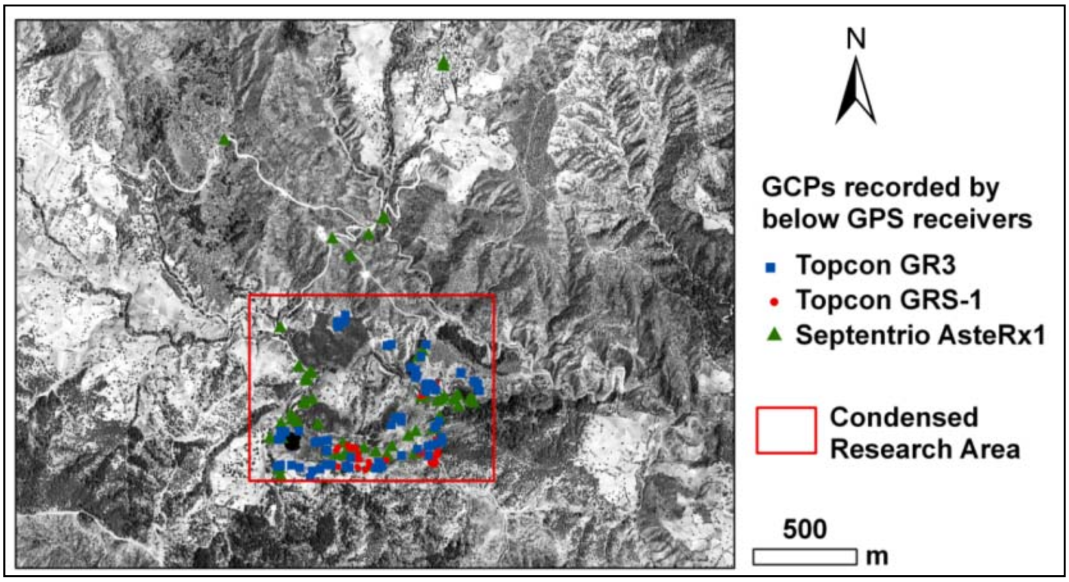

Figure 16 The location of GCPs recorded by GPS receivers

Ancillary Data

Forest map was obtained from General Directorate of Forestry (Orman Genel Müdürlüğü- OGM) with a scale of 1:25000 showing tree type, forest canopy density and general land use of the research area. The map was used in Land Use and Land Cover (LULC) mapping as a complementary data source.

Two 1:25000 scale topographical base maps of the region last updated in 1992 were obtained from General Command of Mapping (HGK) in digital raster data format and additional vector data of elevation contours. The maps were used to extract Digital Elevation Model (DEM) and as ancillary data while testing classification results. The most detailed available geological map of the region having a scale of 1:25000 was purchased from General Directorate of Mineral Research and Exploration (MTA) in vector data format as .e00.

3.5 Management of Data in GIS

Collected data was stored and processed in ArcGIS 9.3 software environment. At the beginning, the database was containing items shown in Figure 17. All available satellite imagery, aerial photos, topographical and geological maps, field data, settlement, road network, abandoned mine layout, Ground Control Points (GCPs) and Terrestrial Laser Scanning (TLS) data were included in the database. Images having different extents and geographic coordinate system were clipped regarding the extent of Worldview-1 imagery which determines the study area boundary and they were re-projected to UTM zone 36N coordinate system with WGS1984 datum. Besides data layers above, many layers produced from source data sets were included in the geodatabase. These were color composites for ASTER and Landsat images, classification of these images, Land Use and Land Cover (LULC) maps, LULC change maps, Digital Elevation Models (DEM) and various thematic maps like DEM difference, slope, and drainage network. Topographical data was stored in the form of Triangular Irregular Networks (TIN) and Terrain dataset. Point cloud (around 5 million points) derived from TLS was stored and processed in terrain data format due to its ability for retrieving only necessary data to build a surface of the required level of detail for a specified area of interest from huge terrain dataset.

All raster and vector data collected or created were converted and stored in a file geodatabase in ArcGIS software environment to make data management easier excluding TIN data which are not supported for file geodatabase format. To store topographical data in file geodatabase, TINs were converted to raster data format.

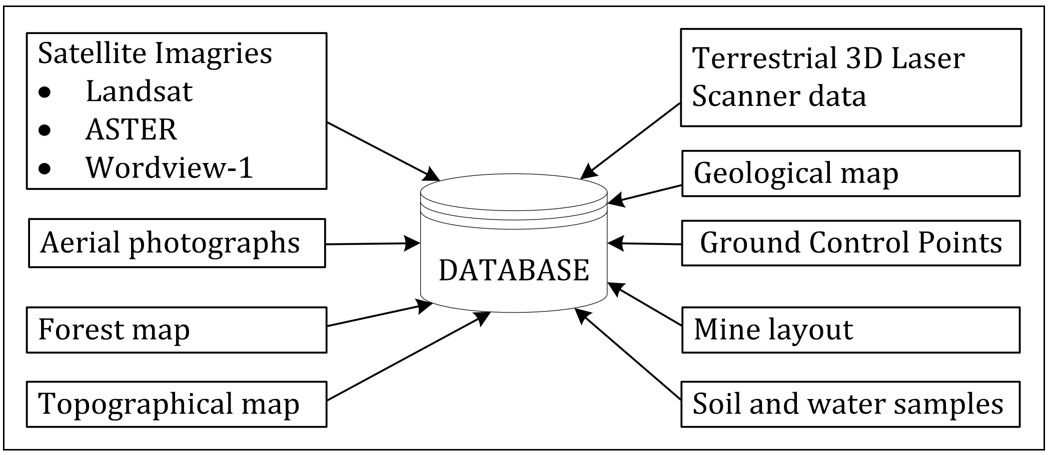

Figure 17 GIS database for Ovacık coal mine

3.6 Data Processing

Data processing steps refers to all pre-processing steps to generate dataset used in land degradation analysis. Main data processes are generation of Digital Elevation Models (DEM) for pre- and post-mining stages of the research area, orthorectification of historical aerial photos and Worldview-1 satellite imagery and pre-processes for ASTER and Landsat imagery.

3.6.1 Digital Elevation Model (DEM) Generation for Pre-mining Terrain from Stereo Pair of Aerial Photos

A digital elevation model (DEM) is a raster image storing elevation values of a surface terrain in each pixel. Stereo pair of aerial photos containing rational polynomial coefficients (RPCs) was used to generate DEM for the year 1951 in which there was no mining activity in the study area.

Computation of Rational Polynomial Coefficients (RPC) for Aerial Photos

In order to generate DEM from scanned stereo aerial photos taken by a frame camera or orthorectify them, first Rational Polynomial Coefficients (RPC)s were needed to be calculated representing sensor geometry in which object point, perspective center, and image point are all on the same space line using collinearity equation technique. The technique consists of transformations involving pixel, camera, image space, and coordinate systems.

ENVI 4.7 *Build RPCs* tool was used to compute and add RPCs to the header files of stereo aerial photo pair taken in 1951. To compute RPCs, interior and exterior orientation parameters should be calculated. Interior orientation (sensor geometry) parameters transform the pixel coordinate system to the camera coordinate system. On the other hand, exterior orientation parameters determine the position and angular orientation associated with the image (ENVI 4.7 Help Menu). Principal point offsets, focal length and positions of the fiducial marks are required to compute interior orientation parameters. However, GCPs are needed to compute the exterior orientation parameters which have six transformation parameters projection center coordinates (X, Y, and Z) and three rotations angles (omega, phi and kappa) shown in Figure 18 (Jacobsen, 2001).

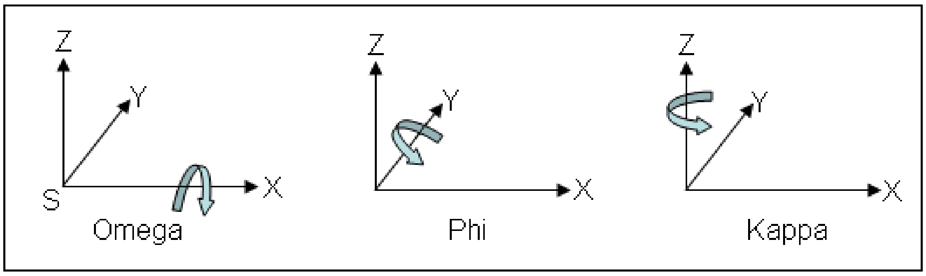

Figure 18 Graphical representation of rotation angles (ENVI 4.7 Help Menu)

The camera used for the first flight was Carl Zeiss RMK 10/18. The associated calibration file was also obtained from General Command of Mapping (HGK). The calibration file includes data about any potential errors for that camera and the parameters displayed in Table 7 which are input into the photogrammetry software while image processing. ENVI 4.7 was used as photogrammetry software.

Table 7 Camera calibration parameters used in calculation of RPCs for air photo taken in1951

Calibration Parameters	Value (mm)		
Focal Length		99.66	
	#	X	Y
Principal Point Coordinates		0.015	0.005
Fiducial Points Coordinates	1	0	87.985
	2	87.995	0
	3	0	-87.985
	4	-87.995	0
(y is in the flight direction)			

Fiducial marks were selected from the images and corresponding fiducial coordinates given in Table 7 were introduced into the software to compute interior orientation of the aerial photos. Associated image coordinates and error values of fiducial points are given in Table 8 and Table 9 for the air photos 354-222 and 354-223 respectively. As seen in Table 8 and Table 9, RMS errors of fiducial points were found acceptable (below 1 pixel) as 0.72 and 0.52 pixels respectively for the air photos 354-222 and 354-223.

Table 8 Error calculation in fiducial point selection of the aerial photo 354-222

Fiducial Points			Coordinates in pixels						
	Fiducial (mm)		Image		Predicted		Error		RMS Error
#	x	y	x	y	x	y	x	y	
1	0.00	87.98	8475.03	4396.00	8474.51	4396.51	-0.52	0.51	0.72
2	88.00	0.00	4395.97	8471.00	4396.48	8470.49	0.51	-0.51	0.72
3	0.00	-87.98	320.00	4397.96	319.48	4398.47	-0.52	0.51	0.72
4	-88.00	0.00	4397.00	325.00	4397.52	324.49	0.52	-0.51	0.72
							Total RMS Error		0.72

Table 9 Error calculation in fiducial point selection of the aerial photo 354-223

Fiducial Points			Coordinates in pixels						
	Fiducial (mm)		Image		Predicted		Error		RMS Error
#	x	y	x	y	x	y	x	y	
1	0.00	87.98	8529.00	4525.00	8528.77	4525.50	-0.23	0.50	0.55
2	88.00	0.00	4397.00	8549.00	4397.23	8548.50	0.23	-0.50	0.55
3	0.00	-87.98	370.97	4421.97	370.74	4422.47	-0.23	0.50	0.55
4	-88.00	0.00	4502.04	399.96	4502.27	399.46	0.23	-0.50	0.55
							Total RMS Error		0.55

During computation of exterior orientation parameters, among discernable GCPs from the aerial photos, 6 GCPs recorded by Topcon GR3 GPS receiver which were well spread across the images were selected displayed in Figure 19 . The same 6

GCPs were used for both images. Image coordinates and error values of these GCPs are given in Table 10 and Table 11 respectively for the images 354-222 and 354-223. Final RMS errors were 18.48 and 12.90 pixels for the images 354-222 and 354-223.

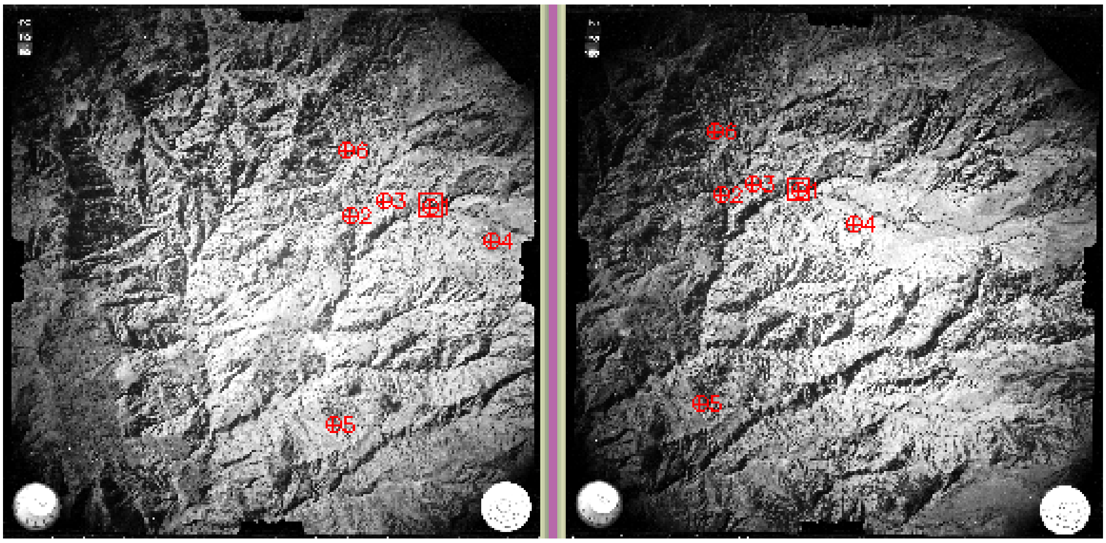

Figure 19 Location of GCPs on stereo aerial photos 354-222 (left) and 354-223 (right)

Calculated exterior orientation parameters are given in Table 12 and they were used to calculate RPCs. RPCs were calculated using interior and exterior orientation parameters for each image and added to corresponding header files shown in Figure 20 for the image 354-222. After computation of RPCs, it was possible to determine ground resolution of scanned aerial photos. Therefore, pixel sizes have been found as 0.73x 0.73 m.

Table 10 Error calculation in GCP selection of the aerial photo 354-222

GCPs				Coordinates in pixels						
	Map (m)			Image		Predicted		Error		RMS Error
#	x	y	z	x	y	x	y	x	y	
1	590669.62	4514250.11	1254.70	6997.29	3341.86	7025.16	3350.61	27.87	8.75	29.21
2	590939.44	4513258.09	1233.38	5681.57	3458.43	5658.41	3447.44	-23.16	-10.99	25.63
3	590707.94	4513630.15	1262.10	6222.14	3244.57	6211.50	3245.24	-10.64	0.67	10.66
4	590959.54	4514999.29	1331.70	8000.50	3881.50	7987.51	3876.52	-12.99	-4.98	13.91
5	593650.89	4513568.91	1241.20	5396.50	6909.50	5402.21	6911.70	5.71	2.20	6.12
6	590170.30	4513042.96	1293.65	5608.50	2409.50	5621.71	2413.85	13.21	4.35	13.91
								Total RMS Error		18.48

Table 11 Error calculation in GCP selection of the aerial photo 354-223

GCPs				Coordinates in pixels						
	Map (m)			Image		Predicted		Error		RMS Error
#	x	y	z	x	y	x	y	x	y	
1	590669.62	4514250.11	1254.70	3853.50	3085.75	3873.88	3090.43	20.38	4.68	20.91
2	590939.44	4513258.09	1233.38	2564.00	3167.00	2549.02	3160.98	-14.98	-6.02	16.15
3	590707.94	4513630.15	1262.10	3089.75	2968.00	3079.86	2968.51	-9.89	0.51	9.90
4	590959.54	4514999.29	1331.70	4753.50	3627.75	4744.47	3625.05	-9.03	-2.70	9.42
5	593650.89	4513568.91	1241.20	2228.75	6609.25	2232.71	6610.44	3.96	1.19	4.14
6	590170.30	4513042.96	1293.65	2467.75	2118.25	2477.31	2120.59	9.56	2.34	9.84
								Total RMS Error		12.90

Table 12 Exterior orientation parameters for the stereo aerial photo pair taken in 1951

Exterior oriantation parameters		
	Aerial Photos	
	354-222	354-223
x (m)	591849.95	591579.24
y (m)	4512552.70	4515026.77
z (m)	4905.38	4818.47
Omega (degree)	-2.146	-1.740
Phi (degree)	-0.187	-0.734
Kappa (degree)	10.425	10.840

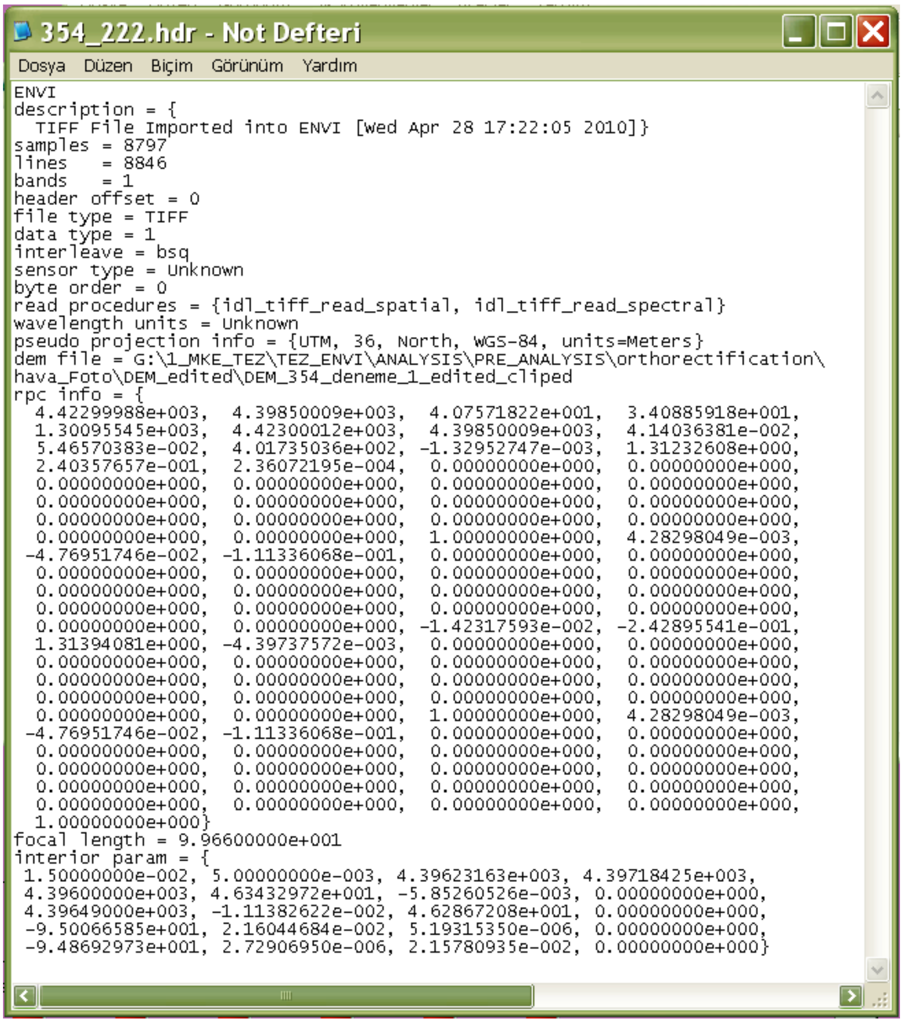

354_222.hdr - Not Defteri

Dosya Düzen Biçim Görünüm Yardım

```
ENVI
description = {
  TIFF File Imported into ENVI [Wed Apr 28 17:22:05 2010]}
samples = 8797
lines   = 8846
bands   = 1
header offset = 0
file type = TIFF
data type = 1
interleave = bsq
sensor type = Unknown
byte order = 0
read procedures = {idl_tiff_read_spatial, idl_tiff_read_spectral}
wavelength units = Unknown
pseudo projection info = {UTM, 36, North, WGS-84, units=Meters}
dem file = G:\1_MKE_TEZ\TEZ_ENVI\ANALYSIS\PRE_ANALYSIS\orthorectification\
hava_Foto\DEM_edited\DEM_354_deneme_1_edited_cliped
rpc info = {
  4.42299988e+003,  4.39850009e+003,  4.07571822e+001,  3.40885918e+001,
  1.30095545e+003,  4.42300012e+003,  4.39850009e+003,  4.14036381e-002,
  5.46570383e-002,  4.01735036e+002, -1.32952747e-003,  1.31232608e+000,
  2.40357657e-001,  2.36072195e-004,  0.00000000e+000,  0.00000000e+000,
  0.00000000e+000,  0.00000000e+000,  0.00000000e+000,  0.00000000e+000,
  0.00000000e+000,  0.00000000e+000,  0.00000000e+000,  0.00000000e+000,
  0.00000000e+000,  0.00000000e+000,  0.00000000e+000,  0.00000000e+000,
  0.00000000e+000,  0.00000000e+000,  1.00000000e+000,  4.28298049e-003,
 -4.76951746e-002, -1.11336068e-001,  0.00000000e+000,  0.00000000e+000,
  0.00000000e+000,  0.00000000e+000,  0.00000000e+000,  0.00000000e+000,
  0.00000000e+000,  0.00000000e+000,  0.00000000e+000,  0.00000000e+000,
  0.00000000e+000,  0.00000000e+000,  0.00000000e+000,  0.00000000e+000,
  0.00000000e+000,  0.00000000e+000, -1.42317593e-002, -2.42895541e-001,
  1.31394081e+000, -4.39737572e-003,  0.00000000e+000,  0.00000000e+000,
  0.00000000e+000,  0.00000000e+000,  0.00000000e+000,  0.00000000e+000,
  0.00000000e+000,  0.00000000e+000,  0.00000000e+000,  0.00000000e+000,
  0.00000000e+000,  0.00000000e+000,  0.00000000e+000,  0.00000000e+000,
  0.00000000e+000,  0.00000000e+000,  1.00000000e+000,  4.28298049e-003,
 -4.76951746e-002, -1.11336068e-001,  0.00000000e+000,  0.00000000e+000,
  0.00000000e+000,  0.00000000e+000,  0.00000000e+000,  0.00000000e+000,
  0.00000000e+000,  0.00000000e+000,  0.00000000e+000,  0.00000000e+000,
  0.00000000e+000,  0.00000000e+000,  0.00000000e+000,  0.00000000e+000,
  0.00000000e+000,  0.00000000e+000,  0.00000000e+000,  0.00000000e+000,
  1.00000000e+000}
focal length = 9.96600000e+001
interior param = {
 1.50000000e-002, 5.00000000e-003, 4.39623163e+003, 4.39718425e+003,
 4.39600000e+003, 4.63432972e+001, -5.85260526e-003, 0.00000000e+000,
 4.39649000e+003, -1.11382622e-002, 4.62867208e+001, 0.00000000e+000,
 -9.50066585e+001, 2.16044684e-002, 5.19315350e-006, 0.00000000e+000,
 -9.48692973e+001, 2.72906950e-006, 2.15780935e-002, 0.00000000e+000}
```

Figure 20 Header file of aerial photo 354-222 showing calculated RPCs

Digital Elevation Model (DEM) Generation

A digital elevation model (DEM) was generated using stereo pair of aerial photos having rational polynomial coefficients (RPCs) for the year 1951 in which there was no mining activity in the study area. In DEM extraction process from aerial photography, *DEM Extraction Module* of ENVI 4.7 was used. There are three main steps of DEM extraction procedure: epipolar image generation, image matching, and DEM geocoding. Implemented DEM extraction tool has processing steps given in
Figure 21.

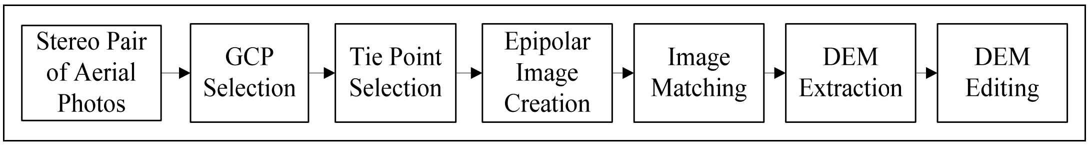

Figure 21 Processing steps of DEM generation from stereo aerial photos

Epipolar image generation needs tie points to define the relationship between the pixels in the stereo pair. An Epipolar image is a stereo pair in which the left and right images are oriented in such a way that ground feature points have the same y-coordinates on both images. Epipolar images are also used in 3D visualization using anaglyph glasses (ENVI 4.7 Help Menu).

In order to get absolute DEM which is comparable with the DEM created from point cloud measured by Terrestrial Laser Scanner (TLS), it was needed to use Ground Control Points (GCPs) collected in the field while DEM generation from stereo pair. Using GCPs ties horizontal and vertical reference systems to geodetic coordinates and the resultant DEM is called as absolute DEM. 6 GCPs previously used in calculation of RPCs are used also in DEM extraction procedure. As seen in Figure 22, GCPs were marked in both left (354-222) and right (354-223) images and corresponding ground coordinates were introduced to match with associated image coordinates of GCPs.

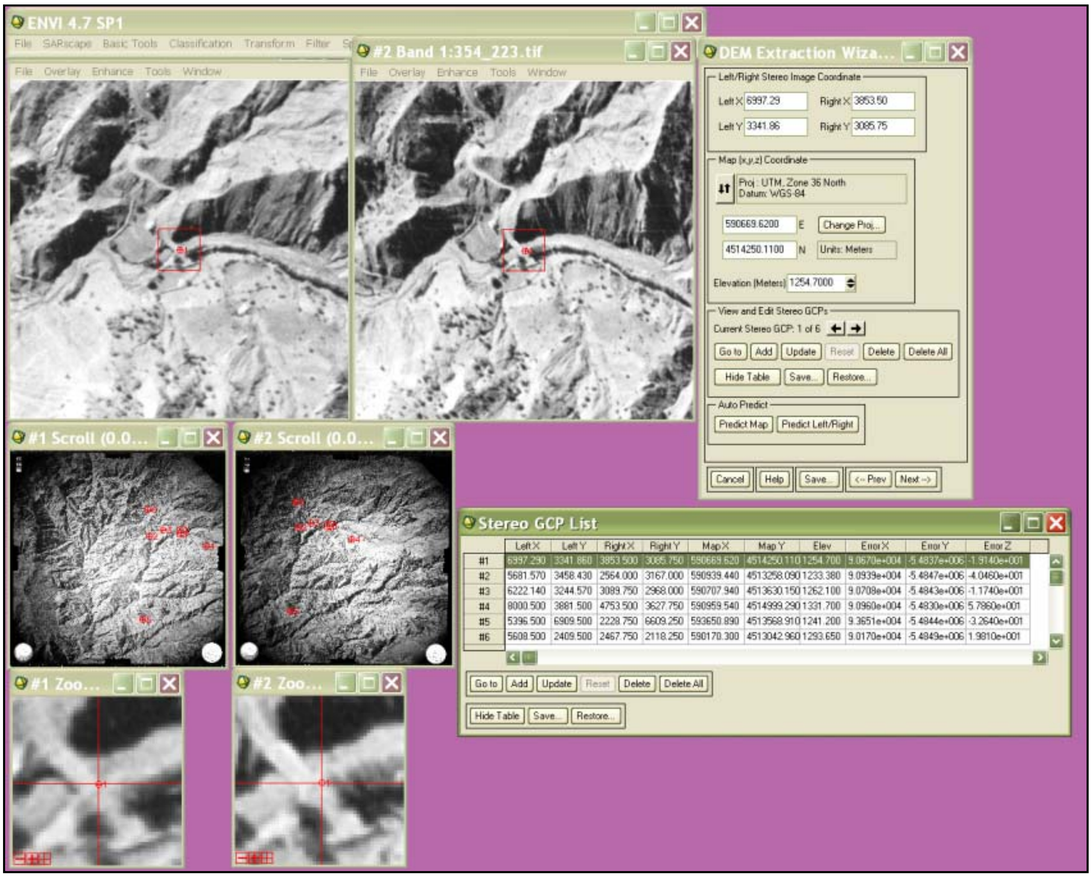

Figure 22 ENVI 4.7 software snapshot during GCP selection step

Tie point selection was performed iteratively considering two main objectives: spreading tie points well across the images and reducing maximum Y parallax below 10 pixels which was threshold value for the software. Y parallax is defined as the difference in perpendicular distances between two images of a point from the vertical plane which contains the air base. Due to the fact that, increasing number of tie points also increased the maximum Y parallax and make impossible to go further in DEM extraction procedure, number of tie points were kept as 9 which was also the minimum number of tie points needed by the software. After reaching 9 tie points supplying a maximum Y parallax of 0.3747 and spreading well across stereo pair, tie point selection have been finalized. Locations of these tie points are displayed in Figure 23. Image coordinates of these stereo tie points are given in Table 13

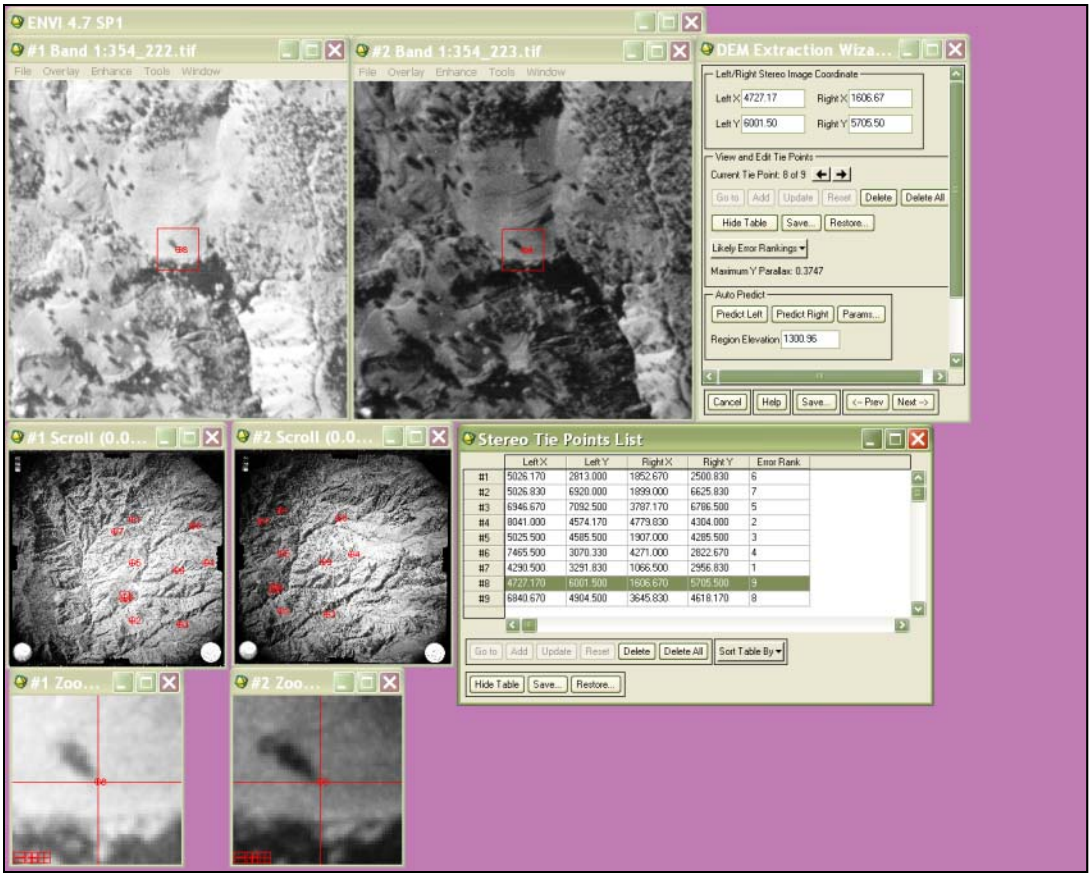

Figure 23 ENVI 4.7 software snapshot while tie point selection step

Table 13 Stereo tie points image coordinates for image pair taken in 1951

Image coordinates of tie points				
	Left image (354-222)		Right image (354-223)	
#	x	y	x	y
1	5026.2	2813.0	1852.7	2500.8
2	5026.8	6920.0	1899.0	6625.8
3	6946.7	7092.5	3787.2	6786.5
4	8041.0	4574.2	4779.8	4304.0
5	5025.5	4585.5	1907.0	4285.5
6	7465.5	3070.3	4271.0	2822.7
7	4290.5	3291.8	1066.5	2956.8
8	4727.2	6001.5	1606.7	5705.5
9	6840.7	4904.5	3645.8	4618.2

Using tie points, epipaolar images were produced. After loading left epipolar image to Green and Blue channel and Right epipolar image to Red channel of RGB display, as seen in the Figure 24, it was possible to see terrain in 3D and to perform 3D measurements of selected points in research area by anaglyph glasses.

Image matching is the process behind the DEM generation from stereo pair of images. The image matching algorithm finds the conjugate points on stereo images which belong to the same ground feature and produce a parallax image in which x-coordinate differences are used to calculate elevation values. Using epipolar images in image matching removes one dimension of variability, hence improves the process of image matching in terms of speed and the reliability of the results (ENVI 4.7 Help Menu).

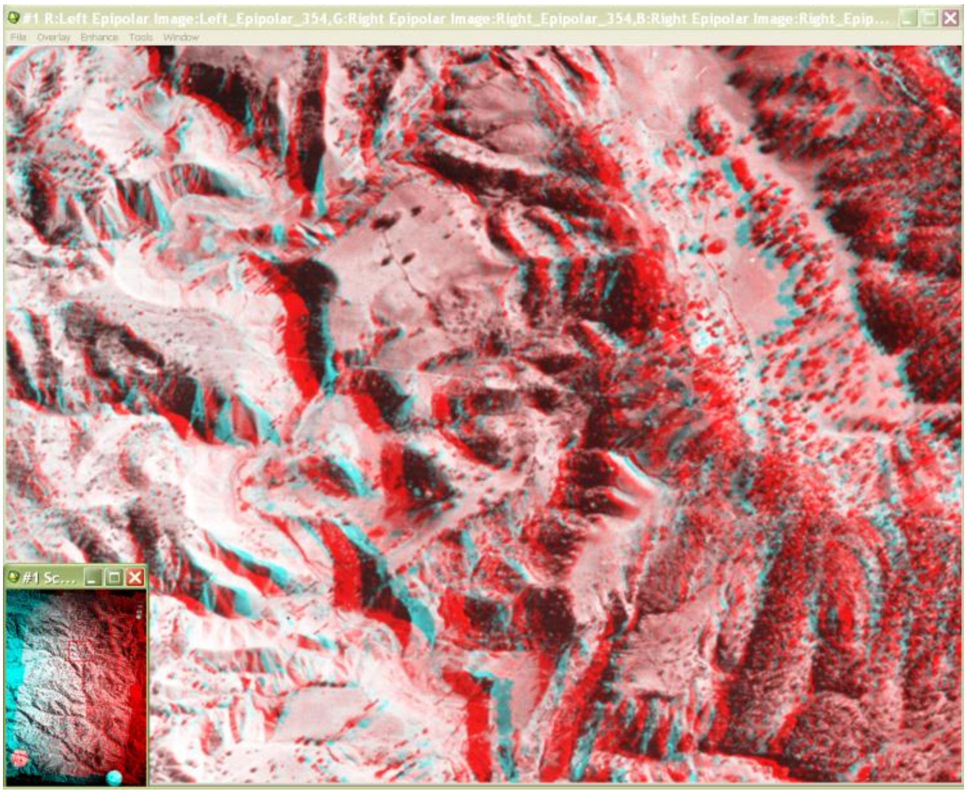

Figure 24 Epipolar stereo pair of images (anaglyph image) of research area before mining operation has been started (should be seen by anaglyph glasses for 3D viewing)

DEM was created with pixel sizes of 0.5x0.5 m using epipolar images obtained from stereo Aerial photo pair taken in 1951. As seen in Figure 25, artifacts were formed in the DEM near the edges due to damages in the film of the scanned photo itself. Hence, an effective area of DEM, displayed in Figure 25, was clipped considering both these artifacts and the coverage of research area. To remove peaks in DEM caused by trees and manmade structures, median and smooth (low-pass convolution) filters of *DEM Editing Tool* of the software were investigated with kernel sizes of 5x5, 11x11 and 21x21. After visual interpretation of hill shade views of these filtering results of DEM shown in Figure 26, it is observed that the median filters resulted in stepped DEMs. Therefore, it was concluded to use the DEM edited by smooth filter with the kernel size of 21x21 in remaining part of this study which gives the best result considering removal of peaks due to trees and manmade structures.

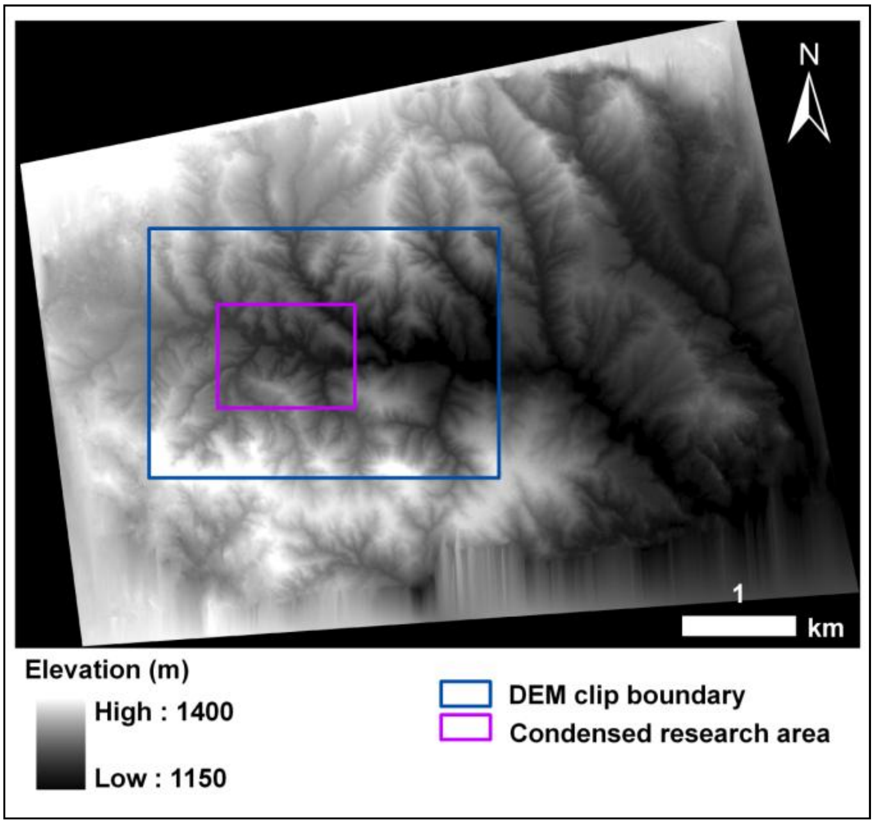

Figure 25 Full scene DEM showing artifacts near the edges of the DEM and showing selected DEM boundary

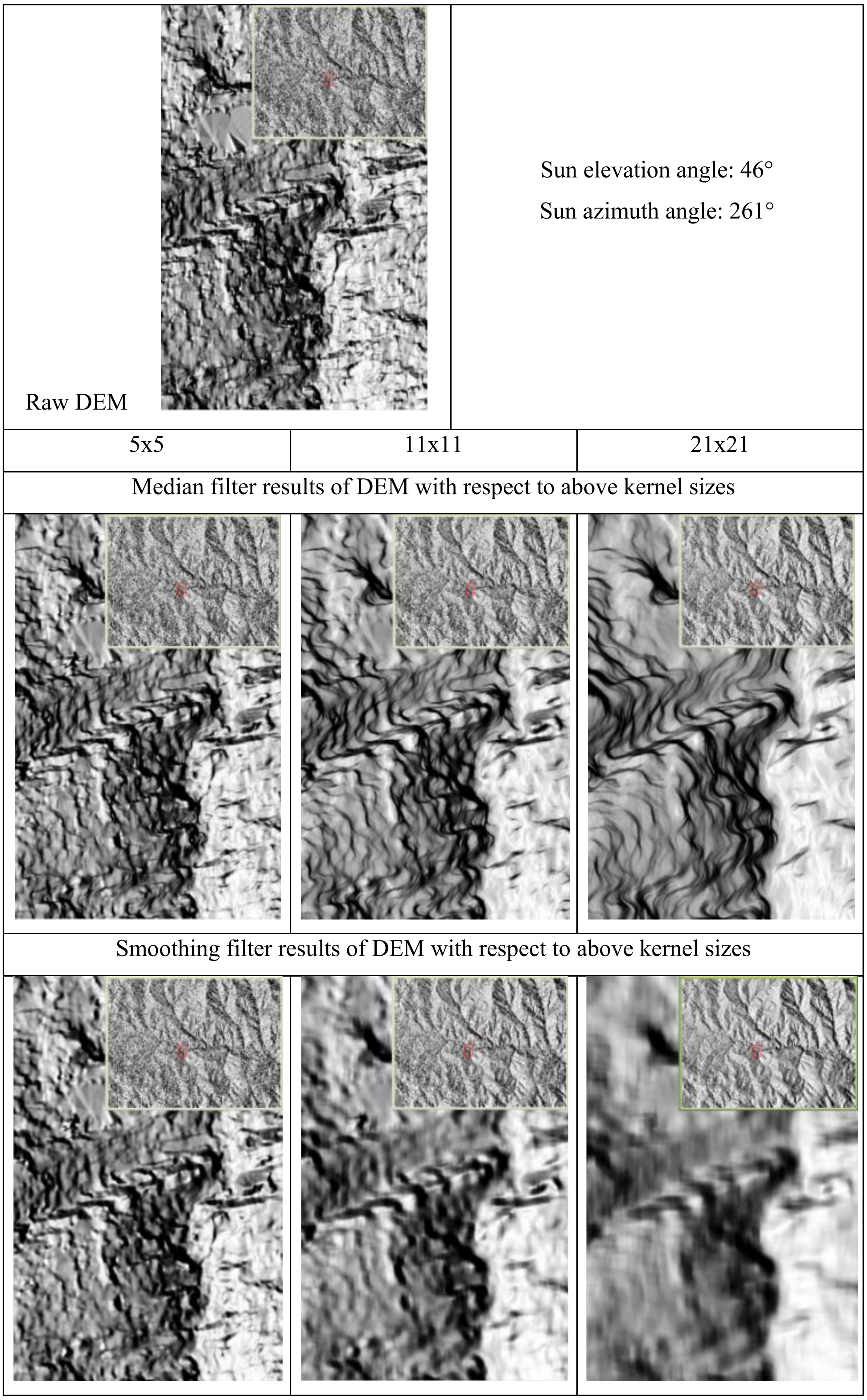

Figure 26 Hill shade views of DEMs in the area of 200 by 300 m after median and smoothing filters applied with kernel sizes of 5x5, 11x11, and 21x21 pixels

Accuracy Assessment of Pre-mining Digital Elevation Model (DEM)

Accuracy assessment of DEM dated 1951 created by stereo pair of aerial photos representing pre-mining terrain were conducted by using 123 Ground Control Points (GCPs) shown in Figure 27. Because there were 58 years between data acquisition date of DEM and GPS survey, GCPs were carefully chosen from locations where no apparent topographical changes exist. Thus, only 41 of GCPs among the points recorded by Topcon GR3 could be used and others where land degradation exists were eliminated from data in the accuracy assessment of past DEM. Instead of these eliminated points, 82 points recorded by Topcon GRS-1 were selected where there is no topographical change observed and added to the accuracy assessment. This test data was superimposed with the DEM and based on differences between Z-coordinates of these GCPs and DEM, RMS errors were calculated. The RMS errors calculated by using only Topcon GR3 and Topcon GRS-1 datasets were 4.01m and 2.24 m respectively. Overall RMS error was 2.95 m. Individual errors of GCPs used in the accuracy assessment of the DEM generated by aerial photos were given in Table A1.

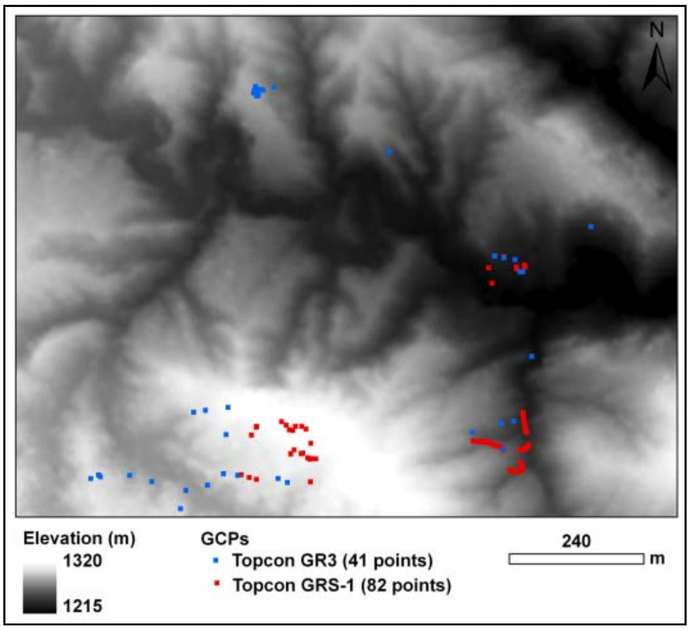

Figure 27 Locations of GCPs used for vertical accuracy assessment of DEM dated 1951

3.6.2 Orthorectification of Aerial Photos

Orthorectification is a process of using a DEM to correct image displacements caused by camera tilt or terrain relief during the acquisition of aerial photos or satellite images. Orthorectification result of an aerial photo is called as orthophoto from which maps can be drawn and distances can be measured.

Orthorectification tool of ENVI 4.7 software was used in the mode of *RPC Orthorectification* for the aerial photos. DEM created by stereo pair of images and GCPs were also used to enhance the accuracy of the orthorectification.

During orthorectification nearest neighbour, bilinear and cubic convolution interpolation methods were experimented. As seen in Figure 28, nearest neighbour method gave disjointed appearance. Also, bilinear interpolation resulted in blurring. Cubic convolution interpolation result was found to be optimal due to being sharper than bilinear and less disjointed than nearest neighbour methods. During the procedure pixel sizes were resampled to 0.5x0.5 m the same as the Worldview-1 imagery. Resultant orthophoto created from aerial photo 354-222 is displayed in Figure 29.

Nearest Neighbour	Bilinear Interpolation	Cubic Convolution
		

Figure 28 Results of interpolation methods used during orthorectification of aerial photos displayed in an area of 200x200 m with a 10x10 m zoom screen

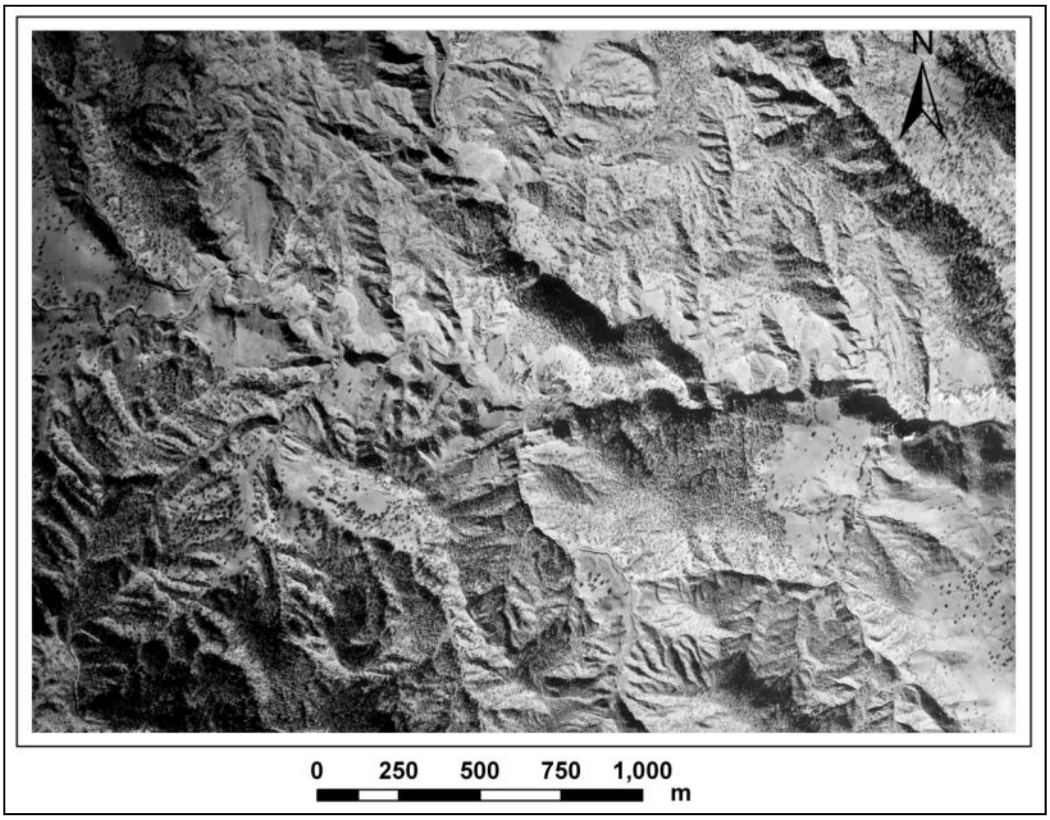

Figure 29 Orthorectified aerial photo (354-222) taken in 1951

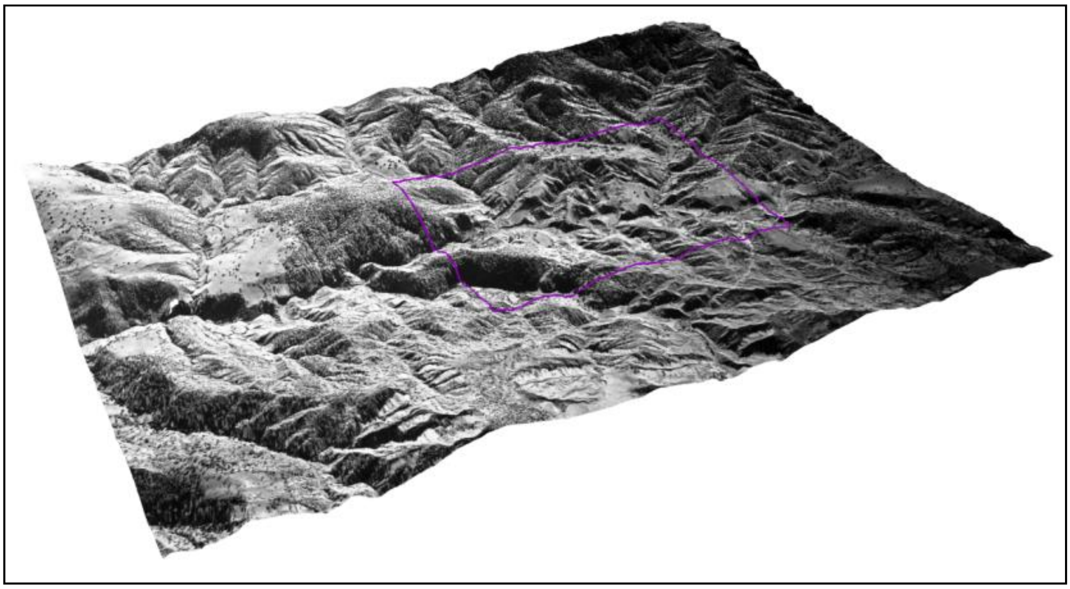

Figure 30 Perspective view of orthophoto dated 1951 draped on DEM highlighting condensed research area

3.6.3 Digital Elevation Model (DEM) Generation for Post-Mining Terrain from Terrestrial Laser Scanner (TLS) Point Cloud

In order to extract detailed Digital Elevation Model (DEM) of the current terrain, Terrestrial Laser Scanner (TLS) survey was conducted. Once the scans were merged and georeferenced, noise and points representing trees and manmade structures like buildings and electricity transmission line were eliminated. To obtain a simplified 3D model which could be easily processed during triangulation a data reduction was applied. After the data reduction, number of points reduced from approximately 150 million to 5 million and average point spacing increased from 14 cm to 74 cm respectively. The point cloud density was also calculated in the unit of number of points per square meter (pts/m^2). As seen from the point cloud density map given in Figure 31, in the most of the region, point cloud density was in the range of 10-20 pts/m^2 which gave us enough topographical detail.

Resultant point cloud was imported to *ArcGIS 9.3* software environment to model surface of the post mining landscape. Because of having large point cloud, a terrain data set was created instead of a Triangulated Irregular Network (TIN) file displayed in Figure 32 and Figure 33 . Terrain dataset is a multi-resolution, TIN-based surface geodatabase designed for data recorded by lidar, sonar, and photogrammetry. Advantage of terrain dataset is to create TIN surface on the fly for the area of interest (display screen) based on the pyramid level previously defined for that display scale. This makes it possible to faster drawing of TIN surface and handling of higher point cloud capacity comparing to TIN data format.
Once terrain dataset was built with 5 pyramid levels, DEM was generated with 0.5x0.5 m pixel size same as the DEM created from stereo aerial photos. Resultant DEM covers around 1.06 km^2 of the research site in rectangular shape defined as condensed research area including the most important parts of the site which are open pit, dump sites, coal stock site, and mine facilities. Further topographical analysis mentioned in section 3.7.1 was performed for this condensed research area.

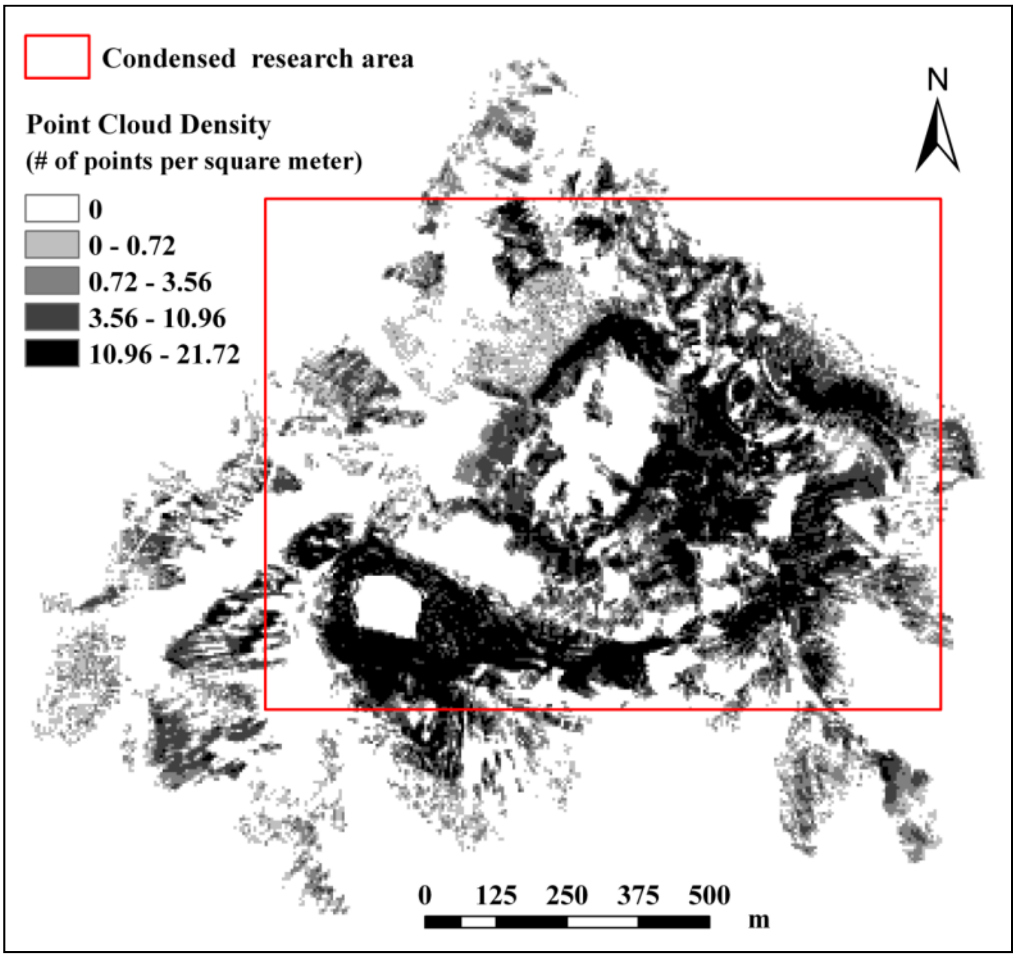

Figure 31 TLS point cloud density map classified to 5 classes with 5x5 m cell size

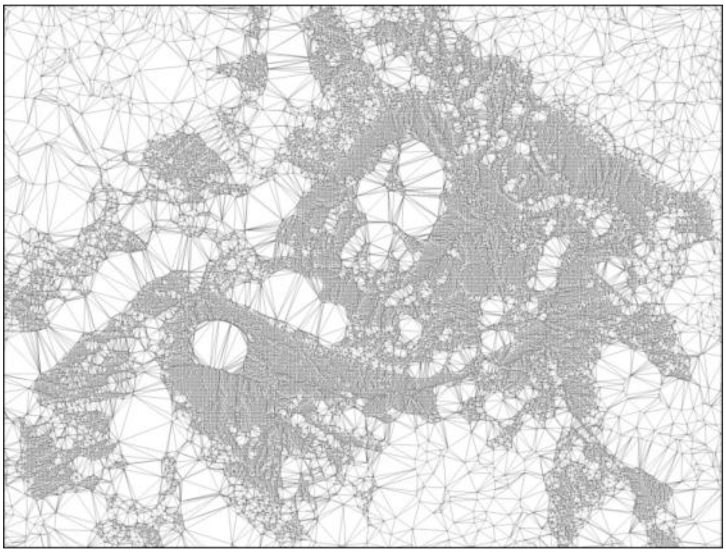

Figure 32 Mesh view of Terrain dataset created from point cloud

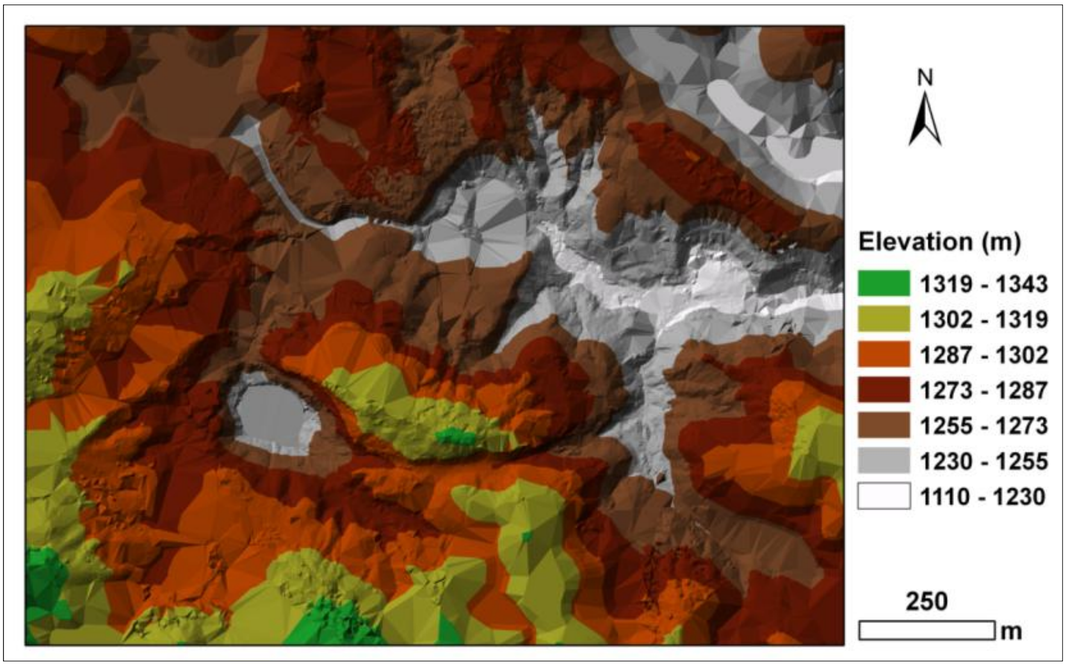

Figure 33 Terrain data set showing elevation

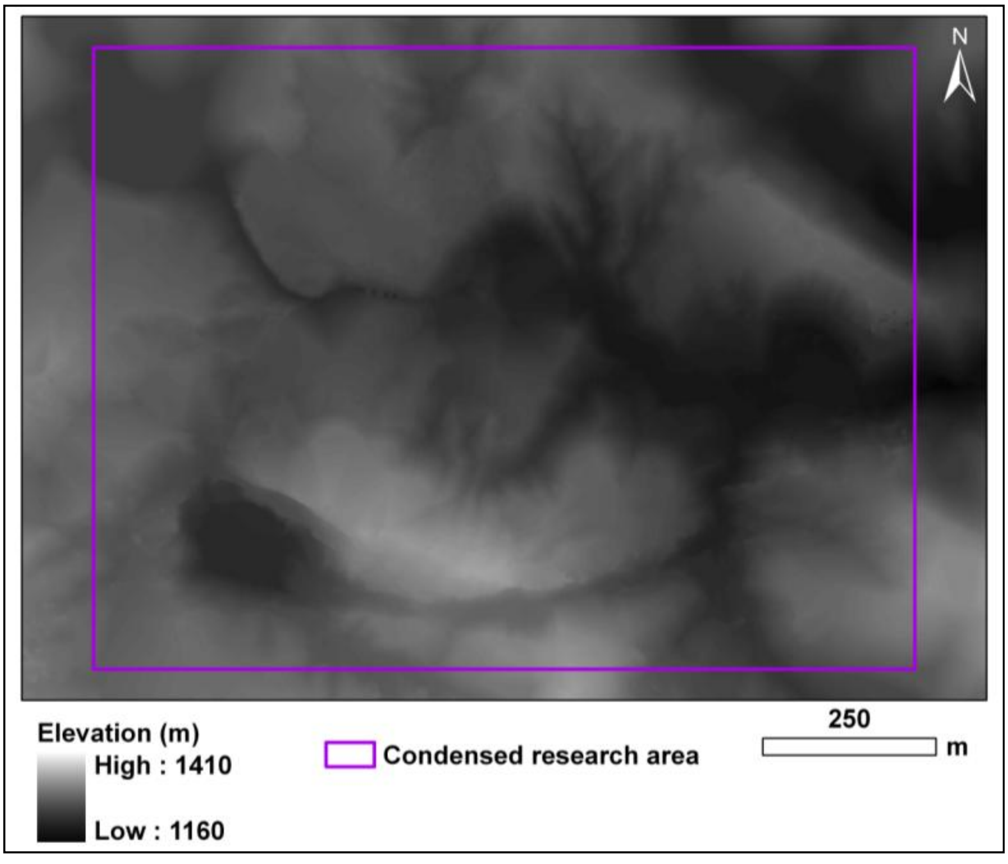

Figure 34 Current DEM produced from TLS point cloud

Accuracy Assessment of Pre-mining Digital Elevation Model (DEM)

Accuracy assessment of DEM representing current terrain (in 2009) produced from Terrestrial Laser Scanner (TLS) point cloud representing post-mining terrain was conducted using 70 GCPs shown in Figure 35 recorded by Topcon GR3 GPS device. 16 points were eliminated from data where the point cloud density was too low. After calculating differences between Z-coordinates of these check points and DEM, RMS errors were calculated. The overall RMS error was found to be 0.98 m using 70 GCPs recorded by Topcon GR3 GPS device. Individual errors of GCPs used in the accuracy assessment of the DEM generated by TLS were given in Table A2.

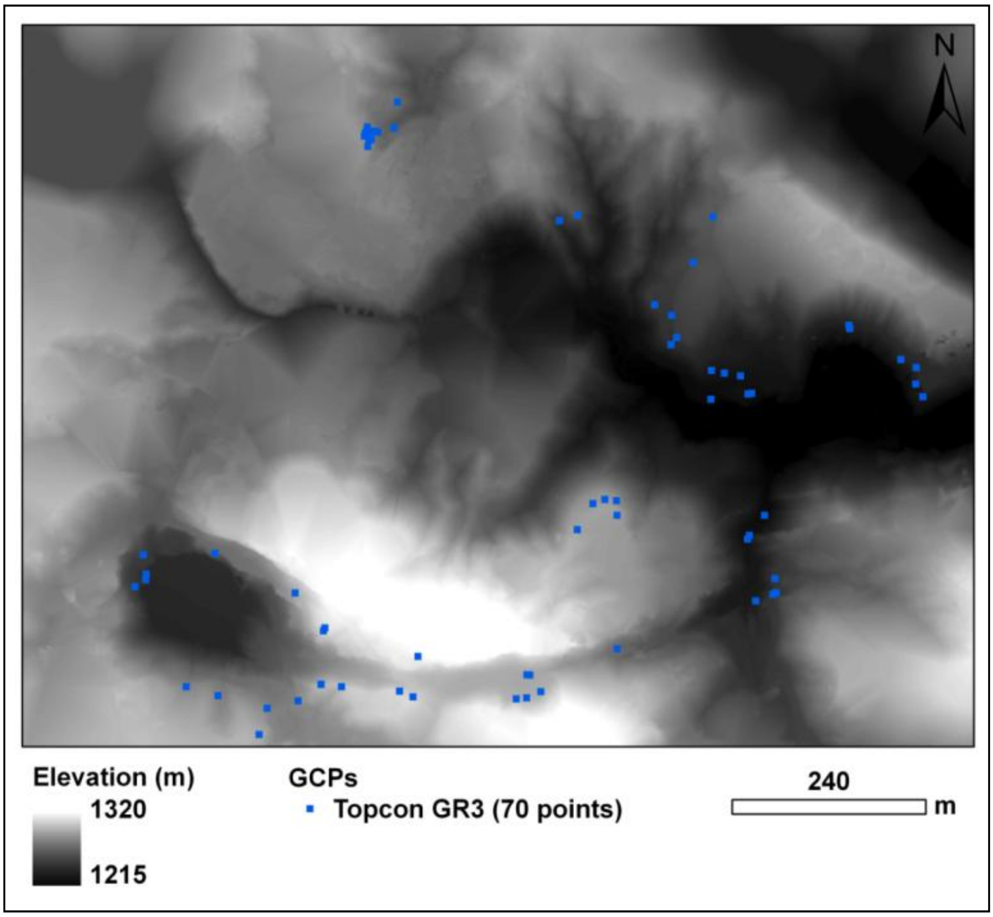

Figure 35 Locations of GCPs used for vertical accuracy assessment of DEM dated 2009

3.6.4 Orthorectification of Worldview-1 Satellite Imagery

ENVI 4.7 *rigorous orthorectification module* was used in orthorectification process for Worldview-1 imagery which was delivered with RPCs file. GCPs and DEM for the current terrain were also used to enhance the accuracy of the orthorectification. The GCPs used in the orthorectification of aerial photos were also used in the orthorectification of Worlview-1 imagery.

The extent of DEM produced from TLS was not enough to orthorectify the full scene Worldview-1 imagery which has 5x5 km extent. Thus, it was needed to expand the coverage of DEM by adding points shown in Figure 36 to the terrain dataset derived from topographical map obtained from General Command of Mapping (HGK) to orthorectify the full scene Worldview-1 satellite imagery. During orthorectification cubic convolution interpolation method was applied and pixel size was remained constant at 0.5x0.5 m.

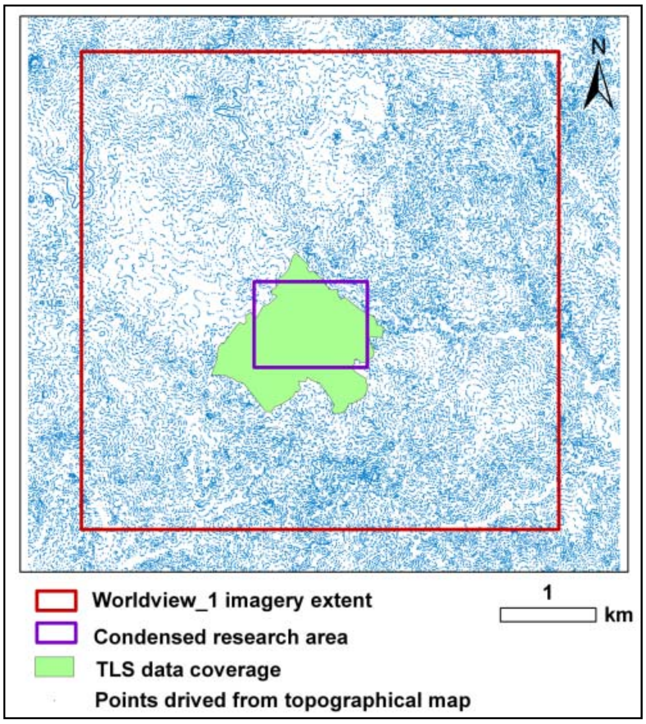

Figure 36 Elevation points derived from topographical map to expand DEM to be used in orthorectification of Worldview-1 satellite imagery

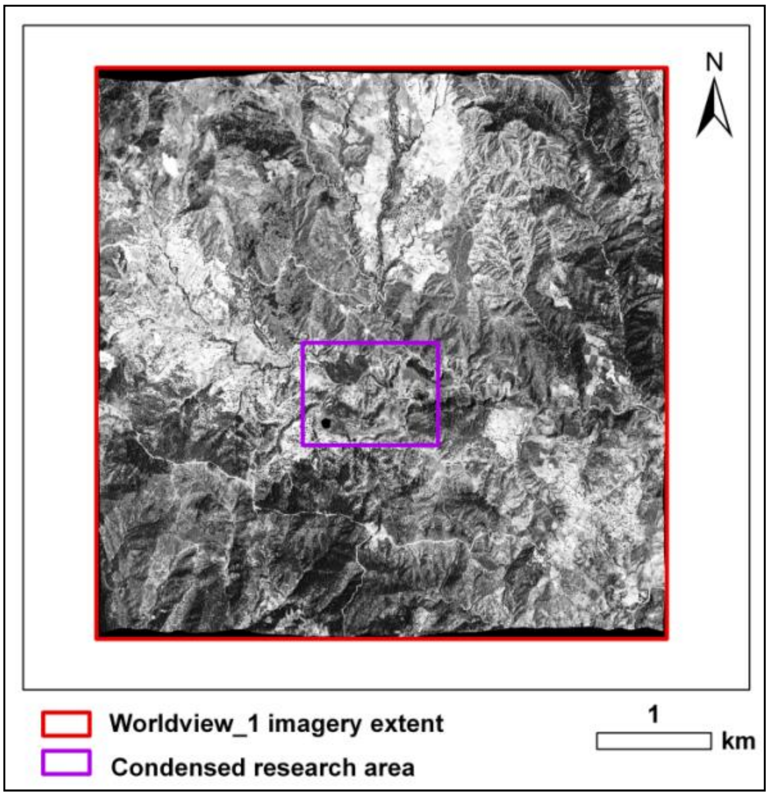

Figure 37 Orthorectified Worldview-1 imagery

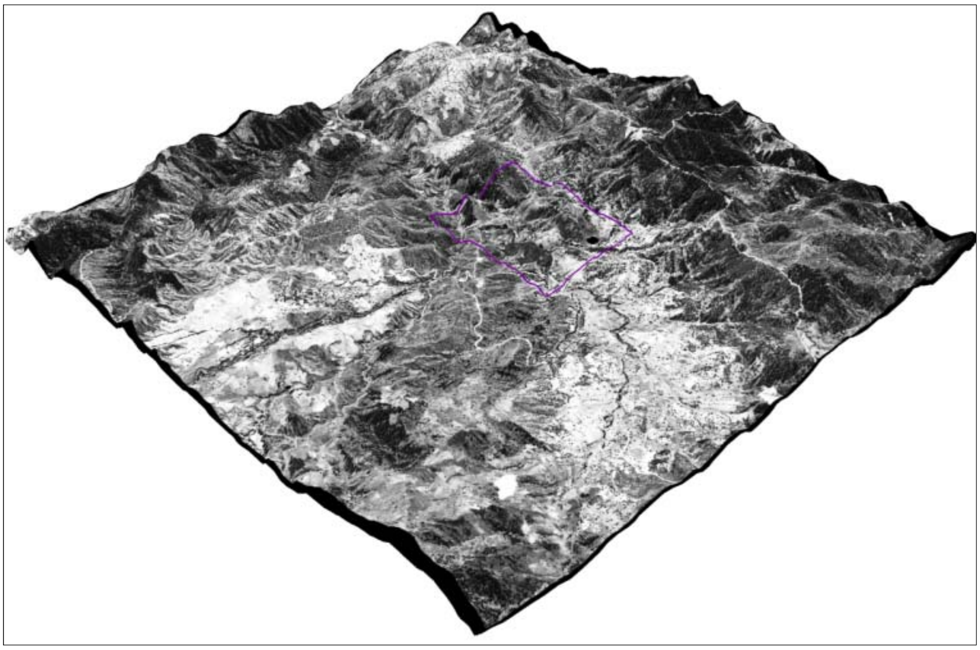

Figure 38 Perspective view of orthorectified Worldview-1 scene draped on DEM highlighting condensed research area

3.6.5 Preprocessing of Landsat and ASTER Satellite imagery

In order to make precise change detection analyses using multi-date imagery they should be orthorectified and co-registered. Both ASTER and Landsat imagery set was obtained as orthorectified. In order to focus on the research area Ovacık coal mine site, each satellite image was clipped with the same rectangular vector data to take subset. Therefore imagery sets become ready to image classification and change detection procedures.

3.7 Analysis of Land Degradation

Land degradation analysis involves two major parts. In the first part, topographical changes were analyzed. In the second part, Land Use and Land Cover (LULC) changes were investigated.

3.7.1 Topographical Change Analysis

After producing the multi-temporal raster DEMs, they were checked to ensure having equivalent geographic reference (UTM zone 36, Datum: WGS84), pixel size (0.5 m) and spatial extent which was previously determined based on effective DEM produced from aerial photos shown in Figure 25. In the topographical change analysis section, changes in volume, drainage network, and slope were investigated in ArcGIS 9.3 as Geographic Information System (GIS) environment.

Volumetric Change in Topography

It is important to determine excavated and dumped material volumes and its locations in the evaluation of land degradation induced by surface mining. Most of the abandoned mines lack of detailed terrain datasets in their archives. Historical stereo aerial photos are valuable data sources to extract DEM of the site before mine start to operate. In this study, a stereo photo set acquired via a frame camera in 1951 was used to generate DEM having 0.5x0.5 m pixel size. Post-mining DEM was produced by terrestrial laser scanner data and resampled to 0.5x0.5 m resolution while converting to raster. After preparation of DEM for pre- (1951) and post-mining (2009) stages of condensed research area, DEM differencing and thresholding were implemented as a method of terrain change detection. Initial threshold value was determined as 9.3 m by the formula given in Eq (1) based on individual absolute accuracy of each elevation data proposed by Jaw (2001).

$$\text{Threshold} = 3\,.\,\sqrt{(\text{RMSE}_{\text{data set t1}})^2 + (\text{RMSE}_{\text{data set t2}})^2} \qquad \text{Eq (1)}$$

After application of initial threshold value, several threshold values from 1 m to 20 m were applied and corresponding change maps were created as excavation, filling and no change classes. Final threshold value was determined based on comparison of overlap between change boundaries and current land use map. The change polygons of 11 m threshold for fillings and 3 m for excavations were best matched with current land use displayed in Figure 56. The polygons determined by thresholding laying on the areas having very low point density were eliminated from the change polygons. Resultant change polygons depicted also as topographically disturbed lands shown in Figure 39 and Figure 40 were used in calculation of volume change by summing up height difference within the polygon and multiplying with the raster cell area. Description, area, and volume of change polygons are given in Table 14.

Results of volumetric change analysis revealed that some of significant terrain changes not identified in the field surveys and interpretation of very high resolution satellite images could be found easily by DEM differencing. The polygon D3 and R, shown in Figure 40, were found after DEM comparison which could not be distinguished as dump site in the field surveys or image interpretation.

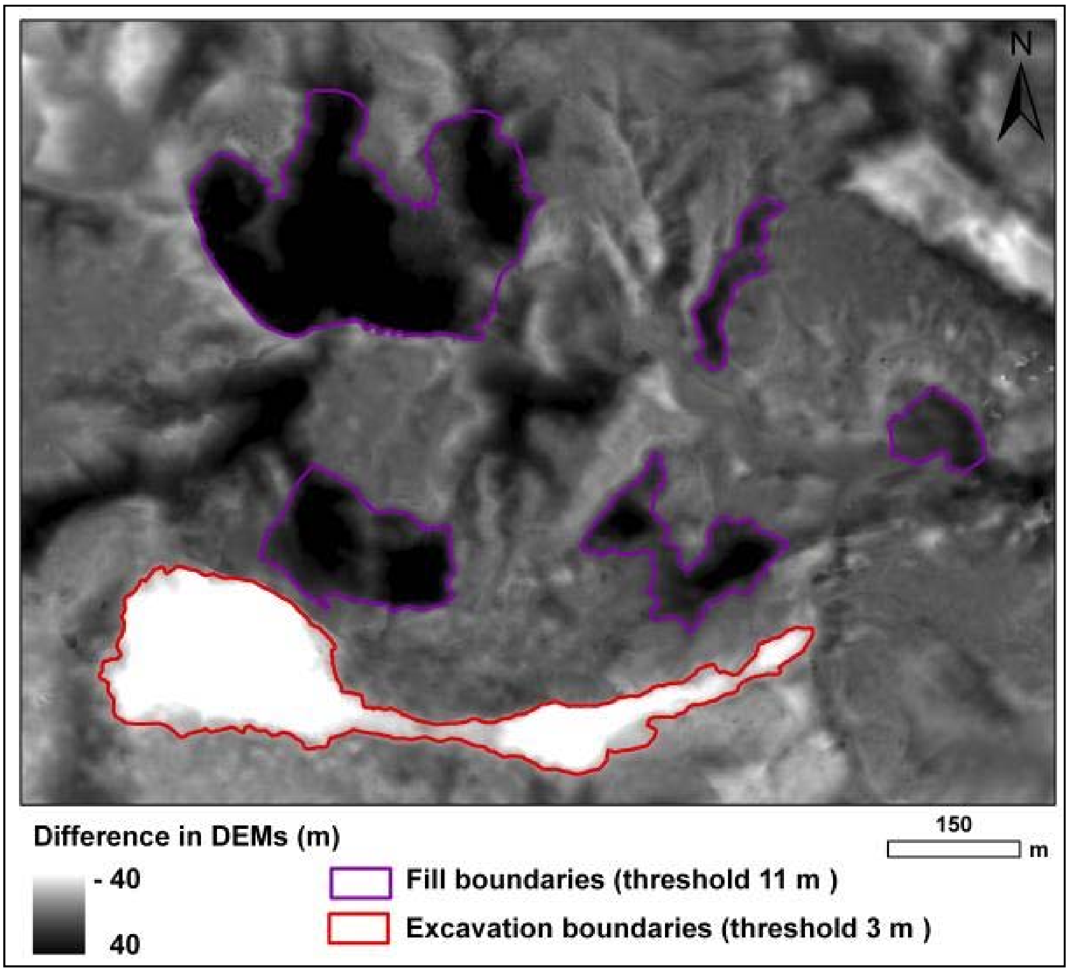

Figure 39 Difference in DEMs and change boundaries extracted by thresholding

Table 14 Volume changes in corresponding change polygons by DEM differencing and thresholding (11 m for fillings and 3 m for excavations)

Polygon Name	Polygon Description	Area (m^2)	Volume (m^3)
P	Open pit coal mine	62602	-1059100
D1	Primary dump site	71341	1625130
D2	Secondary dump site	22603	445245
D3	Tertiary dump site	15972	264503
C	Coal stock site	6681	92664
R	Mine road enlargement	6026	87295

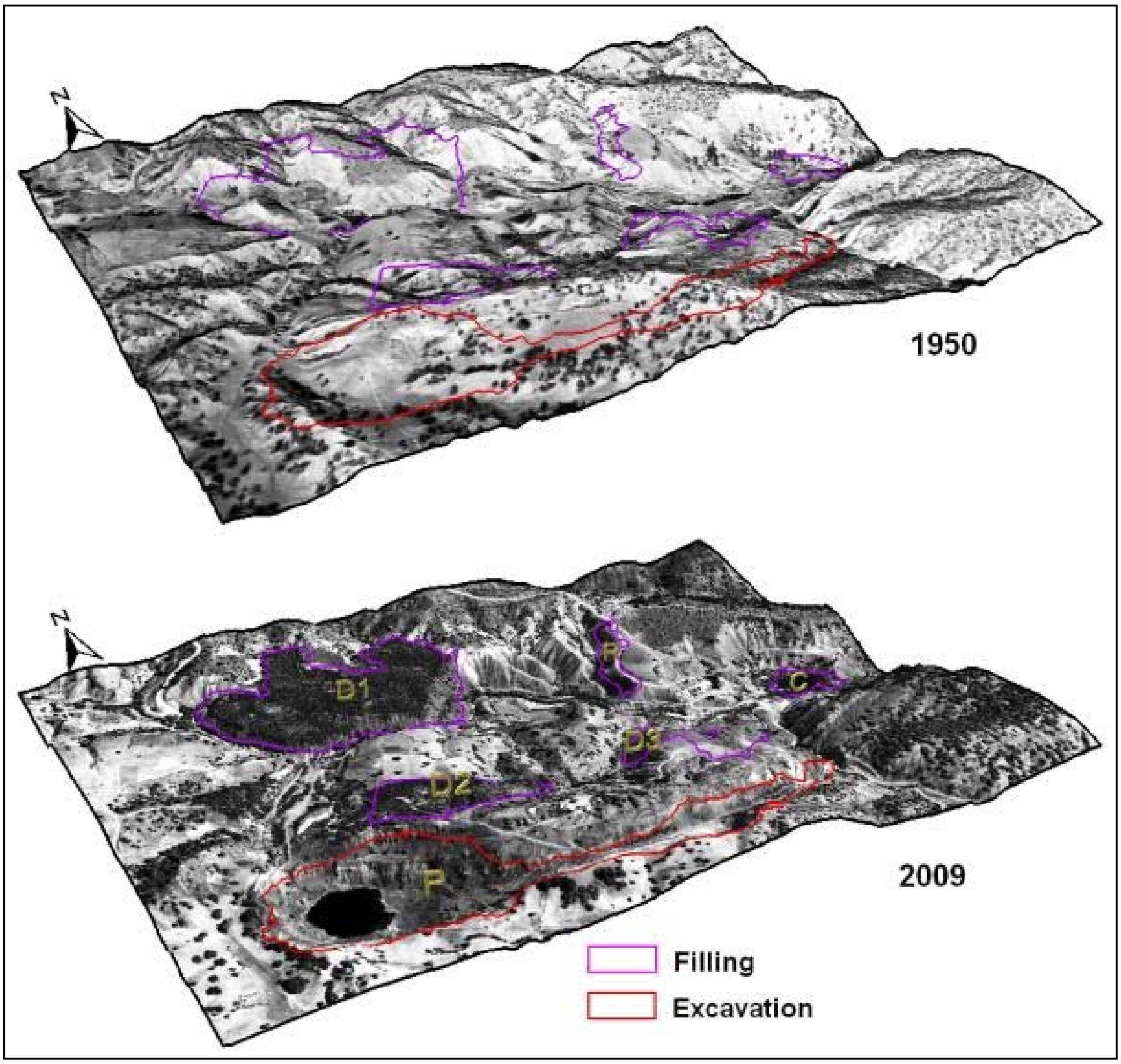

Figure 40 Terrain change polygons found by DEM differencing and thresholding (11 m for fillings and 3 m for excavations) for the year 1951 and 2009

Disturbance in Drainage Network

During extraction of pre-mining drainage characteristics from DEM dated 1951, first *fill sinks* procedure (Garbrecht and Martz, 2000) was applied to ensure that there were no depressions in the DEM representing artifacts in the model. The next step in the watershed analysis was the extraction of *flow direction.* The algorithm D8 (Jenson and Domingue, 1988) behind the *flow direction* determine surface runoff direction from any pixel to lowest pixel adjacent to it. After generation of raster layer showing flow direction, it was needed to calculate *flow accumulation* shown in Figure 41 by summing up total number of pixels contributing runoff to each pixel in the DEM (Garbrecht and Martz, 2000). Pixels with a high flow accumulation would probably become a part of the stream network when applying threshold.

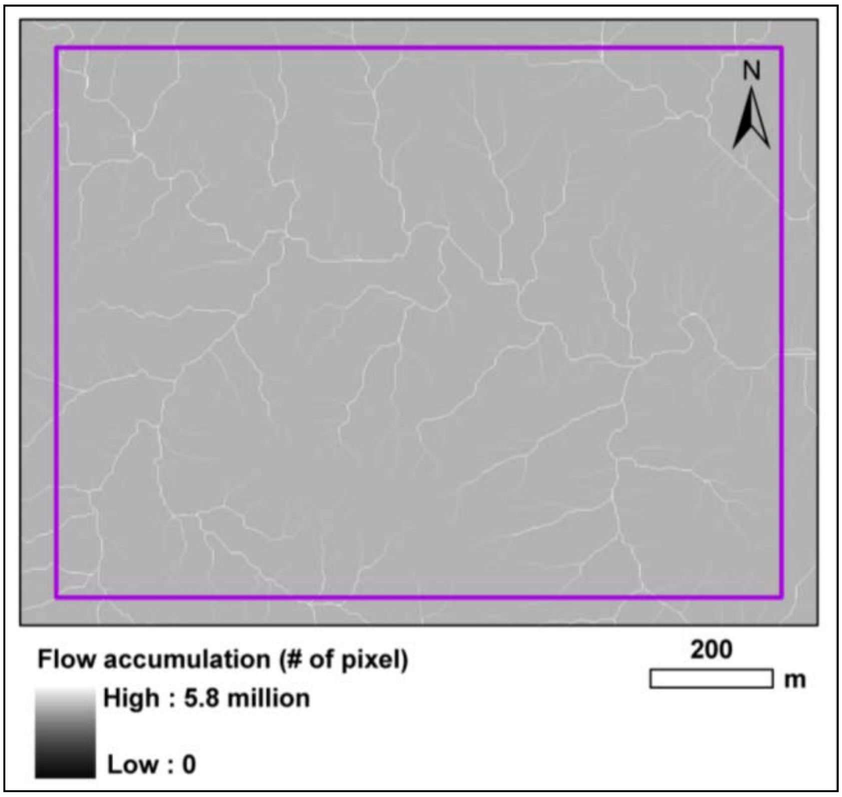

Figure 41 Flow accumulation in research area derived from pre-mining DEM dated 1951 with pixel size of 0.5x0.5 m

Once the flow accumulation map was created, stream network was derived from it by applying threshold such that all cells with more than the number of cells equal to the threshold value flowing into them would be part of the stream network. The threshold value was chosen as 1000 based on several iterations in order to select the value that result in a stream network visually neither too sparse nor too dense. Resultant stream network created by applying various threshold values were displayed in Figure 43 based on corresponding stream order. This stream order represents the order of each segments in the network based on *Strahler* method that suggest to increase stream order only when streams of the same order intersect (Strahler,1952). The number of stream order for each threshold value for the flow accumulation varied as 6, 5, and 4 for the threshold ranges of 100-1000, 3000-10000, and 20000-50000 respectively.

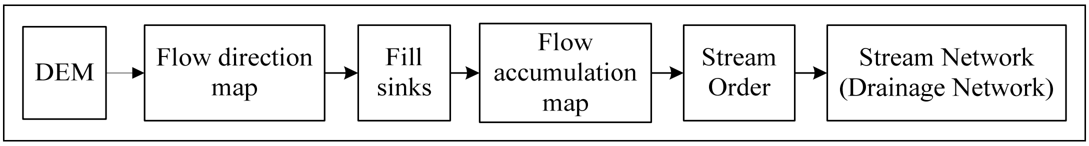

Figure 42 Drainage network extraction workflow for the year 1951

During extraction of post-mining drainage characteristics from DEM dated 2009, *fill sink* procedure was performed by introducing various depression depth thresholds iteratively as seen in Figure 44 in order not to fill the natural depression in which water bodies exist like the open pit lake. The optimal threshold value was found 5 m ensuring all depressions were filled except for water bodies. Three water bodies were found in the result of 5 m depression thresholding which were also detected during the field works. The first one was the open pit lake. The second and the third depressions shown in Figure 46 were formed by dumping overburden into valley adjacent to the primary dump site (D1). The pond within the depression located in northwest of the primary dump site was displayed in Figure 47.

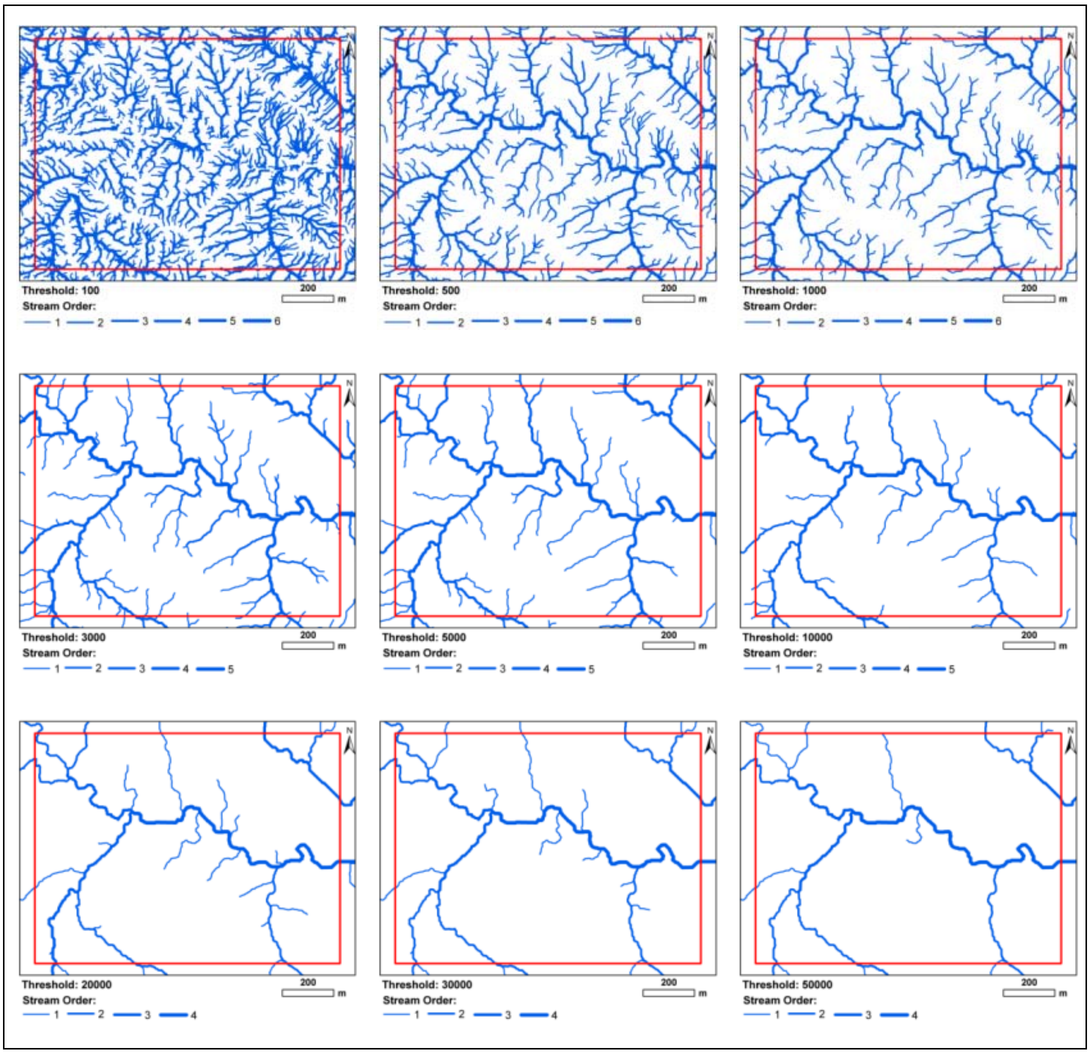

Figure 43 Stream network extracted by applying various thresholds to flow accumulation map with corresponding stream order. Threshold value 1000 was selected for stream network change analysis

Once producing a DEM free from artificial depressions for post-mining landscape, using the same methods introduced in pre-mining drainage network analysis, flow direction and flow accumulation maps were created. Since main objective was to determine disturbance of drainage network between pre- and post-mining landscapes, the stream network threshold was kept at 1000 during representation of stream network similar to pre- mining stream network extraction.

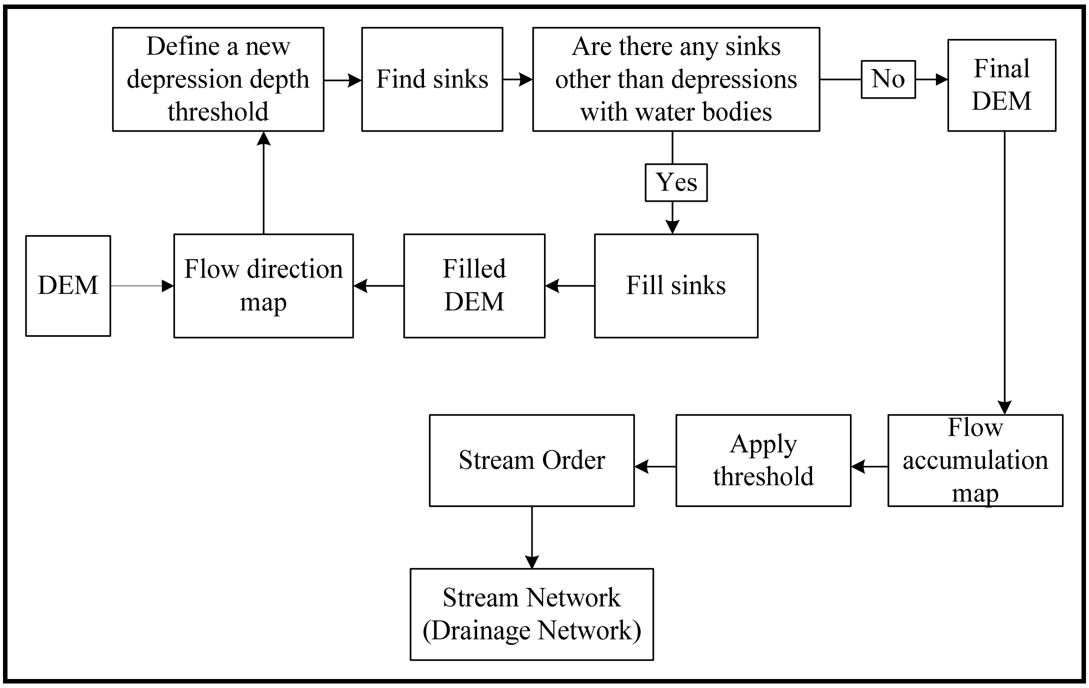

Figure 44 Drainage network extraction workflow for the year 2009

As seen in Figure 45, drainage network significantly changed after mining operation. Main diversions in the network were observed near open pit, primary dump site and the coal stock sites caused by cut and fill operations. Other minor changes were probably resulted from either intense erosion or errors during DEM generation. It can be better understood from Figure 46 that, in northern part of the primary dump site, two water ponds were formed after blocking drainage network by dump material. A scene from the pond located in the west was given in Figure 47. In the southern part of the primary dump site, main stream channel displaced towards south with a maximum displacement distance of 60 m.

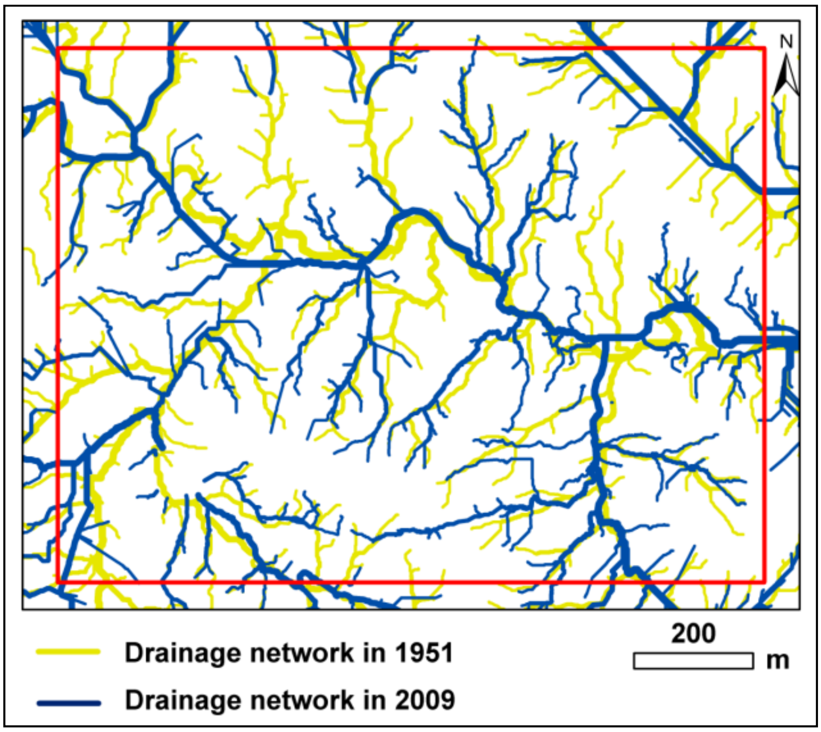

Figure 45 Drainage networks for pre- and post-mining landscapes across the condensed research area

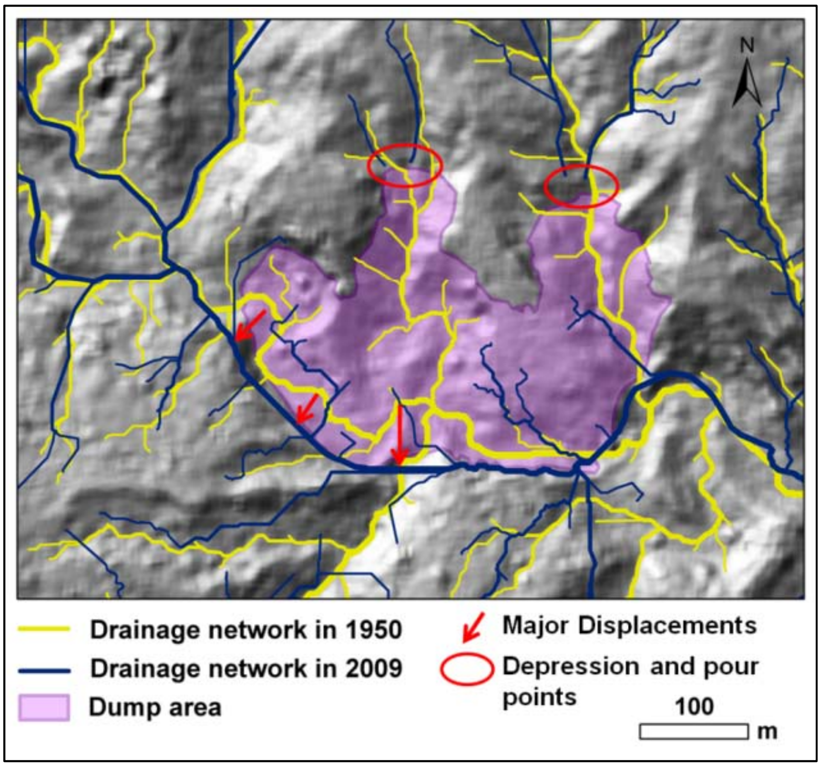

Figure 46 Disturbance of stream network around the primary dump site (D1) displayed on hill shade view of pre-mining DEM

Figure 47 A scene from the pond in the northwest of the primary dump site formed by blocking water drainage via dumping overburden into the valley

More intense disturbance was observed around the open pit as seen in Figure 48 and Figure 50. In the eastern part of the excavation area an open pit lake shown in Figure 49 was formed by excavation taking place on one of the main drainage segment. The lake was fed by two main stream network segments coming from southeast and northwest directions and probably by underground water because the lake was filled with water in dry seasons also.

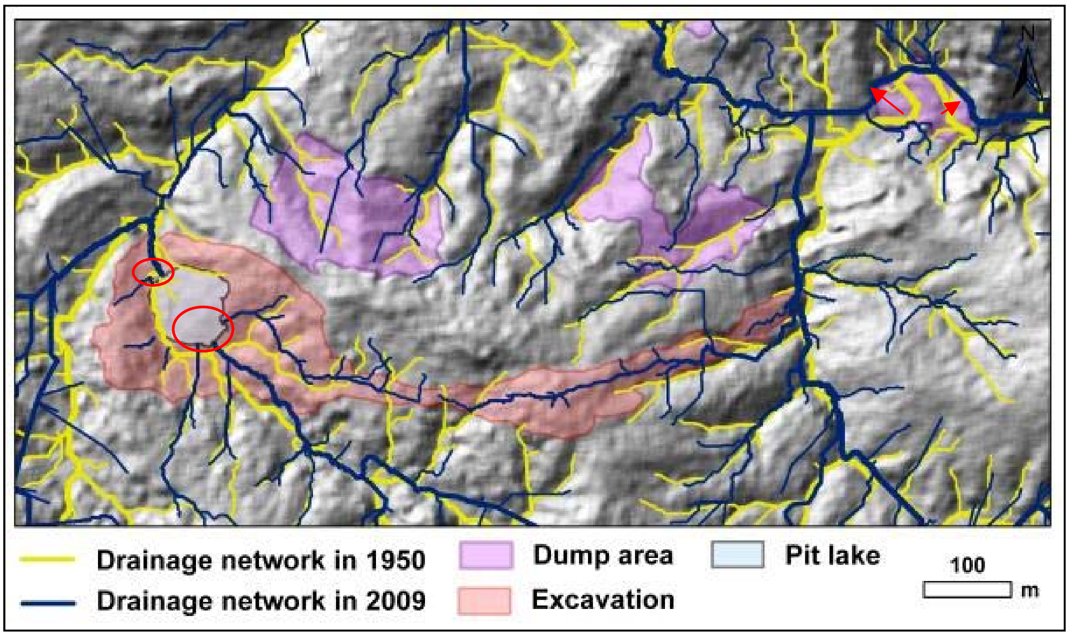

Figure 48 Disturbance of stream network around the around open pit displayed on hill shade view of pre-mining DEM


Figure 49 Open pit lake looking from northwest

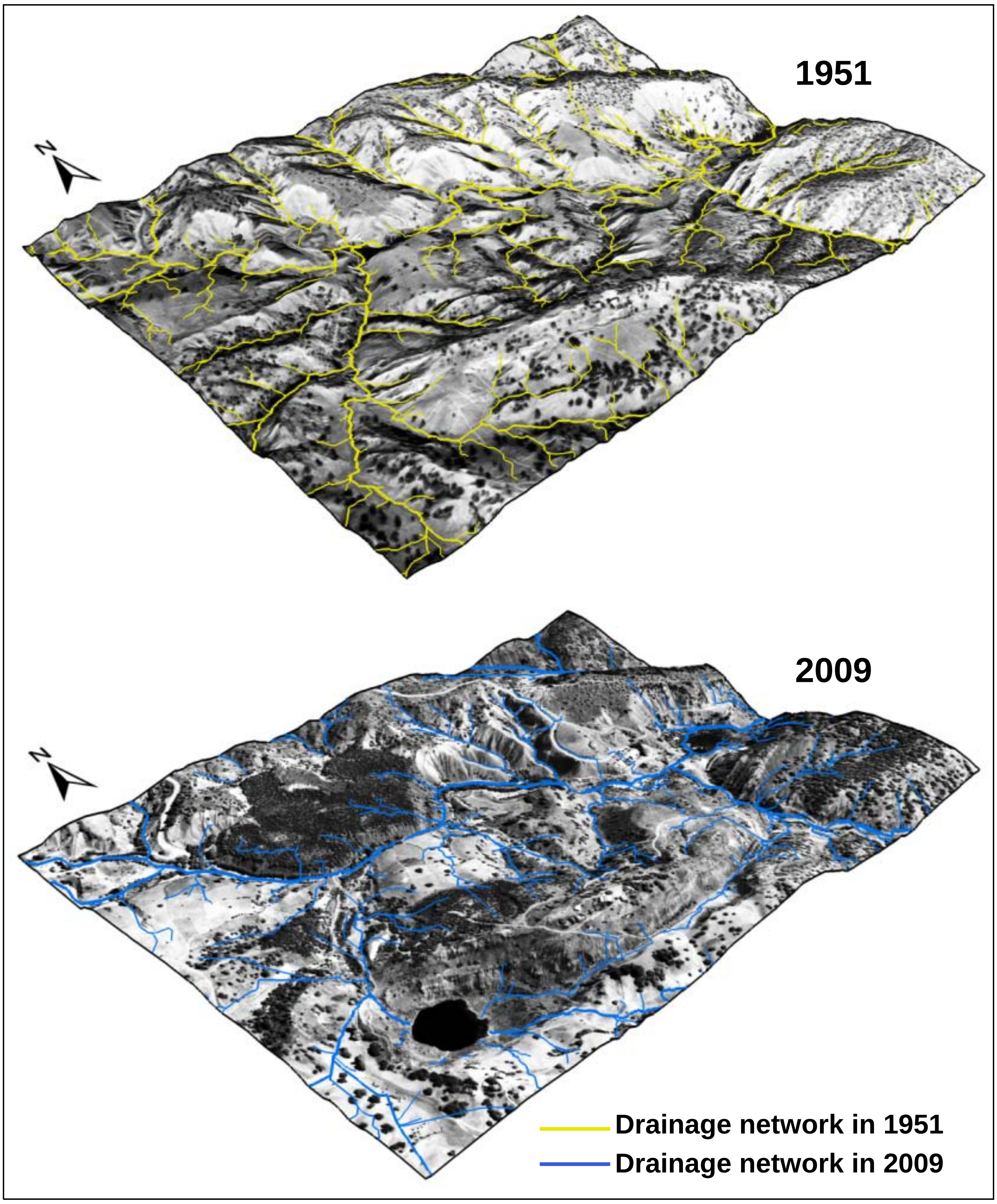

Figure 50 Drainage network lying on top of Aerial photo and Worldview-1 imagery draped on associated DEM dated 1951 (top) and 2009 (bottom) looking obliquely from southeast

Detection of Unstable Slopes

The slope maps were extracted using DEMs by *Spatial Analyst* tool in ArcGIS 9.3 for the pre- and post-mining stages of the condensed research area. As a result of mining activity in the research area slopes were highly changed. Maximum angle of slopes were 67 and 84 degrees for the pre- and post-mining stages of the region respectively. Slope maps were reclassified to 5 classes and associated land areas were calculated for pre- and post-mining terrain for each slope range. As seen in Table 15, from year 1951 to 2009, the area of each slope range larger than 30 degrees increased as a result of mining activity. The most steep slope regions depicted as very steep slope (> 60 degrees) has been increased from 265 m^2 to 3192 m^2.

As seen in Figure 51, in the classified slope map for the year 1951, slopes larger than 40 degrees were only observed where the rocky terrain exists which accounts for 3.51% of the site. In other words, naturally occurring slopes were in the range of 0 to 40 degrees except for rocky landscape in 1951.

As seen in the slope map of the year 2009 in Figure 51 and Figure 52, most of the moderate slopes (30-40) were accumulated in the borders of dump sites. This revealed that angle of repose for the dump material was between 30 and 40 degrees. The slope located in the north of the coal stock site was depicted as moderate slope both in 1951 and in 2009. In addition to that, most of the very steep slopes (> 60 degrees) were observed along the northern border of the open pit excavation.

Table 15 Various types of slope and their areas in 1951 and 2009

Slope Range (degree)	Slope Type	Area in 1951		Area in 2009	
		m^2	Percentage	m^2	Percentage
0-30	Gentle slope	911132	85.64	890566	83.71
30-40	Moderate slope	115295	10.84	131273	12.34
40-50	Sloping	30047	2.82	31561	2.97
50-60	Steep slope	7113	0.67	7260	0.68
60-90	Very steep slope	265	0.02	3192	0.30
Total		1063851	100	1063851	100

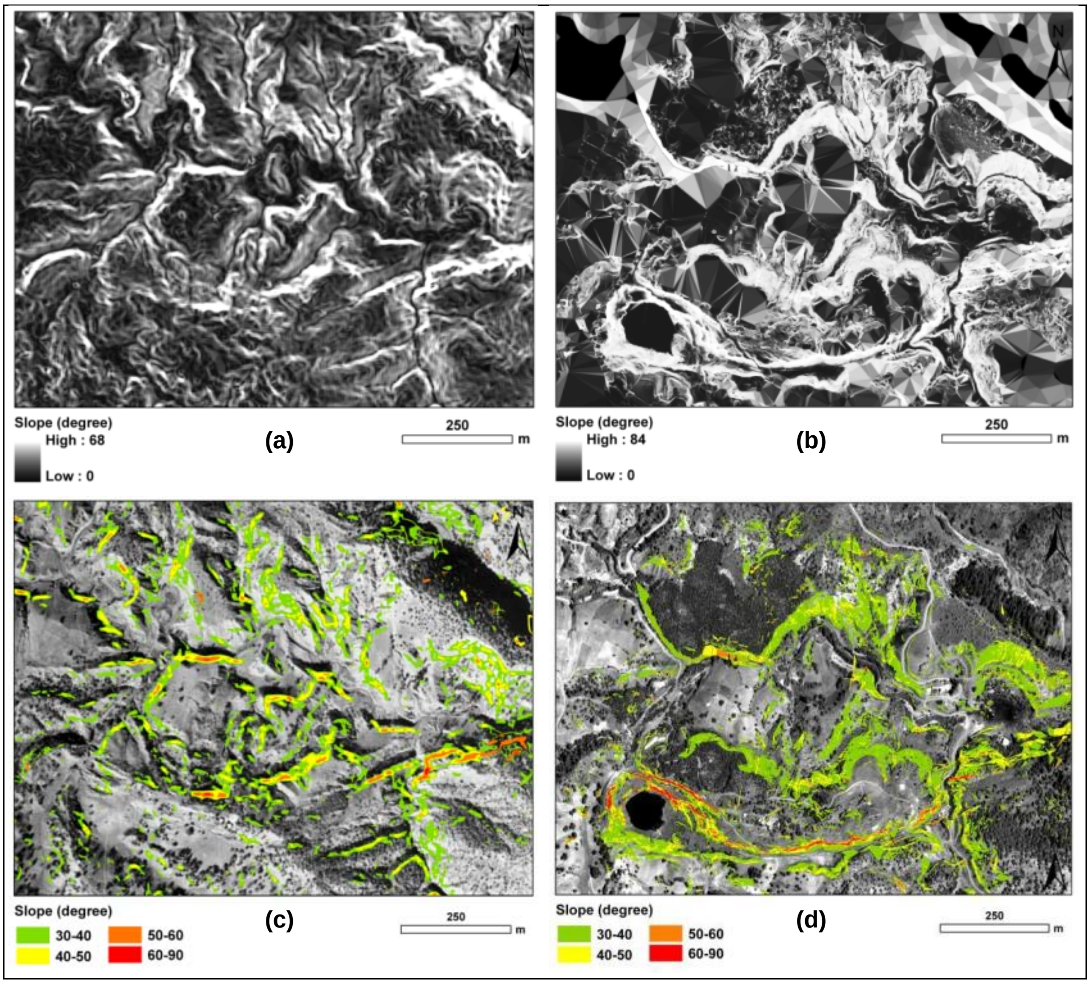

Figure 51 Slope maps of the condensed research area (a) in 1951, (b) in 2009 and reclassified slope maps (c) in 1951, (d) in 2009 overlaid with aerial orthophoto and Worldview-1 Satellite imagery respectively (in c and d, slopes lower than 30 degree were not represented)

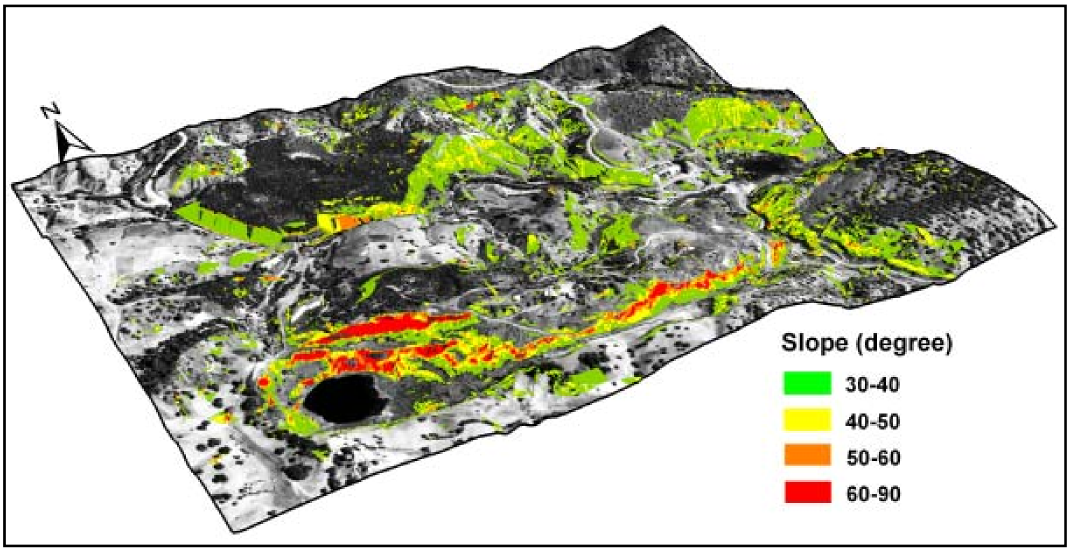

Figure 52 Perspective view of slope map overlaid with Worldwiew-1 satellite imagery (slopes lower than 30 degree were not represented)

The volume change polygons were overlaid with slope map as seen in Figure 53. Also areas of each slope range for each excavation and filling polygons were calculated and given in Table 16. The fact that mining activities are major causes of steep slope is distinctly observed from the difference between very steep slope percentages in disturbed and undisturbed land areas as % 0.90 and % 0.17 respectively. Very steep slope presence in disturbed land is approximately five times more than in undisturbed lands caused by excavation and filling operations. Most of the very steep slopes throughout the condensed research area were located within the excavation polygon as also observed in the field works.

Table 16 Area of land with respect to slope range and volume change polygons

Slope range (degree)	Disturbed lands (m2) Excavation P	Filling D1	D2	D3	C	R	Total Disturbed lands (m2)	Undistured lands (m2)	Total (m2)
0-30	36286	59329	17412	9811	6591	4663	134093	756473	890566
30-40	16488	9487	4726	5680	57	1274	37712	93561	131273
40-50	5932	2034	418	448	28	89	8949	22611	31561
50-60	2238	478	47	32	5	0	2800	4460	7260
60-90	1658	13	0	1	0	0	1671	1520	3192
Total	62602	71341	22603	15972	6681	6026	185225	878626	1063851

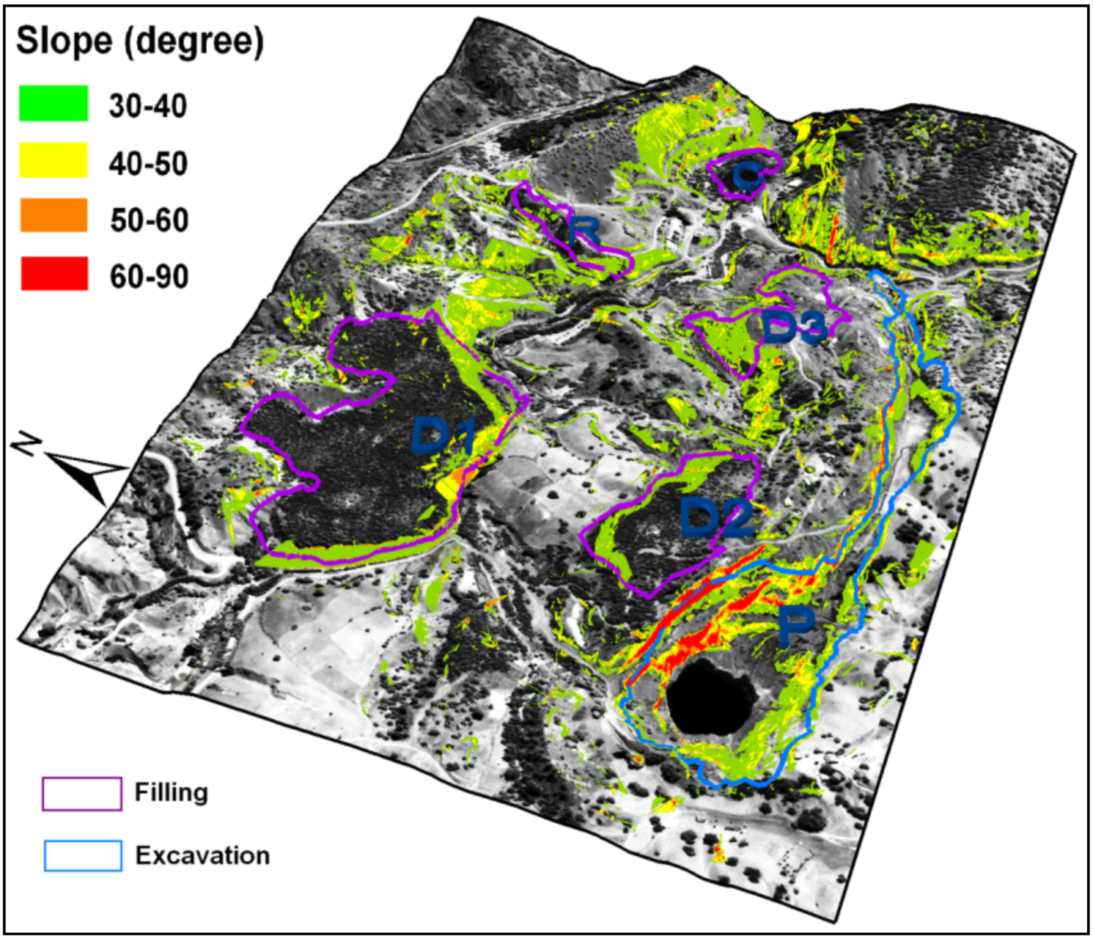

Figure 53 Perspective view of slope map overlaid with volume change polygons and Worldwiew-1 satellite imagery draped on DEM (slopes lower than 30 degrees were not represented)

3.7.2 Land Use and Land Cover (LULC) Mapping

Land cover is defined by Comber et al. (2005) as the physical material at the surface of the earth. Land covers consist of forest, barelands, grass, water bodies. On the other hand, land use is defined differently by natural and social scientists. According to natural scientists, land use is the modification of natural environment by humanity into built environment such as agricultural lands and settlements. Social scientists broaden the definition of land use to include the social and economic purposes and contexts of management or -left unmanaged- of lands subsistence versus commercial agriculture, rented vs. owned, or private vs. public land (Ellis, 2007).

It is important to map Land Use and Land Cover (LULC) for the past and the current stages of the mine site and to observe the changes induced by mining activity.

In this study, two methods were implemented in LULC mapping. The first method was the manual screen digitizing of LULC classes on very high resolution aerial photos (0.7m) and Worldview-1 (m). The aim of this method was to extract detailed pre- and post-mining LULC in order to detect mining induced changes on LULC. The second method was supervised image classification. In the supervised classification method ASTER dataset was used. Landsat dataset was eliminated from image classification due to coarse spatial resolution. The aim of this method was to investigate the efficiency of ASTER dataset to classify LULC in the abandoned mine site in 2002 and in 2007.

Two different change detection algorithms were implemented to determine changes between pre- and post-mining stages of the site; namely, image differencing and post classification comparison. Descriptions of these algorithms were given in section 2.2.

LULC Mapping Based on Image Interpretation and Screen Digitizing using Aerial Photos and Worldview-1 Satellite Image

Orthorectified black and white aerial photo and Worldview-1 Satellite image with spatial resolution of 0.7 m and 0.5 m respectively were used to produce LULC map of the condensed research area based on image interpretation and screen digitizing for pre- and post-mining landscape. Forest map and GCPs were used as ancillary data during LULC mapping. The resultant maps were established as ground truth and later used in accuracy assessment of Landsat and ASTER image classifications.

Based on aerial photo interpretation, the study area was classified into four main LULC classes as forest, bareland, agriculture and sparse buildings for the year 1951 shown in Figure 54. By the help of the forest map, it was possible to divide forest class into four subclasses as black pine, dense oak, sparse oak and pine & oak displayed in Figure 55. Forest class was used without considering subclasses in change detection analysis to simplify representation of mining induced LULC change, and to make it comparable with image processing results of Landsat and ASTER images.

LULC map was produced for the current state of the site based on Worldview-1 image, forest map and observations conducted in the field studies. In addition to the classes defined in LULC study for the pre-mining landscape, mining induced four new classes induced by mining activities - excavation, dump, coal stock and lake- were identified during image interpretation and confirmed in the field studies. LULC map produced for current state of the research area was displayed in Figure 56.

As seen in Figure 57, two of the three dump sites in the eastern part of the research area were afforested by locust trees. However, the one located in southwest was not afforested. An open pit lake was formed within the excavation.

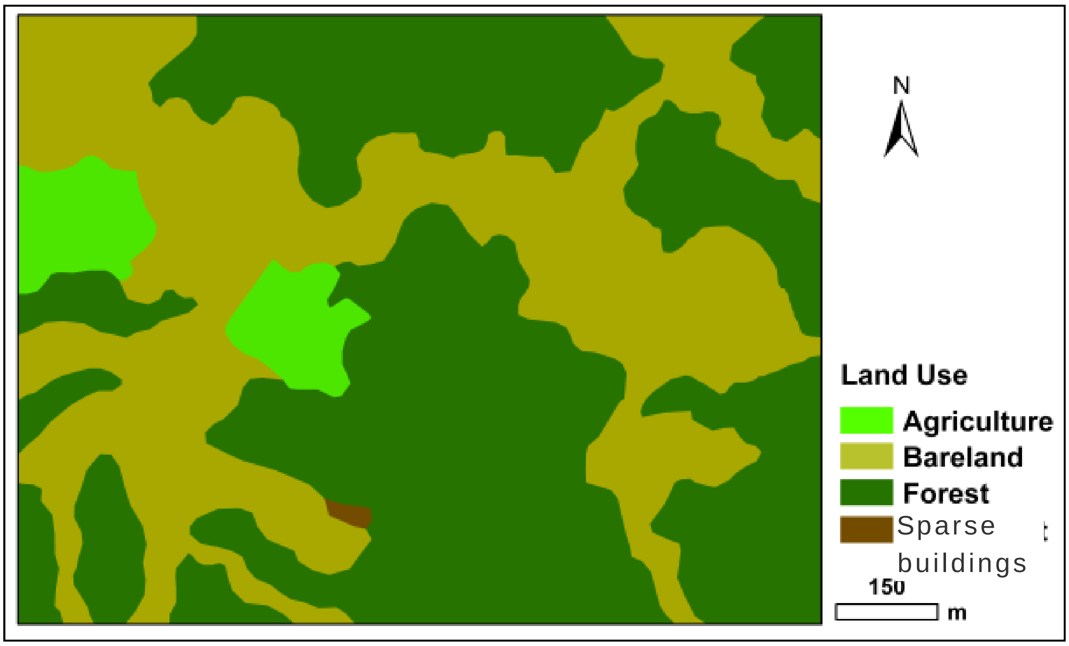

Figure 54 Pre-mining LULC map of the research area derived from orthorectified aerial photo dated 1951

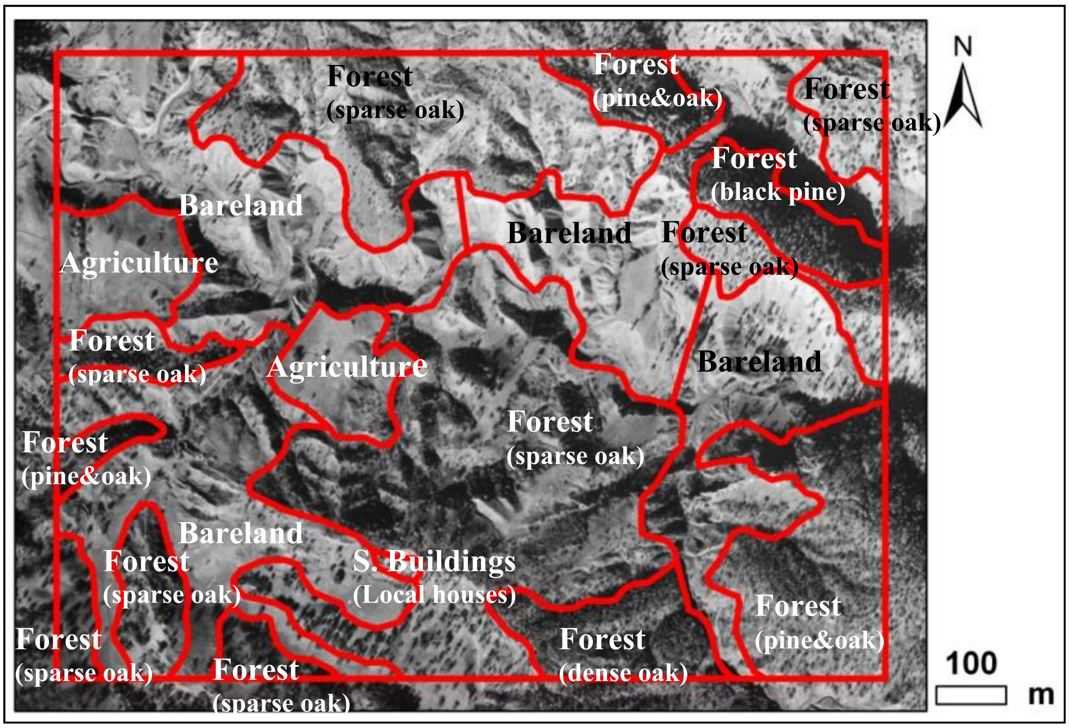

Figure 55 Pre-mining LULC map including forest subclasses displayed on orthorectified aerial photo dated 1951

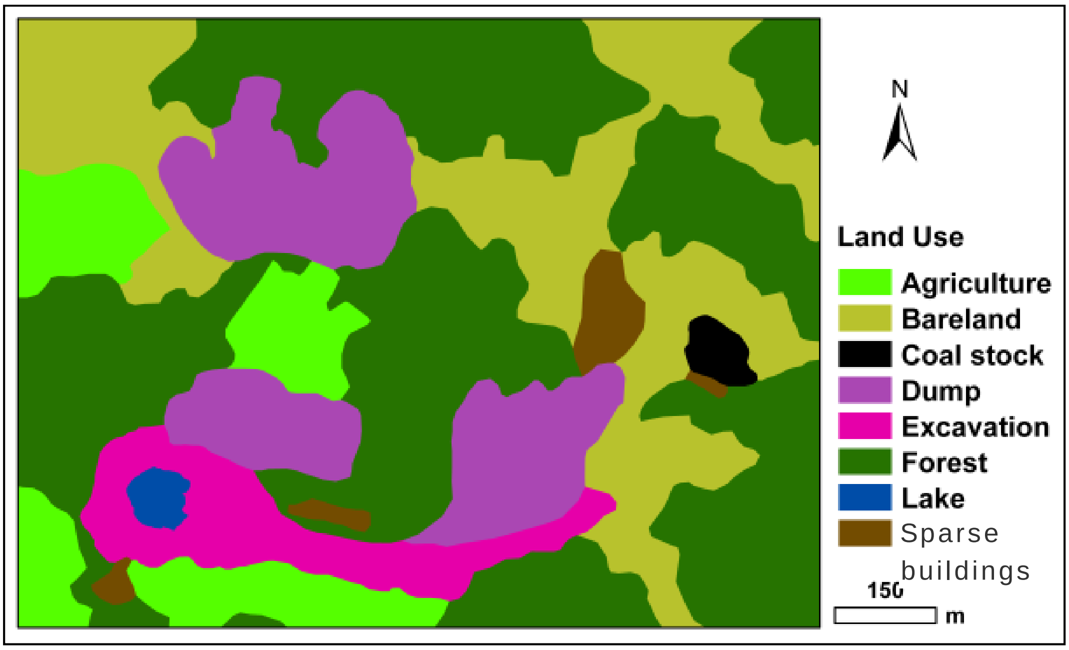

Figure 56 Post-mining LULC map of the condensed research area derived from Worldview-1 satellite imagery dated 2008

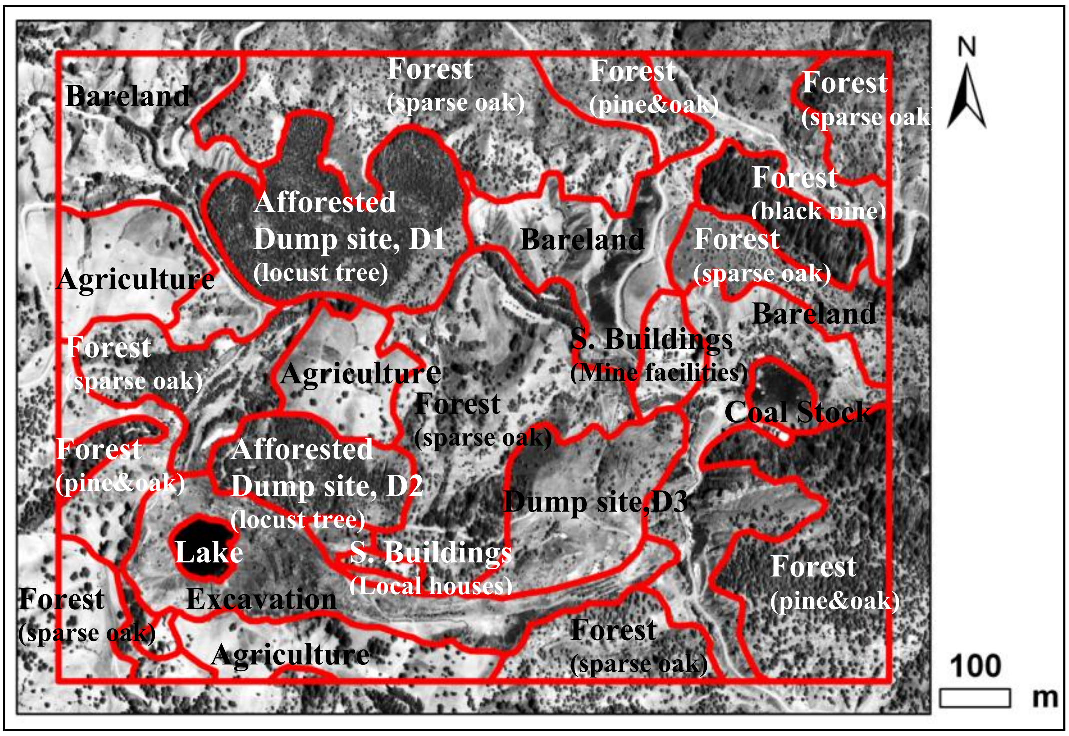

Figure 57 Post-mining LULC map including dump and forest subclasses displayed on orthorectified Worldview-1 imagery

LULC Mapping based on Supervised Image Classification of ASTER imagery

Supervised image classification of ASTER imagery taken in 2007 was performed in ENVI 4.7 software environment. The ASTER dataset was obtained as orthorectified in UTM projection with WGS1984 datum. During supervised image classification of ASTER imagery, the procedure given in Figure 58 was followed.

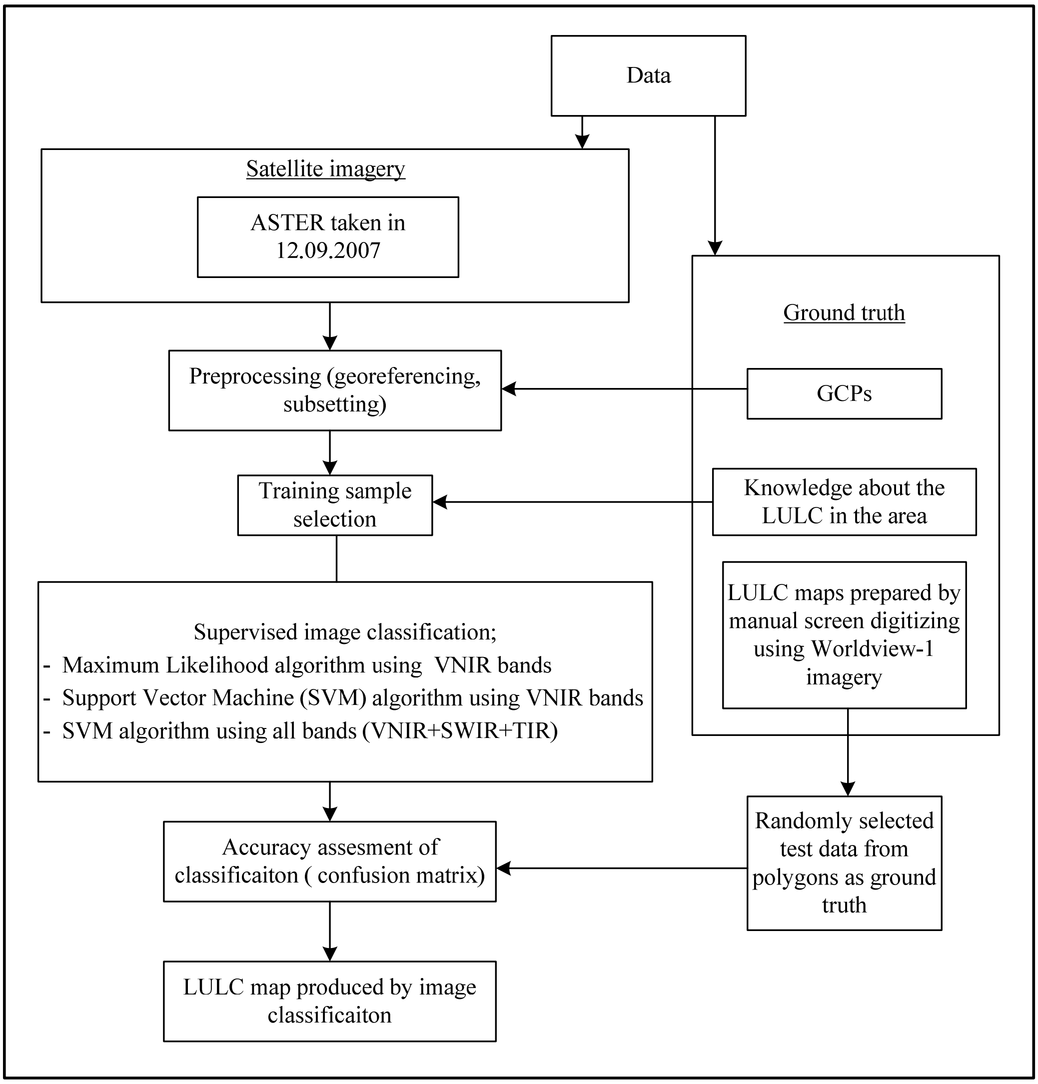

Figure 58 Supervised image classification procedure for ASTER dataset

In this procedure, the first step was the preprocessing of the imagery set. In this step, ASTER 2007 dataset was georeferenced with collected GCPs. The Nearest

Neighbor resampling algorithm was preferred in georeferencing process. Moreover, subsets were extracted in order to focus the condensed research area.

The second step was the selection of training samples which were representative and typical for each of LULC classes identified in the previous section. The selection was based on the field observations, interpretation of various color composite of ASTER imagery, and the Worldview-1 imagery as an ancillary data source. Figure 59 show the distribution and number of pixels for each class of training sample used in supervised classification of ASTER imagery taken in 2007.

The third step was the implementation of two different supervised classification algorithms, Maximum Likelihood and Support Vector Machine (SVM). In this step, three different classification procedures were performed; Maximum Likelihood using VNIR bands, SVM using VNIR bands, and SVM using all bands (VNIR+SWIR+TIR) for ASTER imagery taken in 2007. The aim of combining bands from different sensors was to integrate the data in order to obtain more information that cannot be obtained from single sensor data alone.

In maximum likelihood classification probability threshold was set to zero so that all the pixels were forced to assign one of the classes. During implementation of SVM classification, default parameters of ENVI 4.7 used as kernel type was radial basis function, gamma in kernel function was 0.071, penalty parameter was 100 and probability threshold was zero. Three different classified images were obtained at the end of the image classification step illustrated in Figure 60. As seen in the Figure 60, the result of maximum likelihood classification has noisier appearance than the results of SVM classification. It was observed that, increasing the number of bands in SVM classifier decreased the noisy appearance in the classification results.

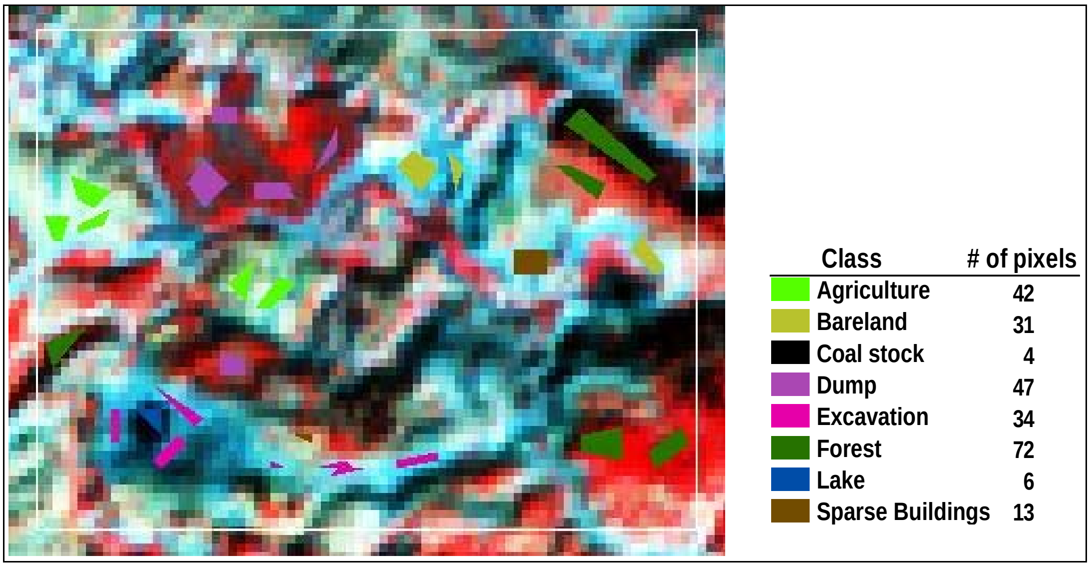

Figure 59 Distribution and number of pixels of training sample for classification of ASTER imagery taken in 2007 (The background image- false color RGB: 321- was enhanced by histogram equalization)

The fourth step was the accuracy assessment of the classification results. Accuracy assessment is a process of assessing classification results by comparing ground truth. The most command method of showing classification accuracy is to prepare a confusion matrix (error matrix). Once confusion matrix was produced, Overall Accuracy, Producer's Accuracy and User's Accuracy for each class can be computed. Another method of assessing accuracy of the classification is to calculate Kappa Statistics which is a measure of the actual agreement between the reference data and an automated classifier and the chance of agreement between the reference data and a random classifier (Lillesand, 2004). In order to assess the classification results, a test sample was required as ground truth. The required test sample was prepared by randomly selecting 30% of each class from the LULC map produced by manual screen digitizing of Worlview-1 imagery. The distribution and pixel numbers of the test sample for each class were given in Figure 61. The confusion matrices, Overall Accuracy, Producer's Accuracy, User's Accuracy, and Kappa statistics of three classification results were displayed in Figure 62.

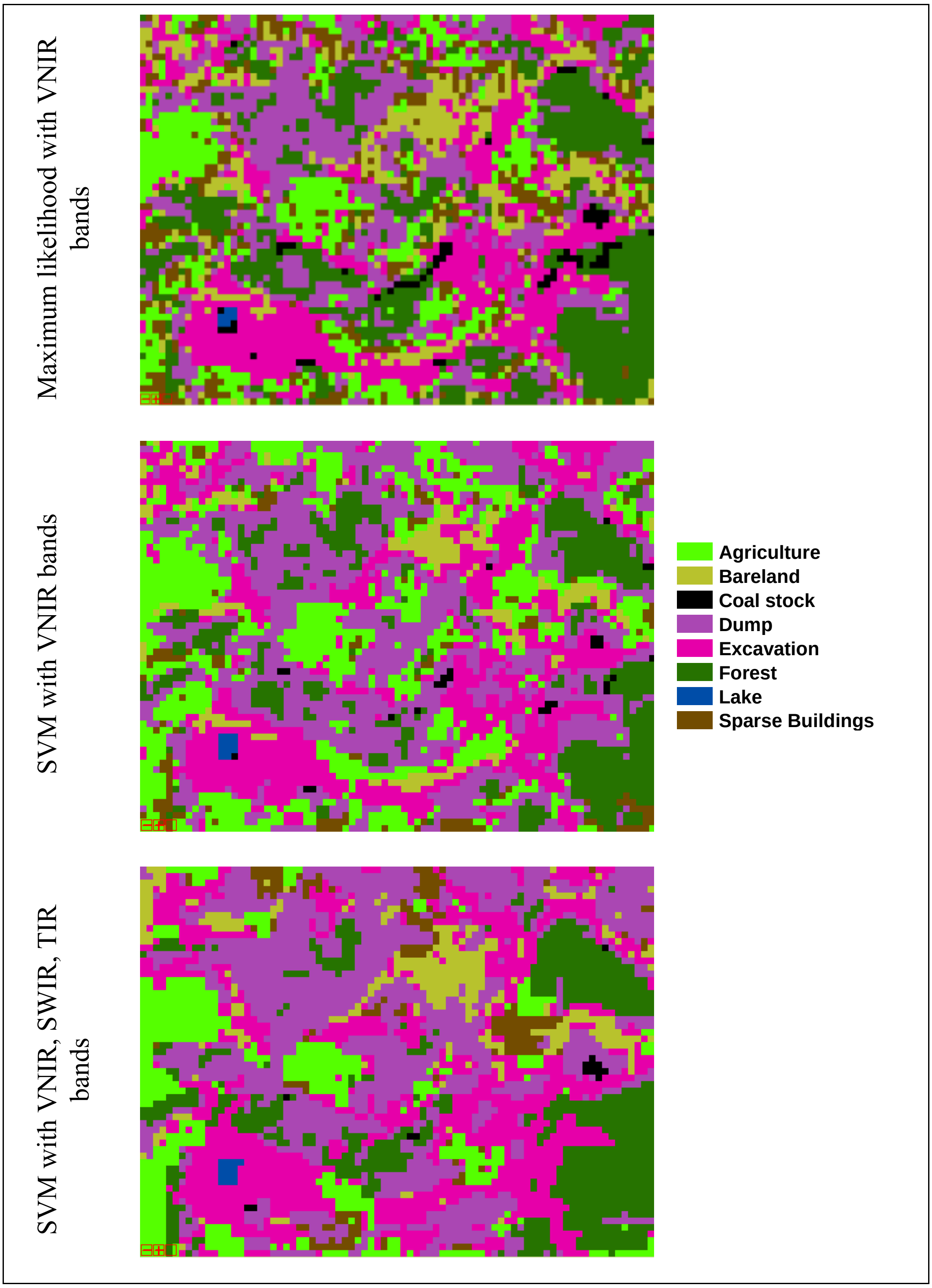

Figure 60 Classification results of ASTER dataset by Maximum likelihood and Support Vector Machine (SVM) classifiers

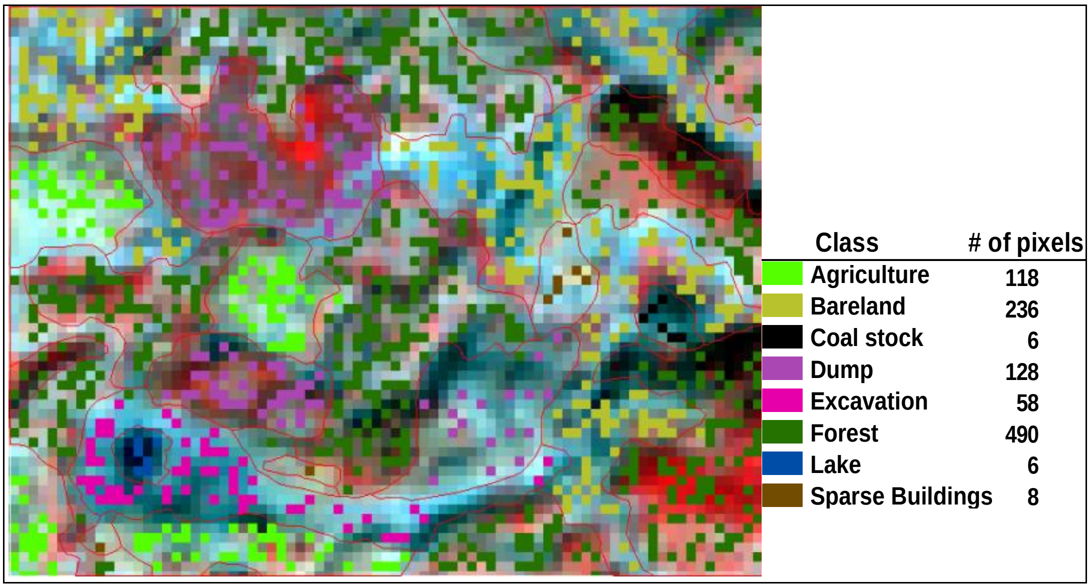

Figure 61 Distribution and number of randomly selected test pixels

As seen in Figure 62, the overall accuracy of Maximum likelihood classification for VNIR bands of ASTER dataset taken in 2007 was 41%. The classes “Forest” and “Agriculture” were extracted without much misclassification with relatively higher Producer’s and User’s accuracies. The other classes such as “Sparse Buildings”, “Lake” and “Coal” were prone to some amount of misclassification with relatively lower Producer’s and User’s accuracies. This was perhaps due to smaller areal extent of these classes which caused to insufficient set of training sample and mixed spectral reflectance at the boundaries. In the case of SVM classification with VNIR bands, the overall accuracy was 33%. It was observed that, distinguishing “Bareland” and “Excavation” classes was poor showing lower Producer’s and User’s Accuracies due to similar spectral signatures in both maximum likelihood and SVM classifications. Adding the SWIR and TIR bands to the SVM classification procedure apparently increased the classification accuracy. Overall accuracy increased to 39% with showing enhancement in both Producer’s and User’s Accuracy for all classes. The overall classification accuracies were generally low probably because of very low classification accuracy of some individual classes such as lake, sparse buildings which were very small areal extent with respect to pixel size of the satellite imagery. This also reduced the overall accuracy.

	Ground Truth (pixels)									
Class	D	A	F	C	L	S	B	E	T	U. A.
D	67	4	126	0	0	0	44	0	241	28
A	6	71	54	0	0	3	17	1	152	47
F	35	8	183	0	0	0	11	0	237	77
C	2	0	3	1	3	0	2	0	11	9
L	0	0	0	0	2	0	0	0	2	100
S	3	22	58	0	0	3	24	0	110	3
B	5	1	35	0	0	0	55	6	102	54
E	10	12	31	5	1	2	83	51	195	26
T	128	118	490	6	6	8	236	58	1050	
P. A.	52	60	37	17	33	38	23	88		
Overall Accuracy = 41% Kappa Coefficient = 0.2812										

(a)

Confusion matrix for Maximum Likelihood classification of ASTER dataset taken in 2007 (a)

	Ground Truth (pixels)									
Class	D	A	F	C	L	S	B	E	T	U. A.
D	69	17	208	0	0	1	55	0	350	20
A	7	80	112	0	0	3	38	1	241	33
F	35	2	112	0	0	0	6	0	155	72
C	1	0	1	0	1	0	2	0	5	0
L	0	0	0	0	4	0	0	0	4	100
S	0	9	21	0	0	2	2	0	34	6
B	0	0	3	0	0	2	33	6	44	75
E	16	10	33	6	1	0	100	51	217	24
T	128	118	490	6	6	8	236	58	1050	
P. A.	54	68	23	0	67	25	14	88		
Overall Accuracy = 33 % Kappa Coefficient = 0.2108										

(b)

SVM classification using VNIR bands of ASTER dataset in 2007 (b)

	Ground Truth (pixels)									
Class	D	A	F	C	L	S	B	E	T	U. A.
D	89	19	192	1	0	0	49	2	352	25
A	8	70	42	0	0	1	10	4	135	52
F	17	3	134	0	0	0	14	0	168	80
C	1	0	1	1	0	0	1	0	4	25
L	0	0	0	0	6	0	0	0	6	100
S	0	7	28	0	0	4	7	0	46	9
B	5	1	14	0	0	0	53	0	73	73
E	8	18	79	4	0	3	102	52	266	20
T	128	118	490	6	6	8	236	58	1050	
P. A.	70	59	27	17	100	50	22	90		
Overall Accuracy = 39 % Kappa Coefficient = 0.2733										

(c)

SVM classification using VNIR+SWIR+TIR bands of ASTER dataset taken in 2007 (c)

Agriculture (A); Dump (D); Forest (F); Bareland (B); Excavation (E); Sparse Buildings (S); Coal Stock (C); Lake (L); Total (T); Production Accuracy in % (P.A.); User Accuracy in % (U.A)

Figure 62 Accuracy assessment of image classification results

3.7.3 Progressive Land Change Analysis in the Mine Site

Monitoring changes on Earth's terrestrial surface caused by human activities became one of the main problems for today's scientists (Ellis, 2007). Humans have been modifying land to obtain food and other essentials for thousands of years. However, current LULC change rates, extents and intensities are far greater than ever in history. This also result in unexpected changes in ecosystems and environmental processes at local, regional and global scales including climate change, biodiversity loss and the pollution of water, soils and air (Ellis, 2007). Observing changes on land surface in the mine site is one of the parameters to assess land degradation caused by mining activities.

In this study, a progressive change analysis approach was implemented shown in Figure 63. Two different change detection algorithms were applied to detect changes across the condensed research area from pre-mining state to post-closure state.

The first algorithm was *image differencing* using individual bands and Normalized Difference Vegetation Index (NDVI). For this purpose multidate Landsat and ASTER satellite images were used. The aim of image differencing was to test effectiveness of the algorithm in detecting mining induced changes by comparison of spectral reflectance and NDVI of individual pixels in different dates. The results of the procedures were the maps of "Change" vs. "No-change" for band differencing and "Decrease in NDVI", "Increase in NDVI" and "No-change" for NDVI differencing.

The second algorithm was the *post classification comparison* using LULC maps generated using aerial photo and Worldview-1 imagery. The aim of post classification comparison approach was to map the changes and calculate areal extent of each type of change across the condensed research area.

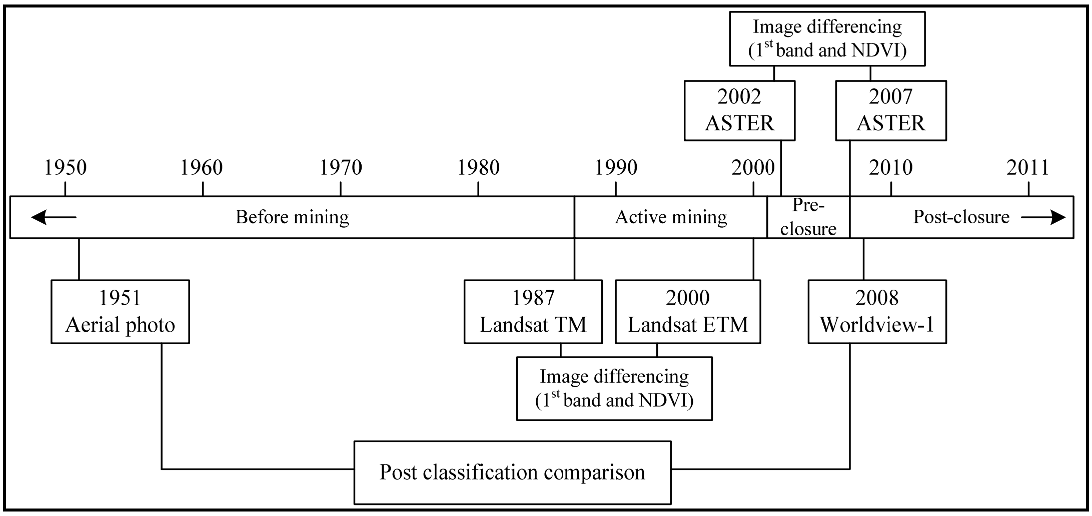

Figure 63 Progressive land change analysis with data sources and change detection algorithms

Implementation of image differencing algorithm

The objective of the image differencing approach was to produce a new change image between two dates by subtracted two co-registered images pixel by pixel. Two sets were compared in this section. The first comparison set was consisted of the two images recorded by Landsat TM in July, 1987 and Landsat ETM in July, 2000. The second set was also consisted of the two images captured by ASTER in November, 2002 and in September, 2007. Band differencing and NDVI differencing procedures were applied for both imagery sets. The first band of Landsat and ASTER imagery was selected for band differencing procedure.

In the band differencing section, first band of Landsat TM taken in 1987 was subtracted from Landsat ETM taken in 2000 pixel by pixel after normalization of pixel values to values between 0 and 1. A threshold value was selected by several trials illustrated in Figure C1 as 0.2 to determine change and no-change pixels based on land use pattern. That is, a pixel having a difference value between -0.2 and 0.2

was considered as no-change in the difference image. The first bands of Landsat TM and Landsat ETM images and the threshold applied difference image were given in Figure 64 (a), (b) and (c) respectively. As seen in the figures (a) and (b), inspection of individual first bands of Landsat dataset did not give much information on mining induced changes between 1987 and 2000 due to having coarse spatial resolution (28.5 m). However, change image (c) delineated the change areas where mining excavation took place and overburden material dumped. The similar image differencing procedure explained above was employed for the ASTER pair captured in November, 2002 and July, 2007. The first bands of the pair and the change image produced by applying the same threshold value (0.2) to the difference image were given in Figure 64 (d), (e) and (g) respectively. Also various threshold applied was illustrated in Figure C1. As seen in Figure 64 (g), a considerable amount of change in spectral reflectance was delineated. It was observed that there was a strong correlation between distribution of change pixels and agricultural areas. Therefore, one of the main reasons of spectral reflectance change might be the seasonal difference in acquisition dates of multidate ASTER pair.

In the NDVI differencing section, once the NDVI for Landsat and ASTER pairs were produced, the normalized NDVI images for final stages were subtracted from the initial stages. Then, various threshold values were applied as seen in Figure C2 and the same threshold value (0.2) was selected for difference images such that the pixels having value lower than -0.2 were designated as “Decrease in NDVI”, between -0.2 and 0.2 as “No-change” and values higher than 0.2 were marked as “Increase in NDVI”. NDVI and change images for Landsat and ASTER pairs were given in Figure 65. As seen in Figure 65 (c), excavation area was pointed out by clustering the change pixels marked as “Decrease in NDVI”. Some clustering of “Increase in NDVI” change pixels was observed in one of the agricultural area located in the north of the excavation. The result of NDVI differencing of ASTER imagery pair revealed an increase in NDVI in dump sites afforested by locust trees shown in Figure 65 (g).

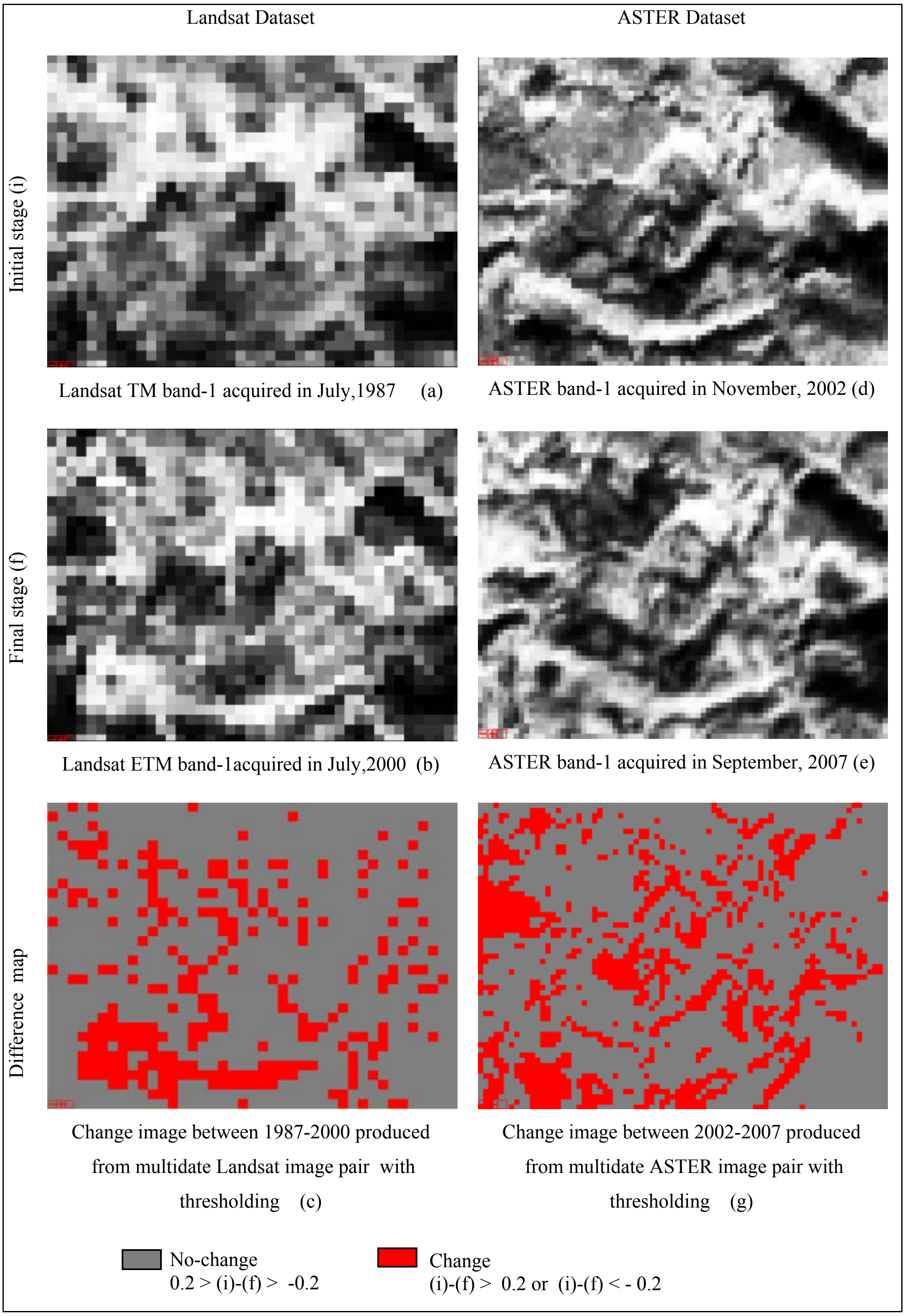

Figure 64 Image differencing change detection results of first band of Landsat and ASTER dataset

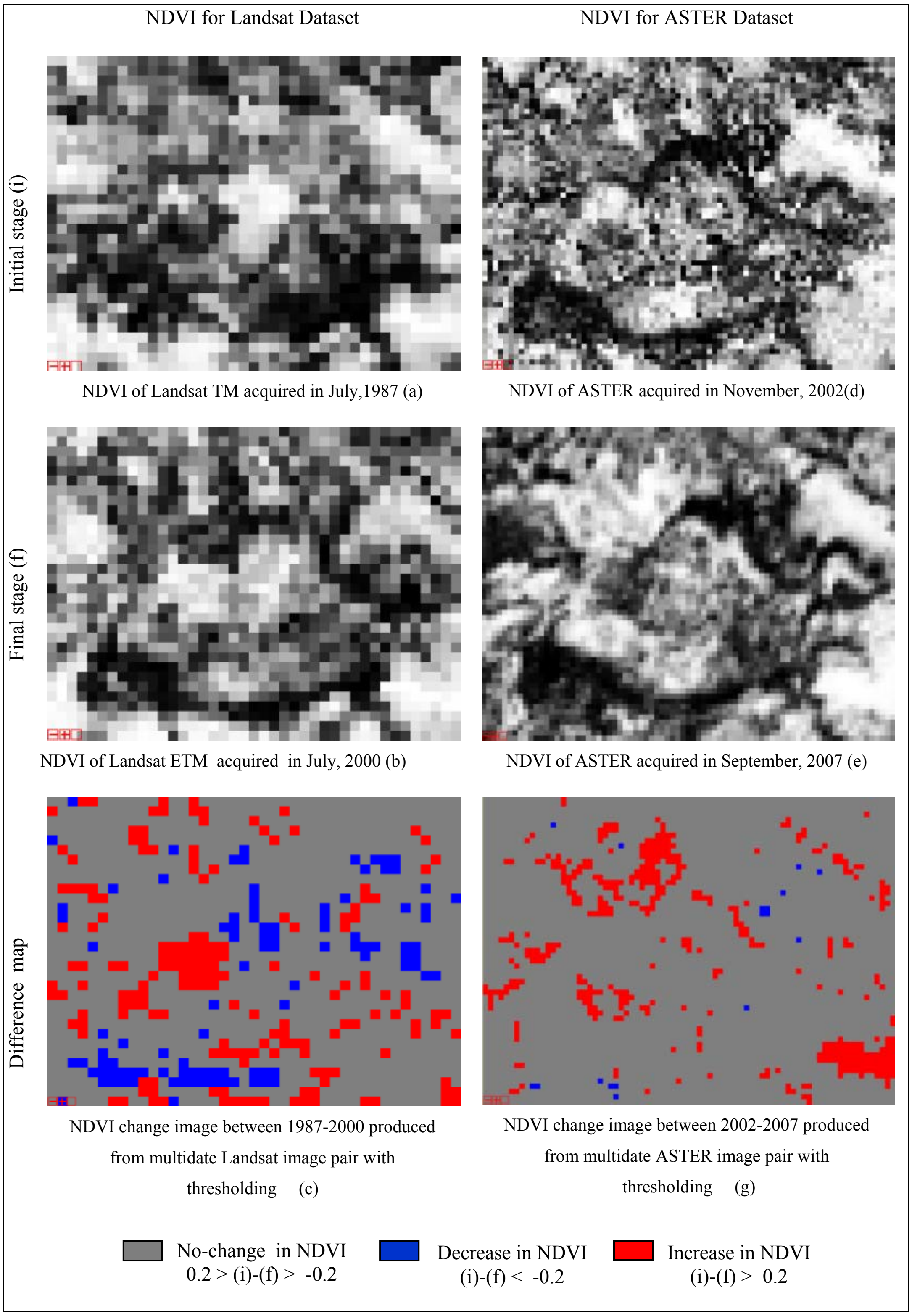

Figure 65 Image differencing change detection results of NDVI produced from Landsat and ASTER dataset

Implementation of post classification comparison algorithm

Mining induced changes in LULC was detected by using *intersect* tool in ArcGIS software environment using LULC maps produced for pre- and post-mining stages of condensed research area. As seen in change map given in Figure 66, most of the LULC change was observed in southwest part of the site where excavation took place. Change categories and their areal amounts were given in Table 17 in the form of a change matrix. As shown in this table, both open pit excavation and overburden dumping took place on forest and bareland. The area of forest damaged by open pit excavation was more than the area of bareland as 37,595 m^2 and 30,634 m^2 respectively. This situation was also valid for the formation of dump sites, 88,046 m^2 of forest and 66,202 m^2 of bareland was disturbed by overburden dumping. Coal stock site was located mainly on bareland with an area of 7,594 m^2. Forest area decreased an amount of 106,485 m^2 from 1951 to 2008. However, by means of the forestation of dump sites D1 and D2, an amount of 106,012 m^2 forest land was recovered. Due to expanding agricultural activities of nearby villagers, use of 34,877 m^2 of forest land has been changed to agriculture.

Table 17 LULC change matrix between 1951 and 2008

LULC change in m^2		2008								
		Agriculture	Bareland	Forest	Sparse Buildings	Excavation	Dump	Coal stock	Lake	Total
1951	Agriculture	56059	180	27			3			56269
	Bareland	17688	220530	69482	14468	30634	66202	7594	6404	433002
	Forest	34877	11766	396810	3702	37595	88046	11		572807
	S. Buildings				1773					1776
	Total	108624	232476	466319	19943	68229	154251	7605	6404	1063851

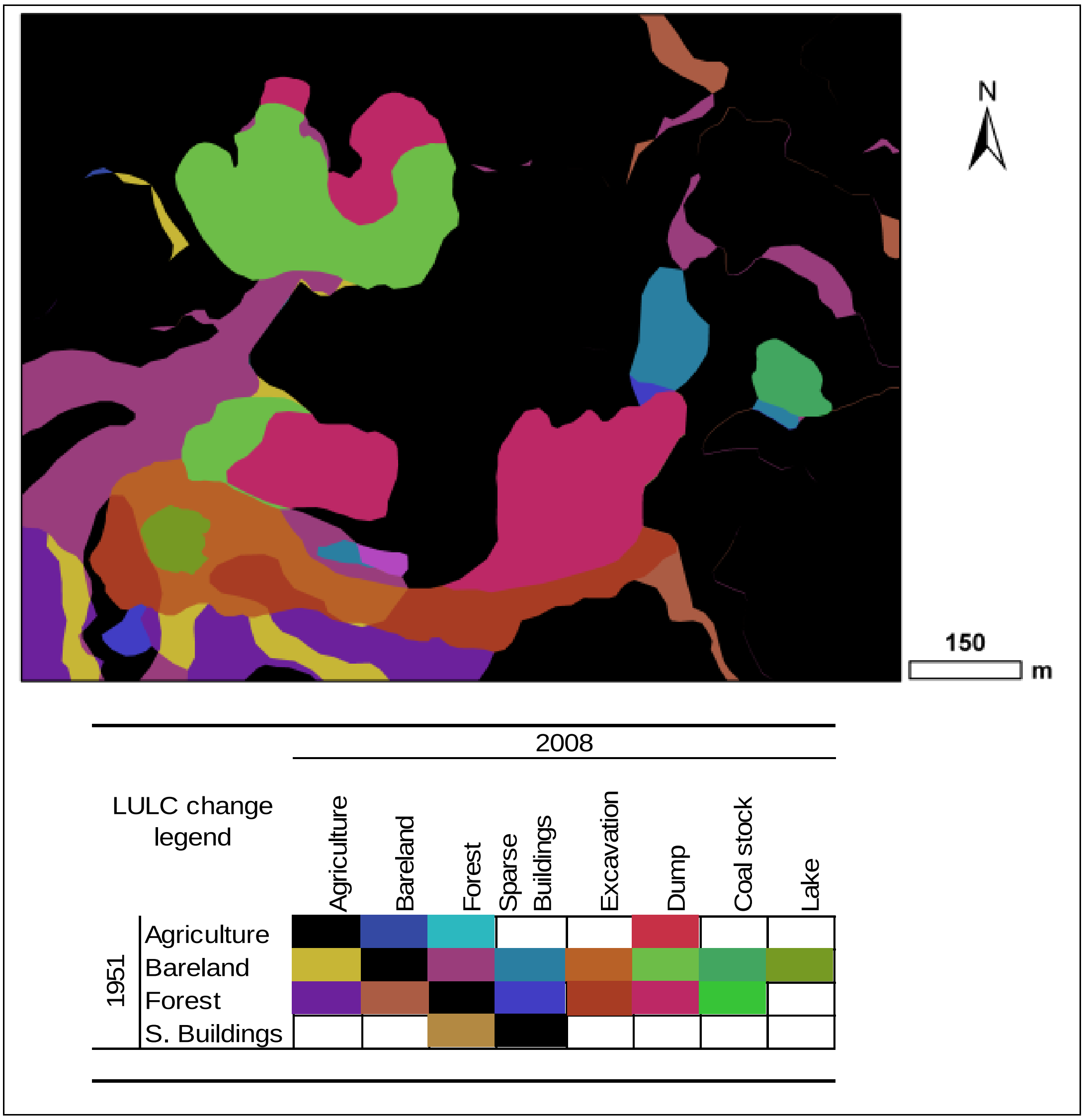

Figure 66 LULC change map between 1951 and 2008

3.7.4 Analysis of relation between Slope and LULC

It was observed that there was an obvious relation between LULC with slope. As seen in Table 2, the highest areas for the very steep slopes occurred in the LULC of excavation and bareland as 2591 m^2 and 320 m^2. In addition to that, percentages of land area where the slope angle is larger than 40 degrees with respect to the total area of each class were % 19.4 for excavation and % 3.7 for bareland classes.

Lowest slope ranges were observed in the classes of lake, agriculture, and sparse buildings.

Table 18 Areas of land use classes for each slope range

Slope range (degree)	LULC classes (m2) Agriculture	Bareland	Forest	Sparse Buildings	Excavation	Dump	Coal stock	Lake	Total
0-30	101959	187612	406953	18239	37134	125308	6956	6404	890566
30-40	5120	36285	46274	1407	17796	24110	280	0	131273
40-50	1355	7250	11078	247	7278	4012	342	0	31561
50-60	161	1010	1832	48	3429	753	28	0	7260
60-90	29	320	182	2	2591	69	0	0	3192
Total	108624	232476	466319	19943	68229	154251	7605	6404	1063851

3.8 Results and Discussions

In this study, land degradation in abandoned Ovacık surface coal mine was assessed with geospatial information technologies. The results of implementation were summarized below;

1) Using historic aerial photos, pre-mining topography of the research area was extracted with 2.95 m RMSE. In addition to that LULC classes forest, bareland, agriculture and sparse buildings were identified and mapped by using aerial photos for pre-mining stage of the study area.

2) The current LULC consists of classes excavation, dump, lake, coal stock, forest, bareland, agriculture and sparse buildings, were obtained by using panchromatic Worldview-1 imagery.

3) LULC map was extracted for above mentioned classes using VNIR bands of ASTER dataset taken in 2007 with an overall accuracy of 41% by using maximum likelihood classification. Although maximum likelihood classification gave slightly better accuracy (41%) than SVM classification (39%), visual inspection of results showed that SVM classification created a more homogenous LULC map than the maximum likelihood classification. Moreover, it was observed that adding SWIR and TIR bands to VNIR bands in Support Vector Machine (SVM) classification of the ASTER imagery increased the overall classification accuracy from 33% to 39%.

4) In the research area, Landsat images were found to be inadequate to identify mine features and map LULC due to coarse spatial resolution (28.5 m). However, it was observed that image differencing of first bands of Landsat TM and ETM images taken in 1987 and 2000 delineated the open pit excavation area.

5) It was found that application of Terrestrial Laser Scanner (TLS) was very powerful tool in generation of detailed DEM in a short time compared to conventional measurement techniques such as total station and GPS surveys. However, it was difficult in thesis implementation to fully measure the study area due to rough terrain, forest cover and time limitation by TLS. In such conditions where detailed DEM was needed, author recommends aerial surveys such as photogrammetry, Light Detection and Ranging (LIDAR) and Interferometric Synthetic Aperture Radar (InSAR).

6) Land Use and Land Cover (LULC) change analysis revealed that 63% of the study area had been changed from 1951 to 2008. Specifically, 37,595 m^2 forest areas were damaged by open pit excavation. In addition to the excavation, formation of dump sites disturbed 88,046 m^2 of forest. On the other hand, forestation of dump sites D1 and D2 recovered 106,012 m^2 of forest land. It was also observed that due to expanding agricultural activities of nearby villagers, 34,877 m^2 forest area converted to agricultural land.

7) It was found that cut and fill operations in the study area had significantly changed drainage network around open pit, primary dump site and coal stock site. Maximum of displacement in the drainage network was found 60 m near primary dumps site. Furthermore, erosional formations - gully and rill- were observed where the drainage network was disturbed, especially around slopes of the dump sites and the open pit.

8) By the help of slope analysis, it was found that mining activity increased slope angles across the study area. It is found that, across the research area, 81% of very steep slopes (> 60 degrees) were observed within the excavation area.

CHAPTER 5

CONCLUSIONS AND RECOMMENDATIONS

4.1 Conclusions

Surface coal mining is one of the important causes of the land degradation which threatens the biological and economical value of the land. Reclamation of these degraded mined-out lands requires detailed assessment of land degradation characteristics of the site. After increasing environmental concerns about the impacts of mining and new regulations about remediation of these impacts, it became more important to use more practical monitoring methods for land degradation assessment caused by mining activities. Geospatial information technologies Remote Sensing (RS) and Geographic Information Systems (GIS) can play a central role in assessment of mining induced environmental impacts. Providing multitemporal earth observation data, capability of management of this large amount of data, and wide range of spatial data analysis options make geospatial technologies essential for all stages of land degradation assessment and reclamation planning such as topographic and land use change detection, and site prioritization for rehabilitation.

Land degradation in Ovacık abandoned surface coal mine was successfully assessed and quantified based on geospatial information technologies. Topographic and Land Use and Land Cover (LULC) change amounts and patterns were computed and mapped. As this research is the first study on environmental impacts of Ovacık surface coal mine, it will be a base for further studies on land degradation assessment or reclamation and closure planning for the site. Regarding priority of human health and safety in environmental management of the abandoned mine, it is urgent to maintain physical stability firstly around the open pit either the mine will be operated or the site will be closed in the future. Research results also show that there is a severe drainage network change in the site with lake, pond formations, deviations in the main stream and erosinal formations -rill and gully- triggered by intense surface runoff in especially slopes of the dump sites. Erosion in the site should also be considered in reclamation planning phase to stabilize the slopes and maintain ecological balance. In addition to that, LULC maps for pre- and post-mining stages and corresponding change map were extracted. Areal extents of any type of LULC transitions were calculated and spatially mapped, this especially demonstrate severity of land degradation in terms of deforestation. Determination of areas disturbed by mining activities which were not reclaimed yet can give also profound advantages with respect to future land use and reclamation planning and cost estimates.

The illegal small coal production openings detected during field studies which are posing danger to local people should be immediately sealed by the authorities in order to prevent undesirable accidents. Furthermore, Acid Mine Drainage (AMD), soil and water pollution parameters needs further investigation to quantify chemical stability of the abandoned mine site.

Results of aerial photo processing reveal that, the historical aerial photo archive in General Command of Mapping (HGK) constitute a valuable even sometimes only data source in extraction of topography and LULC for pre-mining stages of old mines in Turkey.

Image processing results show that Landsat and ASTER satellite imagery could not supply sufficient detail of information for land degradation assessment of Ovacık surface coal mine having small extent relative to pixel sizes of these sensors.

The proposed approach can also be implemented as a guideline for other abandoned or even operating surface mines as a method for land degradation assessment with geospatial technologies. It is sure that methodology can be modified for each individual mine site according to local settings such as extent and data availability.

4.2 Recommendations for Further Studies

The recommendations for further studies are discussed below.

1) The case study can be widened to cover soil and water pollution investigation in the abandoned mine site and cost calculation for implementation a reclamation plan to be proposed based on the analyses.

2) Proposed reclamation plan can be prepared and visualized in 3D virtual reality environment to present to the stakeholders during discussion of the plan and to simulate different development scenarios for the site.

3) Research methodology can be further developed to create a Decision Support System (DSS) for site prioritization for reclamation efforts in local and regional scales.

4) Usage of higher spatial and spectral imagery can increase classification accuracy and ability to assess more detailed mine features such as mine acid drainage and soil pollution by hyperspectral imagery together with field spectroscopy.

REFERENCES

Abuelgasim, A., Chung, C., Champagne, C., Staenz, K., Monet, S., & Fung, K. (2005). Use of Multi-temporal Remotely Sensed Data for Monitoring Land Reclamation in Sudbury, Ontario (Canada). *International Workshop on the Analysis of Multi-Temporal Remote Sensing Images*, (pp. 229-235).

Anderson, A. T. (1977). Landsat Imagery for surface Mine Inventory. *Photogrametric Engineering and Remote Sensing , 8*, 1027-1036.

Antwi, E. K., Krawczynski, R., & Wiegleb, G. (2008). Detecting the effect of disturbance on habitat diversity and land cover change in a post-mining area using GIS. *Landscape and Urban Planning , 87*, 22-32.

Balkau, F. (1993). Pollution Prevention and Abatement Guidelines for the Mining Industry. 17. Paris: UNEP IE/PAC.

Behum, P. T. (2004). Application of LIDAR Imagery in AML Reclamation: Case Example – Design of an AMD Passive Treatment System at the Rock Island No. 7 Airshaft, Oklahoma. *Advanced Integration of Geospatial Technologies in Mining and Reclamation.* Atlanta.

Blanco, J. L., Moreno, F. A., & Gonzalez, J. (2009). A Collection of Outdoor Robotic Datasets with Centimeter-accuracy Ground Truth. *Autonomous Robots , 27* (4), 327–351.

Canada Centre for Remote Sensing. (2008). *Tutorial: Fundamentals of Remote Sensing, Introduction, What is Remote Sensing?* Retrieved July 15, 2010, from http://www.ccrs.nrcan.gc.ca/resource/tutor/fundam/chapter1/01_e.php

Castro-Esau, K. L., Sanchez-Azofeifa, G. A., & Caelli, T. (2004). Discrimination of lianas and trees with leaf-level hyperspectral data. *Remote Sensing of Environment , 90* (3), 353-372.

Choi, Y., Park, H. D., & Sunwoo, C. (2008). Flood and gully erosion problems at the Pasir open pit coal mine, Indonesia: a case study of the hydrology using GIS. *Bulletin of Engineering Geology and the Environment , 67* (2), 251-258.

Clarke, K. C., 1986.Advances in Geographic Information Systems. *Computers, Environment and Urban Systems*, *10*, 175-184.

Comber, A., Fisher, P., & Wadsworth, R. (2005). What is land cover. *Environment and Planning B: Planning and Design , 32* (2), 199-209.

Duong, N. D., Nierynck, E., Van, T., & Hens, L. (1999). "Land Use Changes and GIS-Database Development for Strategic Environmental Assessment in Ha Long Bay, Quang Ninh province, Vietnam. *Proceedings of Geoinformatics Conference*, (pp. 1-15). Ann Arbor.

Düzgün, H.S.B. (2009). "Maden Kapatma Planlaması ve Doğaya Yeniden Kazandırmanın Temel İlkeleri", *3. Madencilik ve Çevre Sempozyumu*, 11-12 Haziran, (pp.1-16), Ankara

Ellis, E., & Pontius, R. (2007). *Land-use and land-cover change.* Retrieved July 16, 2010, from Encyclopedia of Earth: http://www.eoearth.org/article/Causes_of_land-use_and_land-cover_change

Energy Information Administration (2008). *US Energy Information Administration, Indipendent Statistics and Analysis.* Retrieved June 21, 2010 from International Coal Production: http://www.eia.doe.gov/emeu/international/coalproduction.html

ENVI 4.7 Help Menu (2010). ITT Visual Information Solutions.

Environmental Protection Agency, United States (2006). *What is GIS*. Retrieved June 5, 2010, from http://www.epa.gov/region5fields/htm/methods/gis/

Erdoğan, N. (2002). Monitoring Changes in Surface Mining Area by using SPOT Satellite Images, Ms Thesis. *METU Mining Engineering Department* , 118. Ankara, Turkey.

Ganas, A., Aerts, J., Astaras, T., Vente, J., Frogoudakisi, E., Lambrinos, N., et al. (2004). The Use of Earth Observation and Decision Support Systems in the Restoration of Open-Cast Nickel Mines in Evia, Central Greece. *International Journal of Remote Sensing , 25* (16), 3261–3274.

Garbrecht, J., & Martz, L. W. (2000). Digital elevation model issues in water resources modeling. In D. Maidment, & D. Djokic, *Hydrologic and Hydraulic Modeling Support with Geographic Information Systems* (pp. 1-28). California: ESRI Press.

Hill, M. (2004). 3-D Modeling of Large Anthracite Open Pit Mining Operations to Assist in Pennsylvania's Conversion to Conventional Bonding. *Advanced Integration of Geospatial Technologies in Mining and Reclamation.* Atlanta.

Irons, J. R., & Kennard, R. L. (1986). The Utility of Thematic Mapper Sensor Characteristics for surface Mine Monitoring. *Photogrammetric Engineering and Remote Sensing , 52*, pp. 389-396.

Jacobsen, K. (2001). Exterior orientation parameters. *Journal of the American Society for Photogrammetry and Remote Sensing , 67* (12), pp. 1321-1332.

Jaw, J. (2001). Statistics-based Fusion of Terrain Data Sets and Change Detection. *22nd Asian Conference on Remote Sensing* (p. 6). Singapore: Center for Remote Imaging, Sensing, and Processing, National University of Singapore.

Jenson, S. K., & Domingue, J. O. (1988). Extracting Topographic Structure from Digital Elevation Data for Geographic Information System Analysis. *Photogrammetric Engineering and Remote Sensing , 54* (11), pp. 1593-1600.

Lévesque, J., & Staenz, K. (2004). A Method for Monitoring Mine Tailings Re-Vegetation Using Hyperspectral Remote Sensing. *Proceedings of International Geoscience and Remote Sensing Symposium.* Anchorage, Alaska.

Lillesand, T. M., Kiefer, R. W., & Chipman, J. W. (2004). *Remote Sensing and Image Interpretation* (5 ed.). New York: Wiley.

Lu, D., & Weng, Q. (2007). A Survey of Image Classification Methods and Techniques for Improving Classification Performance. *International Journal of Remote Sensing , 28* (5), 823-870.

Lu, D., Mausel, P., Brondi, Z. E., & Moran, E. (2005). Change Detection Techniques. *International Journal of Remote Sensing , 25* (12), 2365-2407.

Manu, A., Twumasi, Y. A., & Coleman, T. L. (2004). Application of Remote Sensing and GIS Technologies to Assess the Impact of Surface Mining at Tarkwa, Ghana. *Proceedings of International Geoscience and Remote Sensing Symposium.* Anchorage, Alaska.

Markus, J. J. (1997). *Mining Environmental Handbook: Effects of Mining on the Environment and American Environmental Controls on Mining.* Imperial Collage Press.

Mather, P. M. (2004). *Computer Processing of Remotely-Sensed Images- An Introduction* (3 ed.). John Wiley & Sons.

Moore, J. N., & Luoma, S. N. (1990). Hazardous Wastes from Large-Scale Metal Extraction. *Environmental Science Technology , 24* (9), 1278-1287.

Mularz, S. C. (1998). Satellite and Airborne Remote Sensing Data for Monitoring of an Open-Cast Mine. *International Archives of Photogrammetry and Remote Sensing , 32* (4), 385-402.

Nori, W., Elsiddig, E. N., & Niemeyer, I. (2008). Detection of Land Cover Changes Using Multi-Temporal Satellite Imagery. *The International Archives of the Photogrammetry, Remote Sensing and Spatial Information Sciences , 37* (B7), 947-952.

Pavelka, K., & Halounová, L. (2004). Using of TM Data and VHR Data for Reclaimed Areas Monitoring Using Vegetation Indices. *International Archives of the Photogrammetry, Remote Sensing and Spatial Information , 34* (30).

Prakash, A., & Gupta, R. P. (1998). Land-use Mapping and Change Detection in a Coal Mining Area- A Case Study in the Jharia Coal field, India. *International Journal of Remote Sensing , 19* (3), 391410.

Röder, A., & Hill, J. (2009). *Recent Advances in Remote Sensing and Geoinformation Processing for Land Degradation Assessment.* Aiken, The Netherlands: CRC Press.

Shank, M. (2004). Development of a Mining Fill Inventory from Multi-date Elevation Data. *Advanced Integration of Geospatial Technologies in Mining and Reclamation.* Atlanta.

Strahler, A. N. (1952). Dynamic Basis of Geomorphology. *Geological Society of America Bulletin* (63), 923-938.

Tören, T. (2001). Determination of Mining Induced Environmental Impacts Using Remote Sensing and GIS, PhD Thesis. *METU Mining Engineering Department* , 181. Ankara, Turkey.

Turkish State Meteorological Service. (2010). *Çankırı içinYıllık Toplam Yağış Verileri*. Retrieved July 20, 2010, from http://www.meteor.gov.tr/veridegerlendirme/yillik-toplam-yagis-verileri.aspx?m=cankiri

Woldai, T. (2001). Application of Remotely Sensed Data and GIS in Assessing the Impact of Mining Activities on the Environment. *17th International Mining Congress & Exhibition of Turkey*, (pp. 75-83). Ankara.

Woldai, T., & Taranik, J. (2008). Environmental Impact Assessment of Mining Related Dewatering Activities using Integrated InSAR, Optical Remote Sensing and Pumping Data. *International Archives of the Photogrammetry, Remote Sensing and Spatial Information Sciences , 37* (B7), 191-198.

World Coal Institute. (2010). *Coal Mining.* Retrieved June 23, 2010, from http://www.worldcoal.org/coal/coal-mining/

APPENDIX A

ACCURACY ASSESSMENT OF DEMs

Table A1 RMSE table for DEM generated by aerial photos

#	GCP ID	GCP Elevation (m) (reference)	DEM Elevation (m)	Difference	Square of difference
1	C1	1290.105	1292.171	-2.066	4.270
2	C2	1289.637	1292.784	-3.147	9.904
3	C3	1287.905	1291.132	-3.227	10.412
4	C4	1286.774	1290.351	-3.577	12.793
5	D10	1287.648	1290.920	-3.272	10.709
6	P149	1305.531	1304.025	1.507	2.270
7	D12	1302.268	1301.112	1.156	1.336
8	D13	1301.202	1301.465	-0.264	0.069
9	D14	1304.673	1302.748	1.925	3.704
10	D15	1306.470	1302.925	3.545	12.565
11	D16	1302.207	1301.500	0.707	0.501
12	D17	1302.077	1301.500	0.577	0.334
13	D18	1300.842	1300.919	-0.077	0.006
14	D19	1299.376	1300.746	-1.370	1.876
15	D20	1299.686	1300.433	-0.747	0.558
16	D21	1311.644	1313.329	-1.686	2.841
17	D22	1314.499	1315.220	-0.721	0.521
18	D23	1315.190	1314.370	0.820	0.673
19	D24	1311.263	1311.047	0.216	0.047
20	D25	1311.673	1308.878	2.795	7.814
21	D26	1310.482	1308.584	1.898	3.601
22	D27	1310.115	1308.372	1.743	3.039
23	P	1311.926	1311.611	0.315	0.099
24	D100	1302.654	1302.864	-0.210	0.044
25	D101	1303.072	1303.064	0.008	0.000
26	D102	1302.657	1299.278	3.379	11.416
27	6001	1260.292	1262.963	-2.671	7.133
28	6005	1260.152	1260.997	-0.845	0.714
29	6008	1259.952	1259.268	0.684	0.468
30	6011	1259.758	1257.594	2.164	4.684
31	6014	1258.782	1256.451	2.331	5.433
32	6017	1258.533	1255.801	2.732	7.464
33	6020	1258.711	1255.474	3.237	10.481
34	6023	1258.505	1255.131	3.374	11.382
35	6026	1258.528	1254.954	3.573	12.770

(table continues)

Table A1 RMSE table for DEM generated by aerial photos (continued)

#	GCP ID	GCP Elevation (m) (reference)	DEM Elevation (m)	Difference	Square of difference
36	6029	1258.166	1255.243	2.923	8.546
37	6032	1258.187	1256.508	1.679	2.820
38	6035	1257.582	1257.260	0.321	0.103
39	6038	1257.869	1257.528	0.341	0.116
40	6041	1257.352	1257.593	-0.241	0.058
41	6044	1257.393	1257.380	0.013	0.000
42	6047	1257.008	1257.587	-0.579	0.335
43	6050	1256.577	1258.199	-1.622	2.632
44	6053	1256.261	1259.338	-3.077	9.468
45	6086	1253.390	1255.615	-2.225	4.952
46	6089	1252.640	1253.543	-0.904	0.816
47	6092	1252.382	1251.985	0.397	0.158
48	6095	1251.879	1250.596	1.283	1.645
49	6098	1252.041	1250.360	1.681	2.826
50	6101	1251.264	1250.648	0.616	0.379
51	6104	1251.565	1250.772	0.793	0.629
52	6107	1249.807	1249.876	-0.069	0.005
53	6110	1249.072	1248.009	1.063	1.130
54	6113	1248.833	1247.247	1.586	2.516
55	6116	1248.661	1247.660	1.001	1.002
56	6119	1248.613	1249.002	-0.389	0.151
57	7002	1246.894	1248.866	-1.972	3.888
58	7005	1246.417	1246.552	-0.135	0.018
59	7008	1246.111	1245.115	0.996	0.993
60	7011	1245.886	1243.724	2.161	4.672
61	7014	1245.854	1242.770	3.085	9.514
62	7017	1245.666	1242.143	3.523	12.414
63	7020	1245.095	1241.403	3.692	13.631
64	7040	1242.616	1239.142	3.474	12.065
65	7043	1241.382	1238.804	2.578	6.646
66	7046	1241.370	1238.154	3.216	10.344
67	7049	1240.725	1237.607	3.118	9.721
68	7052	1240.431	1237.078	3.353	11.246
69	7055	1239.893	1236.754	3.139	9.855
70	7058	1239.400	1235.972	3.428	11.748

(table continues)

Table A1 RMSE table for DEM generated by aerial photos (continued)

#	GCP ID	GCP Elevation (m) (reference)	DEM Elevation (m)	Difference	Square of difference
71	7061	1238.828	1235.452	3.376	11.395
72	7064	1238.253	1235.119	3.134	9.824
73	7067	1237.606	1235.392	2.214	4.901
74	7070	1236.220	1236.779	-0.559	0.313
75	7073	1235.387	1237.961	-2.574	6.626
76	D104	1231.869	1230.252	1.617	2.616
77	D105	1232.521	1228.960	3.561	12.681
78	D106	1231.951	1229.296	2.655	7.051
79	D107	1232.748	1229.529	3.219	10.361
80	D110	1236.312	1233.522	2.790	7.782
81	D111	1228.240	1224.469	3.771	14.223
82	D112	1224.466	1221.940	2.526	6.380
83	8	1286.516	1296.025	-9.509	90.423
84	10	1281.449	1290.920	-9.471	89.696
85	44	1243.747	1251.363	-7.616	58.008
86	65	1249.560	1250.311	-0.751	0.565
87	49	1236.729	1235.150	1.579	2.493
88	20	1279.178	1277.473	1.705	2.908
89	71	1275.559	1273.706	1.853	3.434
90	70	1274.483	1272.550	1.933	3.735
91	69	1273.058	1271.105	1.953	3.814
92	72	1277.904	1275.810	2.094	4.386
93	23	1280.476	1278.373	2.103	4.423
94	53	1234.045	1231.757	2.288	5.233
95	24	1292.346	1290.045	2.301	5.295
96	73	1278.203	1275.884	2.319	5.376
97	21	1290.325	1287.976	2.349	5.520
98	22	1279.233	1276.845	2.388	5.702
99	17	1293.810	1291.354	2.457	6.034
100	78	1278.952	1276.486	2.466	6.081
101	79	1277.815	1275.146	2.669	7.126
102	43	1246.565	1243.704	2.861	8.186
103	18	1293.650	1290.689	2.961	8.769
104	19	1280.089	1277.111	2.978	8.868
105	52	1236.575	1233.538	3.037	9.223

(table continues)

Table A1 RMSE table for DEM generated by aerial photos (continued)

#	GCP ID	GCP Elevation (m) (reference)	DEM Elevation (m)	Difference	Square of difference
106	67	1265.077	1261.984	3.093	9.569
107	77	1280.202	1276.976	3.226	10.406
108	38	1262.280	1258.608	3.672	13.482
109	5	1312.049	1308.339	3.710	13.764
110	74	1280.011	1276.299	3.712	13.780
111	P.152	1295.604	1291.822	3.782	14.303
112	25	1293.839	1290.045	3.794	14.394
113	37	1265.365	1261.310	4.055	16.441
114	47	1233.378	1229.189	4.189	17.545
115	76	1281.297	1277.010	4.287	18.378
116	6	1299.984	1295.686	4.298	18.471
117	28	1300.482	1296.072	4.410	19.445
118	54	1234.241	1229.769	4.472	20.001
119	55	1234.235	1229.650	4.585	21.023
120	29	1298.987	1294.316	4.671	21.816
121	26	1295.105	1290.351	4.754	22.603
122	51	1239.950	1235.073	4.877	23.785
123	56	1243.000	1237.899	5.101	26.018
				Sum of square errors:	1073.646
				Number of test samples:	123
				Mean square error:	8.729
				Root mean square (RMS) error:	2.954

Table A2 RMSE table for DEM generated by Terrestrial Laser Scanner

#	GCP ID	GCP Elevation (m) (reference)	DEM Elevation (m)	Difference	Square of difference
1	1	1280.276	1281.034	-0.758	0.575
2	2	1282.964	1284.254	-1.290	1.664
3	3	1282.724	1283.409	-0.685	0.469
4	4	1285.046	1286.095	-1.049	1.101
5	6	1299.984	1301.508	-1.524	2.321
6	7	1299.861	1300.789	-0.928	0.861
7	8	1286.516	1288.277	-1.761	3.101
8	11	1268.680	1268.035	0.645	0.416
9	12	1249.228	1249.647	-0.419	0.175
10	13	1250.470	1252.147	-1.678	2.814
11	14	1249.852	1249.065	0.787	0.619
12	15	1254.034	1254.503	-0.469	0.220
13	19	1280.089	1278.489	1.600	2.560
14	20	1279.178	1277.752	1.426	2.032
15	21	1290.325	1288.269	2.056	4.225
16	22	1279.233	1278.262	0.971	0.942
17	23	1280.476	1279.329	1.147	1.316
18	24	1292.346	1292.860	-0.514	0.264
19	25	1293.839	1292.860	0.979	0.958
20	26	1295.105	1292.920	2.185	4.776
21	28	1300.482	1298.542	1.940	3.764
22	29	1298.987	1297.914	1.073	1.152
23	30	1287.410	1287.830	-0.420	0.177
24	31	1287.247	1287.559	-0.312	0.097
25	32	1289.437	1289.516	-0.079	0.006
26	33	1291.282	1290.751	0.531	0.282
27	34	1307.021	1307.062	-0.041	0.002
28	35	1291.229	1290.735	0.494	0.244
29	36	1270.064	1270.100	-0.036	0.001
30	39	1252.207	1250.549	1.658	2.749
31	40	1252.283	1251.565	0.718	0.516
32	41	1253.090	1252.141	0.949	0.900
33	42	1242.299	1241.325	0.974	0.949
34	45	1236.315	1235.221	1.094	1.197
35	46	1235.734	1234.456	1.278	1.634

(table continues)

Table A2 RMSE table for DEM generated by Terrestrial Laser Scanner (continued)

#	GCP ID	GCP Elevation (m) (reference)	DEM Elevation (m)	Difference	Square of difference
36	47	1233.378	1231.318	2.060	4.244
37	48	1230.199	1230.247	-0.048	0.002
38	49	1236.729	1236.917	-0.188	0.035
39	52	1236.575	1236.659	-0.084	0.007
40	53	1234.045	1234.045	0.000	0.000
41	54	1234.241	1233.385	0.856	0.732
42	55	1234.235	1233.938	0.297	0.088
43	56	1243.000	1242.652	0.348	0.121
44	57	1245.277	1244.160	1.117	1.247
45	58	1243.279	1241.664	1.615	2.609
46	59	1241.370	1240.532	0.838	0.702
47	60	1241.899	1240.554	1.345	1.808
48	61	1248.122	1246.774	1.348	1.818
49	62	1247.989	1248.030	-0.041	0.002
50	63	1251.118	1251.774	-0.656	0.430
51	64	1252.066	1251.730	0.336	0.113
52	65	1249.560	1248.901	0.659	0.435
53	66	1262.105	1260.975	1.130	1.277
54	67	1265.077	1264.797	0.280	0.078
55	68	1273.067	1272.273	0.794	0.630
56	69	1273.058	1272.293	0.765	0.586
57	70	1274.483	1274.495	-0.012	0.000
58	71	1275.559	1275.563	-0.005	0.000
59	72	1277.904	1277.238	0.666	0.444
60	73	1278.203	1277.602	0.601	0.362
61	74	1280.011	1279.588	0.423	0.179
62	75	1281.627	1281.317	0.310	0.096
63	76	1281.297	1281.569	-0.273	0.074
64	77	1280.202	1279.940	0.262	0.068
65	78	1278.952	1278.841	0.111	0.012
66	79	1277.815	1277.383	0.432	0.187
67	80	1266.435	1264.811	1.624	2.638
68	81	1259.262	1258.593	0.669	0.448
69	K.1	1283.753	1284.252	-0.499	0.249
70	P.1	1252.912	1252.128	0.784	0.615
				Sum of square errors:	67.415
				Number of test samples:	70
				Mean square error:	0.963
				Root mean square (RMS) error:	0.981

APPENDIX B

SATELLITE IMAGERY

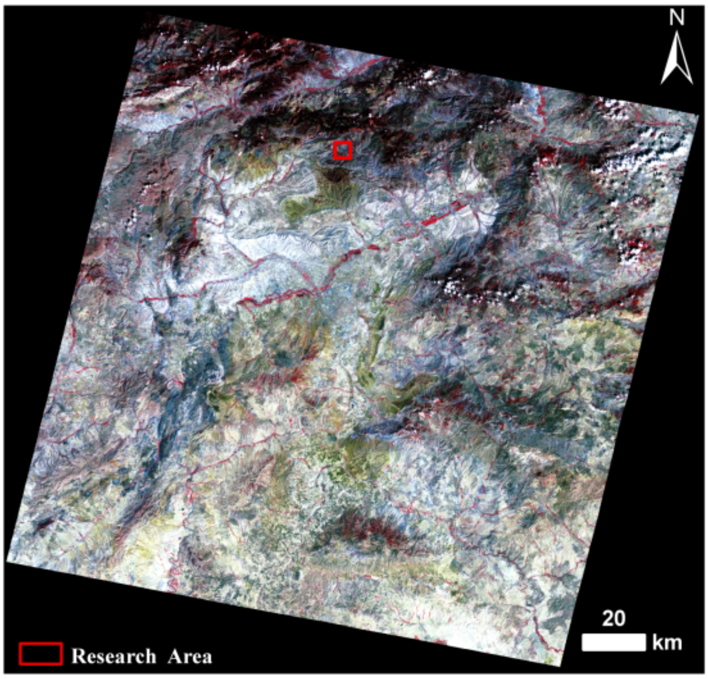

Figure B1 Full scene Landsat-2 MSS imagery (False color composite, RGB: 321) acquired on September 12, 1975

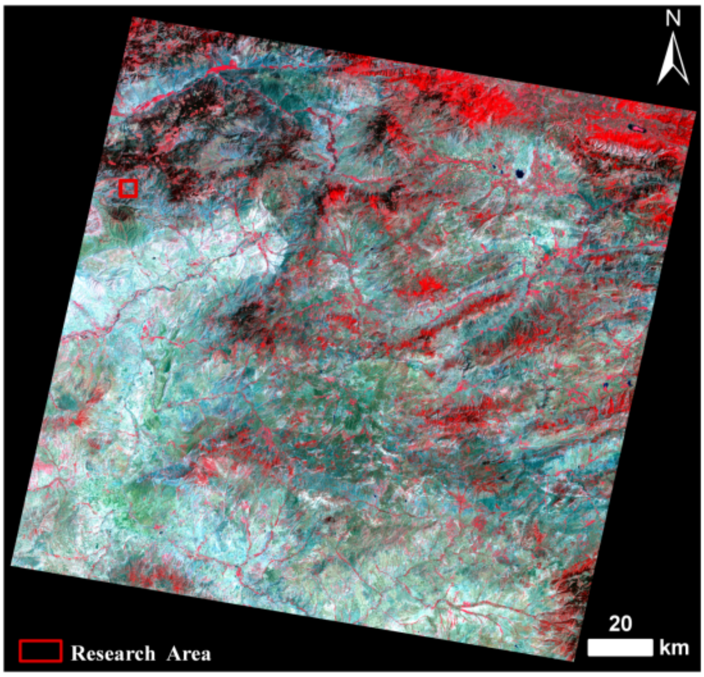

Figure B2 Full scene Landsat-5 TM imagery (False color composite, RGB: 432)
acquired on July 27, 1987

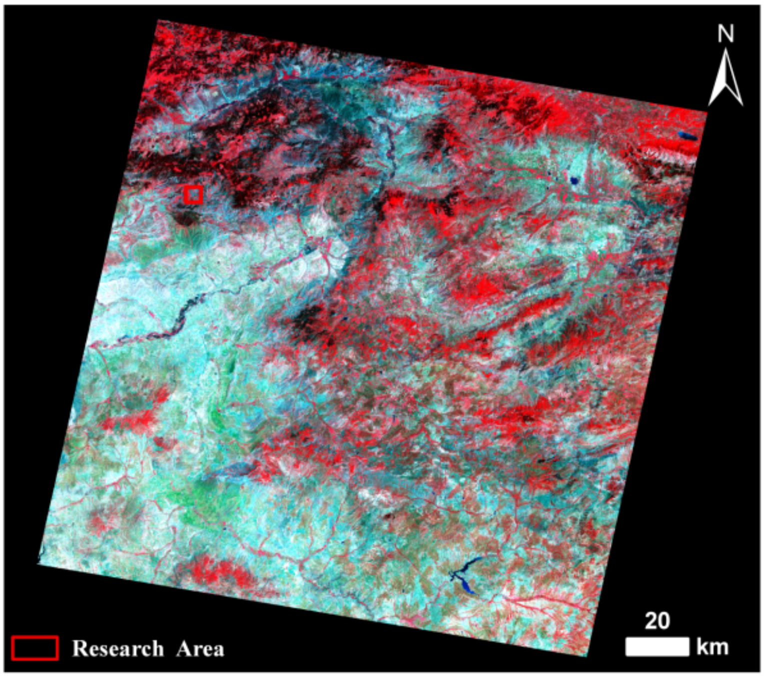

Figure B3 Full scene Landsat-7 ETM+ imagery (False color composite, RGB: 432)
acquired on July 06, 2000

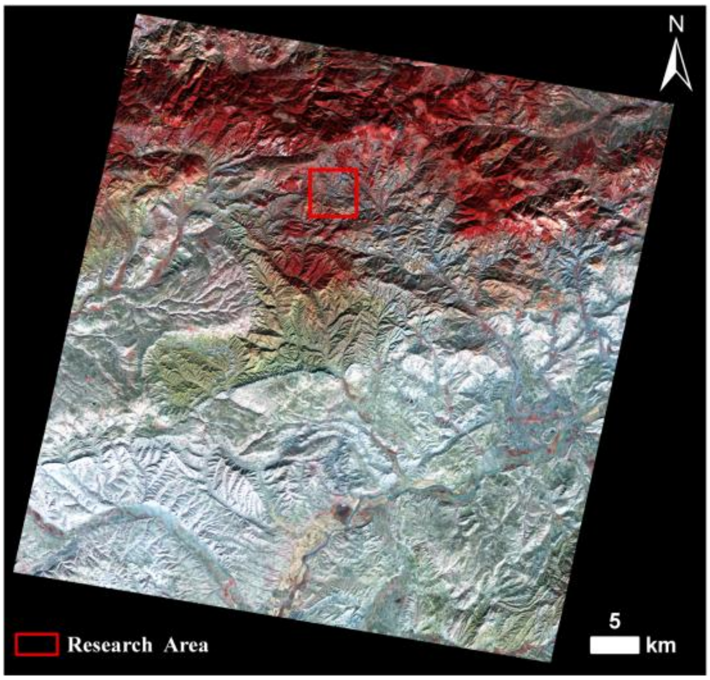

Figure B4 Full scene ASTER imagery (False color composite, RGB: 3N21) acquired on November 17, 2002

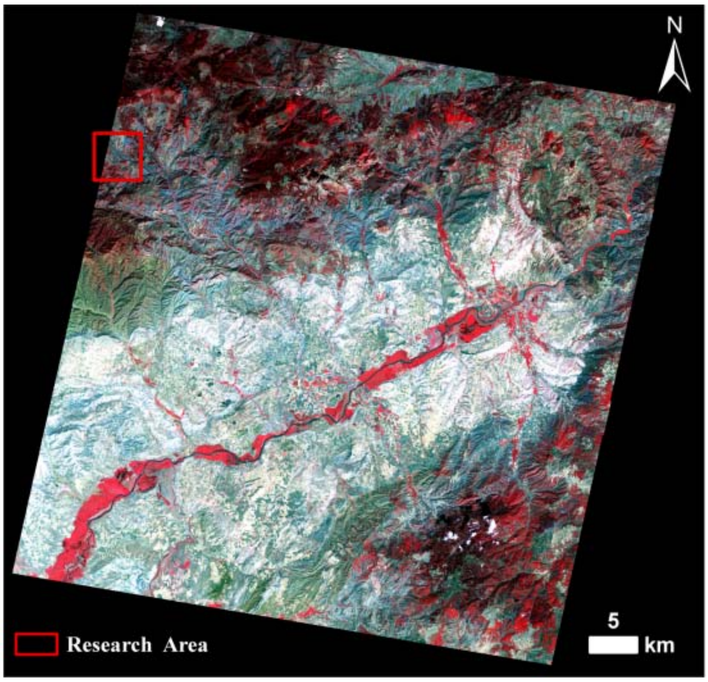

Figure B5 Full scene ASTER imagery (False color composite, RGB: 3N21) acquired on September 12, 2007

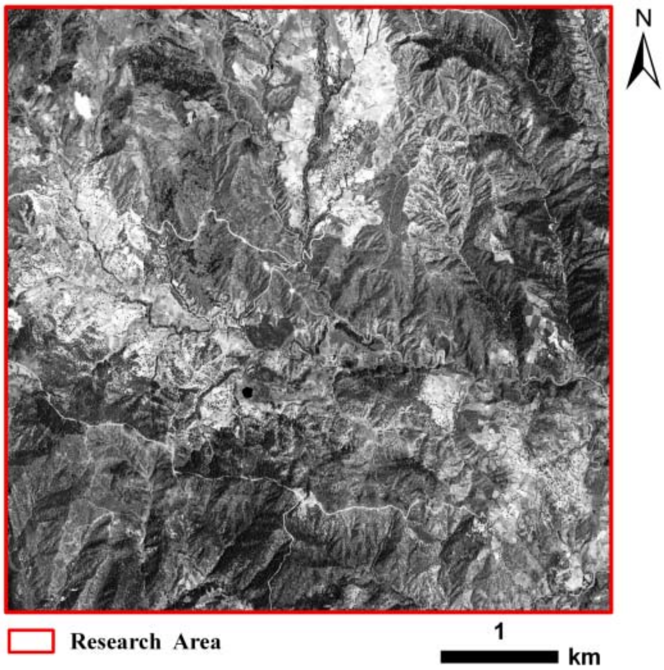

Figure B6 Worldview-1 panchromatic (B&W) imagery acquired on August 28, 2008

APPENDIX C

THRESHOLDING FOR IMAGE DIFFERENCING

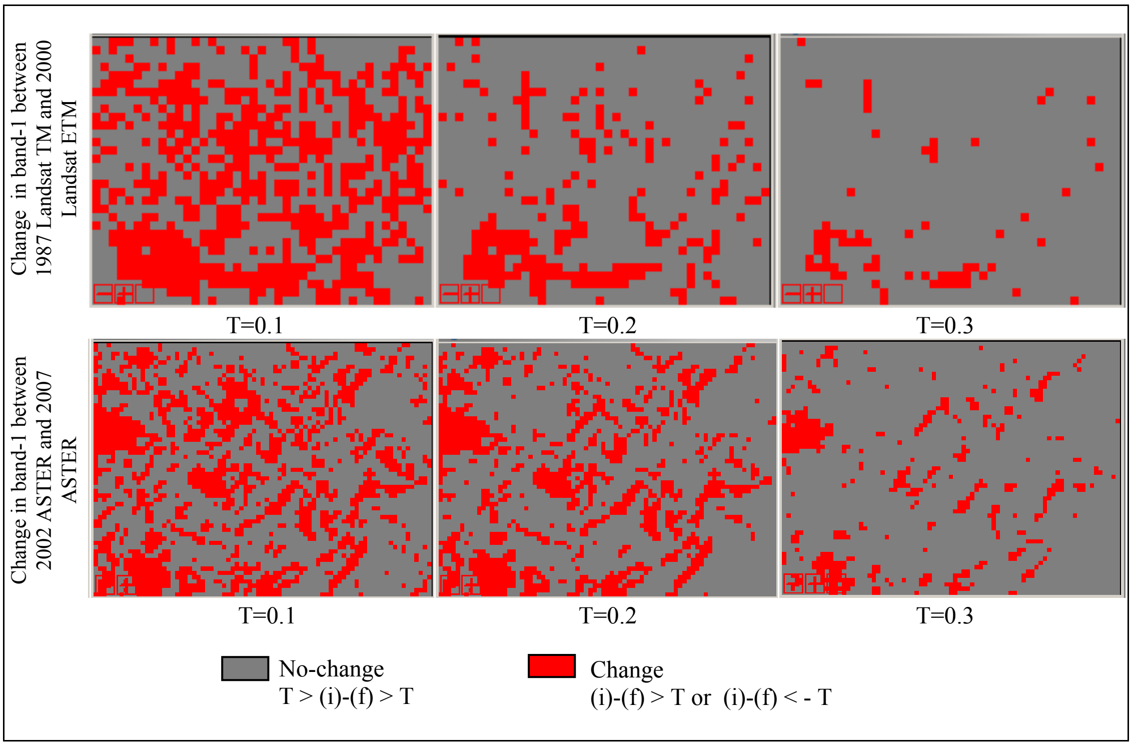

Figure C1 Change images obtained by applying various thresholds (T) to band-1 difference images for Landsat and ASTER dataset

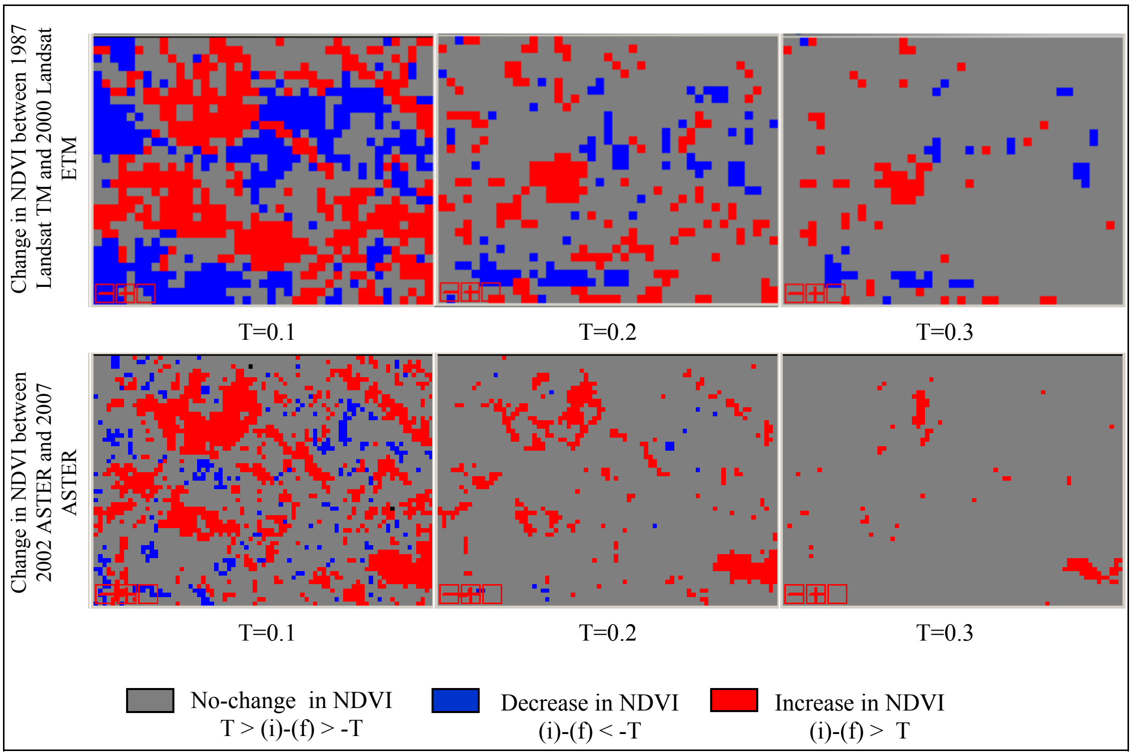

Figure C2 Change images obtained by applying various thresholds (T) to NDVI difference images for Landsat and ASTER dataset